Cytoskeletal filament and intracellular cargo dynamics facilitated by motor proteins : role of activity and a catch-bonded dynein

Nisha Gupta

A thesis submitted for the partial fulfillment of
the degree of Doctor of Philosophy

Department of Physical Sciences

Indian Institute of Science Education and Research Mohali
Knowledge city, Sector 81, SAS Nagar, Manauli PO, Mohali 140306,
Punjab, India.

August 2019

Certificate of Examination

This is to certify that the dissertation titled *"Cytoskeletal filament and intracellular cargo dynamics facilitated by motor proteins : role of activity and a catch-bonded dynein"* submitted by **Ms. Nisha Gupta** (Reg. No. Ph13017) for the partial fulfillment of Doctor of Philosophy programme of the Institute, has been examined by the thesis committee duly appointed by the Institute. The committee finds the work done by the candidate satisfactory and recommends that the report be accepted.

Dr. Rajeev Kapri	Dr. Sanjeev Kumar	Dr. Abhishek Chaudhuri (Supervisor)

Declaration

The work presented in this dissertation has been carried out by me under the guidance of Dr. Abhishek Chaudhuri at the Indian Institute of Science Education and Research Mohali.

This work has not been submitted in part or in full for a degree, a diploma, or a fellowship to any other university or institute. Whenever contributions of others are involved, every effort is made to indicate that clearly, with due acknowledgement of collaborative research and discussions. This thesis is a bonafide record of original work done by me and all sources listed within have been detailed in the bibliography.

Nisha Gupta
(Candidate)
29th November 2019

In my capacity as the supervisor of the candidate's doctoral thesis, I certify that the above statements by the candidate are true to the best of my knowledge.

Dr. Abhishek Chaudhuri
(Supervisor)

Acknowledgements

This thesis would not have been completed without the support and association of many people. I gladly extend my appreciation and sincere gratitude to all those who made this Ph.D. thesis possible.

First of all I would like to extend my sincere gratitude to my Ph.D. supervisor, Dr. Abhishek Chaudhuri. Joining Dr. Abhishek Chaudhuri has definitely changed my thinking process in great ways. He is the most patient and positive person that I have seen. He introduced me to soft condensed matter physics and we had many discussions on computational techniques as well. He is such an enthusiastic person that till this day I go to his office and get motivated by just seeing him working there. His immense knowledge, inspiration, encouragement, advice and continuous support has made it possible for me to complete my Ph.D. He has an integral view for research and has made a deep impression for working constantly in the direction of providing high-quality research. I have learnt extensively from him and that learning process was not limited to science only, to tackle the problems more calmly and being positive towards every situation are among few things that I learned along. I owe him lots of gratitude for showing this way of research and life. I thank him for his guidance and support and am really glad to have him as my supervisor. My special words of thanks go to Dr. Debasish Chaudhuri for his continuous support, encouragement, guidance and valuable comments and allowing me to visit IOP and work with him for some time.

Special thanks to my doctoral committee members, Dr. Sanjeev Kumar and Prof. Sudeshna Sinha for their guidance and support from time to time. I owe a lot of gratitude to Dr. Rajeev Kapri for always being there for discussion and advise. One of his great advise is ”start working and focus on one task at a time and you’ll reach the end eventually”. His friendly nature has always made me feel at ease and I could look back to him for any support.

I would also like to acknowledge Prof. N. Sathyamurthy (Former Director), Prof Debi Sarkar (Former Director), and Prof. Arvind (current Director), Prof. Purnananda Guptasarma (Former Dean R& D), Prof. Sanjay Mandal (Dean Acad.), Prof. Jasjeet Singh Bagla, Dr. Harvinder Jasal, Dr. Dipanjan, Prof. Kavita Dorai and other members of physics department for their kind support in administrative and academic aspects whenever I needed them. I also acknowledge high performance computing facility that has been provided to us here at IISER Mohali. I feel privileged to be part of IISER Mohali community. I must thank the technical and office staff, Garima, Sunny, Ramshankar, Deepika, Anuj, Brijesh, Santosh and Satinder. I express my heartfelt gratitude to hostel cleaning staff specielly to Geeta aunty and Dharam Kaur aunty

for being with me as elderly figures through out. I also acknowledge my neighbours for their constant support and cooperation during the stay at IISER Mohali.

My heartfelt thanks to my seniors Dr. Rajneesh, Sameep Chandel, Dr. Subhadip, Dr. Moutushi, Dr. Iyyappan, Dr. Suman Kalyan, Dr. Preeti, Dr. Jebarathinam for moral support and delightful discussions. They always helped me out when I faced any difficulties or had any queries. Sameep has also contributed in the second part of my work on intracellular transport. I am extremely fortunate to have an enthusiastic and talented proofreader, Dr. Subhadip. His sharp eyes and hard work did much to make this thesis better. I extend my gratitude to fellow group mates, Aman, Debsuvra, Love, Sandip, Gokul, Subhashree, Anweshika, Sougata, Vishnu, Madhuvanthi, Misha, Nimisha, Shubham, Yash, Khush for cheerful gatherings and trips that we had together.

A special mention of thanks to my M.Sc. thesis advisor Prof. T.R. Seshadri for his constant encouragement, inspiration and valuable discussions. My special regards to all my teachers throughout my life because of whose teaching at different stages of education has made it possible for me to see this day. Because of their guidance and vision I was able to reach a stage where I could write this thesis.

Special acknowledgement to my M.Sc. friends Subash, Sumit Keshari, Sumit Sinha and Ravinder for showing confidence in me and always being avlaible as compassionate friends. They hold special place in my heart. My heartiest thanks to my close friends Sumit Mishra, Vandana, Surender Goyal, Meenakshi, Pushpendra, Archana and Shradha with whom I have shared valuable moments and has been a constant support in good and bad times. I have and will always cherish the warmth and affection shown by them. Special thanks to Sumit Mishra and Vandana for bearing with me during the hardest time of my life. I also thank Dr. Ashutosh, Vivek, Anita, Dr. Dahlia, Dr. Smriti, Dr. Amandeep, Varinder, Dr. Satnam, Dr. Gopal Verma, Gyanendra, Manvendra, Ankit, Hemanshu, Sumit and Tarun for delightful moments.

I feel a deep sense of gratitude for my Nani(grand mother), mother, father, who taught me good things and being the reason of my positive vision towards life. Their support and infallible love has always been my strength. The lessons taught by them will always inspire me throughout the life. I am also very much grateful to my brother, Ashwini Gupta for his love, affection and encouragement. I thank God for my nephew Ayan Gupta who has been dear to me and such a joyful bundle that I forget my worries instantly. I also thank my sister-in-law for her support.

I acknowledge UGC and MHRD (initially) for reseach fellowship.

List of Publications

1. **Nisha Gupta**, Abhishek Chaudhuri and Debasish Chaudhuri, *Morphological and dynamical properties of semiflexible filaments driven by molecular motors*, Physical Review E **99**, 042405 (2019).
2. Palka Puri*, **Nisha Gupta***, Sameep Chandel, Supriyo Naskar, Anil Nair, Abhishek Chaudhuri, Mithun K Mitra and Sudipto Muhuri, *Dynein catch bond as a mediator of codependent bidirectional cellular transport*, Physical Review Research **1**, 023019 (2019). (* equal contribution).

Abstract

The cytoskeleton of the cell is a highly complex, dynamic and adaptive system of semiflexible filaments with their associated motor proteins and cross-linkers. It generates internal stresses and responds to external ones, intermediates cell signaling, ensures the structural integrity and morphology of the cell and helps in the spatial organization of cellular contents. This dynamic regulation is effected by the coordination of the different cytoskeletal components : polymeric filaments such as microtubules, actin and intermediate filaments; cross-linker proteins such as fascin and α-actinin; and motor proteins such as dynein, kinesin and myosin.

Much of the physical understanding of the components of cytoskeletal network have been obtained through in-vitro experiments on cytoskeletal extracts. In a bead assay a cytoskeletal filament is irreversibly attached to a substrate, while the motor proteins moving on the filament are attached to a bead which is optically trapped. On the other hand, in a gliding assay setup, the geometry is inverted. Here, the cargo domains of motor proteins are irreversibly adsorbed on a glass substrate, while their filament binding domains attach to the complimentary cytoskeletal filament. In the presence of ATP, the motors move in a directed fashion along the length of the filament before detachment. This results in a gliding movement of the cytoskeletal filament in the opposite direction. Apart from a wealth of information on single motor protein movement and force generation, motility assays have revealed the emergence of collective motion in high densities of such filaments leading to the formation of clusters, swirls and interconnected bands. Within these in-vitro settings, it is possible to ask theoretical questions regarding both the role of individual motor proteins and their cooperative dynamics, in controlling the dynamics of the cargo/filament that they bind/unbind to/from and therefore make falsifiable predictions amenable to experimental verifications.

In the first problem, we consider an explicit model of a semiflexible filament moving in two dimensions on a gliding assay of motor proteins, which attach to and detach from filament segments stochastically, with a detachment rate that *increases* with the increase of local load force. Attached motor proteins move along the filament to one of its ends with a velocity that varies nonlinearly with the motor protein extension. The resultant force on the filament drives it out of equilibrium. We characterize the nonequilibrium conformations of the polymer comparing its end-to-end distribution with that of the equilibrium filament. In theoretical studies of active systems, key concepts such as broken detailed balance and entropy production have recently been used to characterize the distance of these systems from their equilibrium counterparts. We show that subtle changes in the local load dependence of detachment rate and active velocity of motor proteins lead to dramatic difference in the end-to-end distribution. With increasing activity, the difference increases, the effective bending stiffness reduces, and the polymer shows a phase coexistence between open and spiral chains. The most startling result is seen in the dynamics. The center of mass of the polymer shows a series of crossovers between ballistic and diffusive motion, controlled by its inertial, orientational and speed relaxation time scales, a significant result which can be checked in motility assay experiments.

In the second problem, we look at the effect of the dynein catch-bond on the intracellular bidirectional transport of cargo on microtubule filaments, achieved by the collective action of oppositely directed dynein and kinesin motors. Experiments have found that in certain cases, inhibiting the activity of one type of motor results in an overall decline in the motility of the cellular cargo in both directions. This counter-intuitive observation, referred to as paradox of codependence is inconsistent with the existing paradigm of a mechanistic tug-of-war between oppositely directed motors. Unlike kinesin, dynein motors exhibit catchbonding, wherein the unbinding rates of these motors *decrease* with increasing force on them. Incorporating this catchbonding behaviour in our theoretical framework, we show that this non-monotonic nature of the detachment kinetics gives rise to extremely non-trivial cooperative effects for bidirectional transport. Using measures like the average processivity, probability distributions of run and pause times and cargo trajectories, we show that in an experimentally viable parameter space, the wide range of results - from those which are in agreement with the conventional “tug-of-war” model to the ones which are in contradiction - are all correctly reproduced, therefore providing a plausible resolution of the paradox of codependence. The proposed framework necessitates a reassessment of existing experimental data in the light of our predictions, and will enhance the fundamental understanding of intracellular motor- driven processes, which have consequences for the overall spatiotemporal organization within the cell, cellular motility and cell division.

Contents

1 Introduction **3**

1.1 The Cell cytoskeleton . . . 3
  1.1.1 Cytoskeletal filaments . . . 4
    1.1.1.1 Actin filaments . . . 4
    1.1.1.2 Microtubules . . . 5
    1.1.1.3 Intermediate filaments . . . 5
  1.1.2 Motor Proteins . . . 5
    1.1.2.1 Myosin Motor . . . 6
    1.1.2.2 Kinesin Motors . . . 7
    1.1.2.3 Dynein Motor . . . 7
1.2 In vitro experiments . . . 8
  1.2.1 Gliding assay . . . 9
  1.2.2 Bead assay . . . 11
1.3 Theoretical modeling: biopolymer . . . 11
  1.3.1 Wormlike chain model . . . 12
    1.3.1.1 Tangent-tangent correlation . . . 13
    1.3.1.2 Mean squared end to end distance . . . 13
    1.3.1.3 Probability distribution of end-to-end vector . . . 14
  1.3.2 Simulation techniques . . . 15
    1.3.2.1 Langevin dynamics . . . 15
    1.3.2.2 Simulation results . . . 16
1.4 Theoretical modeling : Molecular motor . . . 18
  1.4.1 Binding and unbinding rates . . . 18
  1.4.2 Motor velocity . . . 18
1.5 Organization of the Thesis . . . 21

2 Morphological properties of a semiflexible filaments on a motor protein substrate **23**

2.1 Theoretical models 24
2.2 Limitations of earlier studies 25
2.3 Model and Simulations 25
2.4 Results 28
    2.4.1 Polymer morphology in the presence of motor proteins 29
    2.4.2 Dependence on Peclet number 32
2.5 End-to-end distributions for different Ω 33
    2.5.1 Competition between activity and bending stiffness 33
    2.5.2 Determination of effective stiffness 35
    2.5.3 Coexistence of spiral and open chains 38
2.6 Conclusions 38

3 Dynamical properties of a semiflexible filament driven by molecular motors 41
3.1 Anomalous dynamics of the center of mass 41
3.2 Can an effective polymer model describe the dynamics? 45
3.3 Ballistic to diffusive cross overs 46
3.4 Conclusions 50

4 Dynein catch bond as a mediator of codependent bidirectional cellular transport 53
4.1 Modelling dynein catch bond. 55
4.2 Theory and Simulation 58
    4.2.1 Model 58
    4.2.2 Methods 60
        4.2.2.1 Stochastic Simulation Algorithm (SSA) with equal load sharing 60
        4.2.2.2 Brownian dynamics with stochastic load sharing . . . 61
4.3 Results 63
    4.3.1 Cargo Processivity Characteristics 63
    4.3.2 Probability distribution of runtimes and cargo velocities . . . 67
    4.3.3 Quantitative comparison with experiments 70
4.4 Conclusion 70

5 Motility diagrams for bidirectional transport in the presence of dynein catch bond 73
5.1 Master equation 74
5.2 Motility states 75

5.2.1 Symmetric tug-of-war 76
    5.2.1.1 Probability Method plots 76
5.3 Asymmetric tug-of-war 77
5.4 Discussion 79

6 Summary 81

List of Figures

1.1 The various cytoskeletal filaments, microtubule, actin filaments and intermediate filaments shown in the figure. Figure adapted from [3]. . . 3

1.2 Dynein motor is shown to be attached to a gray sphere which is the cargo. The attachment is via the intermediate and light chains shown in blue. The ring structure in each head domain is shown as six ATPase associated with the AAA domains shown in yellow. The microtubule shown in green is connected to the head domain by the binding stalk (in gray) coming out from the AAA4 and AAA5. Lower inset shows the two stages of the possible catch-bond scenrio. Left shows the R and L in the absence of force. Right shows the R and L when force is applied giving rise to a lock. Figure adapted from [17] 8

1.3 Mean squared end-to-end distance, $\langle R^2 \rangle$ for different lengths of the polymer, L, in two dimensions. Simulations and theory (Eq. 1.13) are in excellent agreement. 16

1.4 Probability distribution of end-to-end vector, $p(\tilde{r})$ for different u values in two dimensions. The distribution shows that for polymer with lower stiffness (large u) the peak is near $\tilde{r} \approx 0$ while that for higher stiffness (small u) is near $\tilde{r} \approx 1$. 17

1.5 (Color online) Force-velocity data for kinesin molecules at 2 mM ATP concentration extracted from Ref. [42]. The line is a fit to Eq. 1.25 with $v_0 = 0.807\,\mu\mathrm{m}\,s^{-1}$, $d_0 = 0.01$ and $f_s = 1.16$ pN. Figure adapted from [41] 20

2.1 (color online)(i) Schematic of the system showing the molecular motors arranged on a square grid. The semiflexible polymer glides on the bed of molecular motors. (ii) and (iii) Simulation snapshots of the polymer in an open and spiral state for a polymer with persistence ratio $u = 3.33$, under the influence of MP activity $Pe = 100$, and bare processivity ratio $\Omega = 5/6$.. 26

2.2 (color online) The end-to-end distribution of the semiflexible polymer at equilibrium $p_{eq}(\tilde{r})$ in the absence of motor proteins. Note that excluded volume interactions suppress the peak at $\tilde{r} = 0$. 28

2.3 (color online) The logarithm of the ratio of the end-to-end probability distributions of the filament under active drive with respect to that of the equilibrium polymer, $\Delta\Sigma$, provides a measure of the difference in distributions. The legends denote parameter values (detachment rate, MP velocity), where, in this figure, all data sets correspond to a constant detachment rate ω_0, and MP velocity varies between constant values 0, v_0, and stretching dependent active velocity v_t^a as denoted by Eq.(2.4). 30

2.4 (color online)The end-to-end distribution of stretchable semiflexible polymer $p(\tilde{r})$, with local strain dependent detachment $\omega_{\rm off}$ as in Eq.2.3. The variation of MP active velocities are as in Fig.2.3. 31

2.5 (color online) End-to-end distribution for three different values of Pe using stretching dependent turnover $\omega_{\rm off}$ for $N = 64, \Omega = 5/6, u = 3.33$. 32

2.6 (color online) End-to-end distribution at $Pe = 1$, 10, 100 for different values of bare processivity Ω, using stress dependent active velocity and detachment rate with $N = 64, u = 3.33$. The graphs correspond to (a) $\Omega = 2/3$, (b) $\Omega = 5/6$, and (c) $\Omega = 20/21$. 34

2.7 (color online) End-to-end distribution functions. We use constant detachment rate ω_0 with $\Omega = 5/6$ for all the figures. The variation of MP active velocities are as in Fig.2.3, with the non-zero active velocities set by $Pe = 1$. The three graphs show results for (a) $N = 64$, $u = 3.33$, $l_p = 18.92\,\sigma$. (b) $N = 128$, $u = 3.33$, $l_p = 38.14\,\sigma$ (c) $N = 128$, $u = 6.66$, $l_p = 18.92\,\sigma$. 36

2.8 (color online) Tanget-tangent correlation function for a chain of $N = 64, u = 3.33$, and activity v_t^a set by $Pe = 1, 10$ and 100 and load dependent detachment rate $\omega_{\rm off}$ with $\Omega = 5/6$. The data set *passive* denotes equilibrium result. The solid line shows a single exponential fit to $Pe = 10$ data used to extract the effective persistence length $l_p^{\rm eff} = (15.99 \pm 0.24)\,\sigma$. 37

2.9 (color online) Plot of turning number $\psi(s)$ for three different configurations with $Pe = 100$. It shows that $\psi(s)$ is an effective order parameter, distinguishing between the open state (green), clockwise spiral (blue) and anti-clockwise spiral (red). For $N = 64, u = 3.33$ and load dependent detachment ω_{off} with $\Omega = 5/6$ with activity v_t^a set by Pe. 39

2.10 (color online) Probability distributions for $\psi(L)$ using $N = 64, u = 3.33$ and load dependent detachment ω_{off} with $\Omega = 5/6$ at $Pe = 1, 10$ and 100. 40

3.1 (color online) Dynamics of center of mass for a chain of $N = 64, u = 3.33$, with load dependent MP activity v_t^a controlled by Pe and detachment rate ω_{off} determined by $\Omega = 20/21$. Mean squared displacement of the center of mass at different Péclet ($Pe = 1, 10, 100$). 42

3.2 (color online) Dynamics of center of mass for a chain of $N = 64, u = 3.33$, with load dependent MP activity v_t^a controlled by Pe and detachment rate ω_{off} determined by $\Omega = 20/21$. (Numerical analysis of the dynamics at $Pe = 100$ is presented. The gray line shows a center of mass trajectory. Structure of polymer corresponding to the blue, red, and green points indicated on the trajectory are shown in the respective colors. 43

3.3 (color online) Dynamics of center of mass for a chain of $N = 64, u = 3.33$, with load dependent MP activity v_t^a controlled by Pe and detachment rate ω_{off} determined by $\Omega = 20/21$. Numerical analysis of the dynamics at $Pe = 100$ is presented. The end-to-end length r_{ee} (red line), end-to-end orientation ϕ (green line), and root mean squared fluctuations of the center of mass position (blue line) for a single trajectory are shown as a function of time at $Pe = 100$. 44

3.4 (color online) Speed autocorrelation of the centre of mass of the polymer. Single exponential decays are observed for both $Pe = 1$, 10, with correlation times $t_s \approx 0.1\tau$, 1.0τ respectively. (Inset) In the log-log plot, for $Pe = 100$, multiple exponential decays with $t_s \approx 1\tau$, 250τ, 2000τ are shown. The three exponential fits are indicated by black points. 47

3.5 (color online) Orientational autocorrelation of the centre of mass velocity vector. This shows multiple exponential decays for all Pe. (Inset) For $Pe = 1$, the log-log plot shows multiple exponential decays with time scales $t_\theta \approx 1\tau$, 1500τ. The two exponential fits are indicated by black points. 48

3.6 (color online) Cross-correlation of the orientation and speed of the centre of mass velocity for $Pe = 1$ (red), 10 (green) and 100 (blue, and values correspond to right ordinate). 49

4.1 (Color online) Here we show the schematics of a dynein motor walking on a microtubule filament. Catch bond behavior is anticipated to be happening due to a conformational change at the microtubule binding domain of the stalk of the dynein motor. Adapted from [70] 56

4.2 Single dynein unbinding rate from experiments [113] (points) and the corresponding fit (solid line) from the TFBD model [130]. 57

4.3 Schematic of bidirectional motion of cargo (C) attached to both kinesin (K) and dynein (D) motors on a microtubule (MT) filament. 59

4.4 Average processivity as a function of N_- for $N_+ = 4$. The colored points and lines are obtained using SSA. The zero-force (un)binding rates for dynein are $\varepsilon_{0-} = \pi_{0-} = 1/s$. 62

4.5 Average processivity as a function of N_+ for $N_- = 4$. The colored points and lines are obtained using SSA. The zero-force (un)binding rates for dynein are $\varepsilon_{0-} = \pi_{0-} = 1/s$. 64

4.6 Average processivity as a function of N_+, as the bead size σ is changed. Note that the friction constant ζ changes as a result. The blue curve shows the corresponding result under the equal load sharing assumption. Here $N_- = 4$, $\alpha = 40$ and $F_o = 7pN$. 65

4.7 Contour plots for processivity obtained using SSA in the $N_+ - N_-$ plane for $F_{s-} = 1pN, \alpha = 0$, The color bar indicates the average processivity (in μm). The zero-force (un)binding rates for dynein are $\varepsilon_{0-} = \pi_{0-} = 1/s$. 66

4.8 Contour plots for processivity obtained using SSA in the $N_+ - N_-$ plane for $F_{s-} = 1pN, \alpha = 40k_BT$, The color bar indicates the average processivity (in μm). The zero-force (un)binding rates for dynein are $\varepsilon_{0-} = \pi_{0-} = 1/s$. 66

4.9 Probability distributions of runtimes for $N_+ = 2$, $N_- = 6$. The left panels show the normalized histograms and sample trajectories for dynein in the presence of catch bond ($\alpha = 40$). The right panels show the corresponding quantities in the absence of catch-bond ($\alpha = 0$). (a) and (e) Sample trajectories; (b) and (f) distributions of runtimes for plus directed runs (shown in green); (c) and (g) pause time distributions (shown in blue); (d) and (h) distributions of runtimes for minus directed runs (shown in red); and insets in (b) and (h) show magnified views of the corresponding distributions. 67

4.10 Probability distributions of runtimes for $N_+ = 6$, $N_- = 2$. The left panels show the normalized histograms and sample trajectories for dynein in the presence of catch bond ($\alpha = 40$). The right panels show the corresponding quantities in the absence of catch-bond ($\alpha = 0$). (a) and (e) Sample trajectories; (b) and (f) distributions of runtimes for plus directed runs (shown in green); (c) and (g) pause time distributions (shown in blue); (d) and (h) distributions of runtimes for minus directed runs (shown in red); and insets in (b) and (h) show magnified views of the corresponding distributions. 69

4.11 Histograms showing scaled (a) retrograde and (b) anterograde run lengths with *non-catchbonded* (Expected, red, $\alpha = 0$) and *catchbonded* (Observed, blue, $\alpha = 40k_BT$), when N_+ is changed from 3 to 2, while $N_- = 4$. The scaling is done with respect to the control (without kinesin inhibition) and corresponds to $N_+ = 3$. The zero-force (un)binding rates for dynein are $\varepsilon_{0-} = \pi_{0-} = 1/s$ 70

5.1 Motility diagram for symmetric tug-of-war using only dynein motor parameters with $\alpha = 0$. The number of motors are equal as are the various parameters. $N_+ = N_- = 5,\ F_d = 0.67\ pN,\ F_s = 1.5\ pN,\ F_0 = 7\ pN,\ \pi_0 = 1\ /s,\ v_f = 0.65\ \mu m/s,\ v_b = 1\ nm/s$. 77

5.2 Motility diagram for symmetric tug-of-war using only dynein motor parameters with $\alpha = 35$. The number of motors are equal as are the various parameters. $N_+ = N_- = 5,\ F_d = 0.67\ pN,\ F_s = 1.5\ pN,\ F_0 = 7\ pN,\ \pi_0 = 1\ /s,\ v_f = 0.65\ \mu m/s,\ v_b = 1\ nm/s$. Note that some parts are left white since the motility state could not be accurately determined from the probability maxima. 78

5.3 Motility diagrams in the $N_+ - N_-$ plane for (a) Weak dynein ($F_{s-} = 1pN$), and (b) Strong dynein ($F_{s-} = 7pN$). There are seven possible motility states, *fast plus* (+), *fast minus* (-), *no motion* (0), *fast plus with pauses* (0+), *fast minus with pauses* (0-), *fast bidirectional motion* (+-), and *fast bidirectional with pauses* (-0+). The parameter values used are the same as in Fig. 4.4. 78

Chapter 1

Introduction

The biological cell is a highly complex dynamical system which is capable of spontaneous movement, adaptation, changing shape, division, responding to the environment and organization [1]. A large number of these functions are carried out by the cell with the help of the cytoskeleton, a dynamic and adaptive system of biopolymers with their associated motor proteins and cross-linkers. It generates internal stresses and responds to external ones, intermediates cell signaling, ensures the structural integrity and morphology of the cell and helps in the spatial organization of cellular contents [2].

1.1 The Cell cytoskeleton

The cytoskeleton is a network of fibrous proteins that are throughout the cytoplasm of the cell. However, unlike a skeleton, this meshwork is not rigid. It is dynamic and

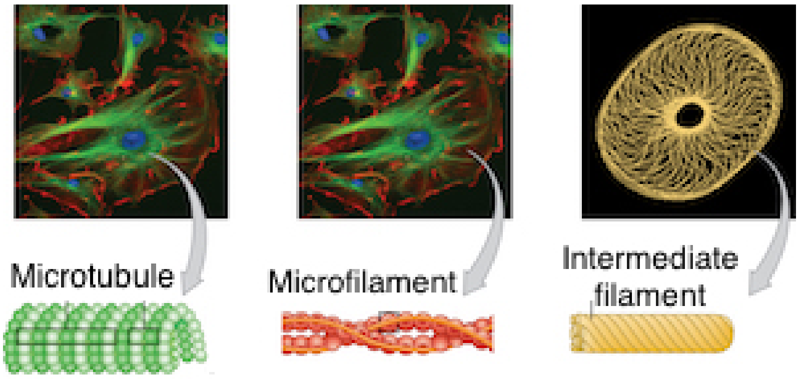

Figure 1.1: The various cytoskeletal filaments, microtubule, actin filaments and intermediate filaments shown in the figure. Figure adapted from [3].

adaptive, constantly growing and shrinking, assoicating and dissociating giving rise to viscoelatic properties. We first discuss the various cytoskeletal components which gives rise to this dynamic network.

1.1.1 Cytoskeletal filaments

Cytoskeletal filaments are biopolymers made up of protein subunits. There are three types of cytoskeletal filaments : actin filaments, mictotubules and intermediate filaments. All these together form networks which give shape and stability to the cell as well as reorganize if necessary. The organization and integrity of cellular compartments are also maintained by this network of polymers. The various cytoskeletal filaments are differentiated by their structure, mechanical properties and the motor proteins that they are associated with. Biopolymers like the cytoskeletal filaments show high rigidity when compared to their synthetic counterparts and are examples of semiflexible polymers. Semiflexible polymers have suffiicient bending stiffness such that the energetic propensity to have a fairly straight conformation competes with the entropic propensity to collapse into a random coil [4]. This competition gives rise to several unique physical properties not only in single polymers but also in semiflexible polymer networks where there are polymer-polymer interactions. Thus such networks show unique elastic and viscoelastic properties. The quantification of the bending stiffness of the polymer is given by the *persistence length*. This measures the length over which the polymer appears straight in the presence of thermal fluctuations.

1.1.1.1 Actin filaments

Actin filaments are made up of the protein called actin and are two stranded helical polymers. Actin filaments are mostly near the cell cortex, lying below the plasma membrane in an eukaryotic cell. They have diameters of the order of $5-7$nm and are structurally polar. The polarity is due to their structurally asymmetric subunits. Actin filaments are not very rigid with their persistence length of the order $15-17\mu$m [5]. However, inside the cell, accessory proteins acts as crosslinkers, bundling multiple actin filaments to form organized, stiff networks. For example, in filipodia, actin filaments bundle and align giving rise to filopdial protrusions which help the cell to move in the direction of a chemical gradient as well as in cell-cell communication. The two ends of the actin filament polymerize and depolymerize by adding and removing subunits with rates k_{on} and k_{off} [6]. k_{on}, is higher in the plus side of the polar actin filament compared to the negative side, giving rise to a difference in local concentration of free subunits at the two ends. If the concentration is in some intermediate range, then the addition and removal of subunits can lead to the phenomena of “treadmilling”, when the length of the filament is constant with a net flux of monomers through th polymer.

1.1.1.2 Microtubules

Microtubule is made up of the protein called tubulin and its structure is hollow and cylindrical. The tubulin heterodimer is made up of two types of tubulin, α and β tubulin, which together gives rise to the helical structure. The diameter of a microtubule is of the order of 25nm which is much bigger than the actin filament. Hence, microtubules are much stiffer compared to actin and have persistence lengths of several millimeters. The hollow cylindrical structure of the microtubule is made up of 13 parallel protofilaments [5]. Each protofilament consists of alternating α and β tubulin molecules, with each subunit (the heterodimer) pointing in the same direction, giving rise to structural polarity in the microtubule, with α tubulins at one end and β tubulins in the other. There is a microtubule organizing center called centrosome and the microtubules in a cell are typically organized radially from it, with the nucleation of microtubules happening at the centrosome with their minus ends. The plus ends grow towards the cell cortex in a star like “atrsal” conformation.

1.1.1.3 Intermediate filaments

The family of proteins making up the intermediate filaments are themselves elongated and fibrous. This gives rise to long fibers with diameters of 10nm. Intermediate filaments have the minimum stiffness of all the cytoskeletal filaments with persistence lengths $\sim 0.3 - 1\mu$m [5]. Crosslinking proteins such as plectins crosslink intermediate filaments together or with actin filaments and microtubules. A major difference of intermediate filaments with the other two cytoskeletal filaments is that they are not polar. Therefore, they do not support the movement of motor proteins in a directed fashion. Thus, intermediate filaments mainly provide structural rigidity to the cell.

1.1.2 Motor Proteins

Molecular motors are proteins and protein complexes which convert chemical energy into mechanical work. There are a large class of molecular motors that exist in biology, primary examples being rotary motors and linear stepping motors. One example of the rotary motor is that used by bacteria to swim. It uses ion flux down an electrochemical gradient which causes the bacterial flagellum to rotate at a frequency of

100Hz. Some bacteria like *Escherichia coli* spin their flagellar motor in both directions while others do in in one direction only, although the speeds and the frequency of pauses are modulated in both [7]. Of all the classes of molecular motors, linear stepping motors are the most common for eukaryotic cells. These molecular motors bind to specific cytoskeletal filaments and move along them by hydrolyzing ATP and undergoing extensive conformational changes. These molecular motors can be further classified into *processive* and *non-processive* molecular motors [8]. Processive motors walk along the filament carrying cargo and are heavily involved in intracellular trafficking. On the other hand, non-processive motors are usually involved in generating contractile forces, examples being stress fibers and contractile rings formed during cytokinesis [9]. Processivity is related to the *duty ratio*, Ω which refers to fraction of the ATPase cycle that the molecular motor spends strongly bound to corresponding cytoskeletal filament. The primary motor proteins of this class are *myosins, kinesins* and *dyneins*.

1.1.2.1 Myosin Motor

Myosin, is found in all eukaryotic cells and regulates the contraction of muscles. Myosin is a family of motor proteins [10], all of which have a motor *head* domain which undergoes conformational changes during ATP hydrolysis and connects to the filament track and a *tail* domain that attaches to the cargo that it carries. The filament track for myosin [11] is the actin filament. The head domain consists of two motor heads which are identical and are called motor domains. Each motor domain consists of a catalytic domain and about 8 nm long lever arms. The heads are connected to the filament track through a coiled coil which in turn is made up of two helical coils. The tail domain is generally different for the different classes of myosin filaments. Myosin II family is involved in muscle contraction. Myosin V is a processive myosin motor involved in transport of pigment granules in mammalian skin cells. Myosin VI is a minus-end directed motor as opposed to all other myosin types.

For processive myosin, motion happens via a “lever-arm” model where one of the motor heads first bind to the actin filament while the other head is free. The catalytic domain in the attached head is weakly bound with ADP and P_i bound to it. Upon attachment, P_i is released and the lever arm is thrown counterclockwise due to conformational change pushing the actin filament by 10nm. ADP is now released from the bound head and with ATP taking its place, the binding again becomes weak for the head to be completely detached from the filament. The cycle then keeps repeating.

1.1.2.2 Kinesin Motors

The structure of kinesin [12] motors are very similar to that of myosin and they are believed to have originated from a common ancestor. Their head domains are similar while their tail domains are different. All known kinesin family of motor proteins are processive and they are associated with the microtubule. Kinesin motors are super processive - they travel long distances on micrtotubule tracks for many enzymatic cycles before detachment [13, 14].

Kinesin I walks on the microtubule track in a manner which is very different from the myosin motor. They move via a hand-in-hand mechanism where one motor domain binds to the microtubule track. Then the motor domain undergoes conformational changes driven by the hyrdolysis of ATP such that the other motor head domain is propelled forward which then binds to a microtubule binding site [15]. This cycle continues and the kinesin moves towards the plus end of the microtubule in steps of about 8nm [16].

1.1.2.3 Dynein Motor

The dynein family of proteins are associated with microtubule like kinesin. However, most dyneins are minus-end directed unlike kinesins. Cytoplasmic dyneins carry cargo and are therefore involved in intracellular transport. Axonemal dyneins help in the bending of cilia and flagella [18–28]. Dynein belongs to AAA class of proteins which makes it structure very different from kinesin and myosin. Six AAA domains are arranged in a ring in each of the two head domain of the dynein motor. The force generating arm of dynein which connects to the microtubule binding domain is 25nm. This is fairly long compared to the kinesin arm and indeed dynein does not undergo the hand-over-hand stepping of kinesin motor. Dynein movement is stochastic or coordinated depending on the tension and distance between the two heads. Dynein function is weak and erratic, frequently detaching and diffusing and takes sidesteps and back-steps while walking.

One of the most interesting aspects of dynein arises in its detachment characteristics. Several experiments have reported that unlike kinesin which detaches rapidly from the microtubule under forces above the stall force, the situation for dynein is markedly different. Beyond forces greater than the motor's maximal force, dynein shows a *catch-bond* behavior where application of force prolongs bond lifetime. The microscopic nature of the catch-bond mechanism in dynein is not understood. One

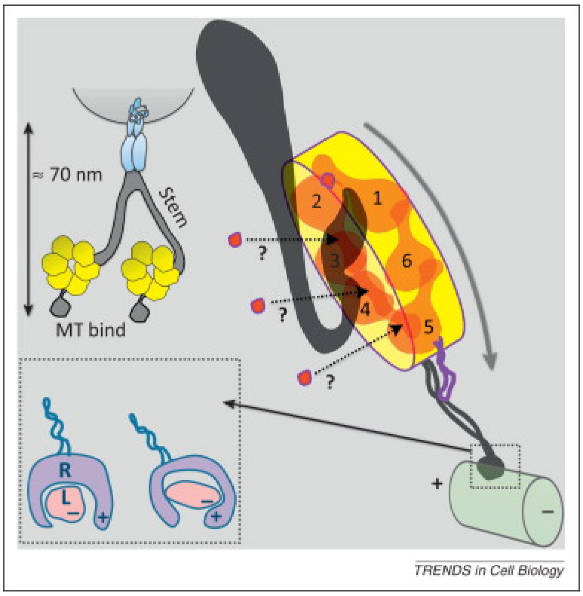

Figure 1.2: Dynein motor is shown to be attached to a gray sphere which is the cargo. The attachment is via the intermediate and light chains shown in blue. The ring structure in each head domain is shown as six ATPase associated with the AAA domains shown in yellow. The microtubule shown in green is connected to the head domain by the binding stalk (in gray) coming out from the AAA4 and AAA5. Lower inset shows the two stages of the possible catch-bond scenrio. Left shows the R and L in the absence of force. Right shows the R and L when force is applied giving rise to a lock. Figure adapted from [17]

.

possibility of what could be happening is shown in the Fig. 1.2 in the lower inset. Consider the attachment region of the dynein motor to the microtubule as a ligand-receptor binding with R representing the microtubule binding domain and L the domain on the surface of the microtubule. As force is applied, an allosteric deformation in R and L could cause a locking, therefore making the bond resistant to unbinding. The importance of the dynein catch-bond in intracellular cargo transport is explored in detail in Chapter 4 and 5 of this thesis.

1.2 In vitro experiments

The various cytoskeletal components including the filaments, motor proteins, cross-linkers and other accessory proteins have been extensively characterized *in vitro*. Such experiments have revealed that the complex cytoskeletal structures that are observed in the cell can be reconstituted from the basic components. In a minimal reconstituted system with three fission yeast proteins Mal3, Tip1 and the kinesin Tea2, Bieling et.

al [29] demonstrated microtubule plus-end tracking. A mixture of microtubules and motor proteins spontaneously form radially symmetric arrays similar to what is observed in the cell. Further experiments using extracts from *Xenopus laevis* ova assemble bipolar spindles around plasmid DNA coated polystyrene particles. This is evidence of spindle self-assembly in the absence of centrosomes and kinetochores. Thus *in-vitro* experiments helps us identify the minimal players required to give rise to the complex dynamical organization of cytoskeletal components inside the cell.

Molecular mechanisms of force generation by motor proteins have been studied using optical traps, atomic force microscopy and fluorescence techniques. These techniques allows for the visualization and manipulation of single motor proteins for instance, in a bead assay where the filament is irreversibly attached to a substrate, while the motor proteins moving on the filament are attached to a bead which is optically trapped. On the other hand, in a gliding assay setup, the geometry is inverted. Here, the cargo domains of motor proteins are irreversibly adsorbed on a glass substrate, while their filament binding domains attach to the complimentary cytoskeletal filament. In the presence of ATP, the motors move in a directed fashion along the length of the filament before detachment. This results in a gliding movement of the cytoskeletal filament in the opposite direction. Here, we review some of the experimental results in these two *in-vitro* set-ups.

1.2.1 Gliding assay

Sliding movement of actin filaments on myosin heads was first studied by Kron et. al. [30] and the conventional in-vitro motility assay was established. Here, myosin molecules are adsorbed onto glass coverslip surface and fluorescently labeled actin filaments slide over myosin heads. Toyoshima et. al. [31] refined this experimental assay and showed that even the tailless proteolytic fragments of actin, heavy meromyosin and the subfragment-1 (S1) enabled gliding movement of actin filaments. Using a thin and flexible micro-needle to which the actin is attached, Kishino and Yanagida [32] measured the force exerted by a single actin filament when it interacts with the myosin motors. The forces measured were 0.8pN, comparable to the average force per cross-bridge in muscle. Further studies were done to show the effects of changing the ionic strength, pH and the change of temperature on the movement of filaments. One of the key findings in the assay experiments using actin and myosin was to show that even single headed myosins were able to move actin filaments. Further, the actin velocity was mostly independent of the length of the filament and the density of myosin on the substrate. Howard et. al. [33] used bovine brain kinesin absorbed on a glass surface to see the movement of microtubules. They showed that a single kinesin can move a microtubule for several micrometres. Further, the speed of microtubule movement at high ATP concentrations is found to be independent of the number of kinesins. Hunt et. al. [34] in experiments on microtubules moving on a glass surface coated with kinesin motors showed that increasing the viscosity of the buffer solution, increased the drag on the microtubule filaments. The speed of a microtubule filament was observed to be linearly dependent on the drag force loading the motor. They were also able to show that certain theoretical approaches to model molecular motors were not adequate. Bordieu et. al. [35] performed motility assay experiments on both actin filament and micrtotubule systems and demonstrated the role of defects in their dynamics. They showed that point like defects in the path of the gliding movement of these filaments on the substrate causes the filament to buckle and rotate uniformly around the defect point. This motion in a spiral around the pinning point was observed for both F-actin on myosin and microtubules on kinesin. Filaments rotated several times before breaking free from the pinning point. With increasing surface density of motor proteins, the rotations of the filaments slowed down and the radius of the sprial increased. A theoretical analysis to explain the results showed consistency with the experimental observations. Recent gliding assay experiments by Schaller et. al. [36] have shown the self organization of actin filaments to form coherently moving structures such as clusters, swirls and interconnected bands in a high density of fluorescently labelled filaments moving on a substrate of heavy meromyosin (HMM) proteins. These collective dynamic structures are a result of the cooperative effect of the interacting filaments in the presence of the active molecular motors. A similar motility assay experiment by Sumino et. al. [37] looked at the dynamics of micrtoubules moving on a surface decorated with dynein motors. At high densities of the filaments, colliding microtubules which are on the average 15μm in length, self organized into large scale vortices of diameters around 400μm. The micrtoubules inside the vortices rotated both in the clockwise and anti-clockwise directions. At long times, a lattice of vortices is formed.

Such gliding assays of actin filaments and microtubules in the presence of crosslinkers forms circular structures like rings and spools as well as bundles [38]. A ring consists of a single filament or a filament bundle that forms a closed loop by crosslinking to itself, while a spool is formed when the filaments join along the length. The rings and spools continue to grow and rotate as more and more filaments are incorporated. Unsurprisingly, the size of the spools depend on the persistence length of the filaments with microtubules forming spools of bigger diameters.

1.2.2 Bead assay

Sheetz and Spudich [39] separated the cytoskeletal filaments from cells of the alga *Nitella*. Then they coated tiny plastic beads, 0.7μm in diameter with heavy meromyosin (HMM) molecules and put them on the cytoskeletal filaments kept on a substrate. In the presence of ATP, the beads were attached to the filaments via the myosin motors. The motors moved unidirectionally depending on the structural polarity of the actin filaments. This study confirmed the sliding filament mechanism in muscle. Using a fluorescent dye to attach to kinesin molecules, Vale et. al. [14] directly visualized the movement of kinesin on microtubule filaments by low background total internal reflection fluorescence microscopy (TIRFM). This proved that kinesin could walk on filaments even in the absence of cargo and secondly both head motor domains are required for movement, confirming the hand-over-hand long distance motion of kinesin on a microtubule filament. Another set of experiments involve the use of probe particles linked to the molecular motor via biotin and streptavidin molecules. The probe particles that were used included polystyrene beads, magnetic beads and gold colloidal particles. The advantage of these probe particles is the possibility of indirect visualization of motor protein dynamics and to apply forces on these motors. A large number of optical trap and magnetic tweezer experiments have been performed which has revealed the dynamics of the motor proteins and their energetics. However, the probe particles used are of sizes much larger than the motor proteins and therefore reveal indirect information. The interaction of the motor protein with the probe particle can often be overlooked in such experiments.

1.3 Theoretical modeling: biopolymer

As discussed previously, cytoskeletal filaments, are more rigid than synthetic polymers and in a coarse grained sense can be characterized in terms of their elasticity. These filaments are also long enough to show thermal bending fluctuations and are thus best described as *semiflexible* polymers. A measure of the bending stiffness exhibited by these filaments is the persistence length. The persistence length and the filament stiffness share a direct relationship only in thermal equilibrium. If κ is the bending stiffness of the filaments and l_p its persistence length, then in d-dimensions,

$$\frac{\kappa}{k_B T} = \frac{(d-1)l_p}{2}. \tag{1.1}$$

1.3.1 Wormlike chain model

This is the continuum version of the model first proposed by Kratky and Porod. Let us consider a continuous curve in space and denote s as the distance of a point on the chain from one of the end points of the chain, with the distance measured along the contour of the curve. The vector $\vec{r}(s)$ describes a point on the curve and completely specifies the curve. The tangent vector at a point s on the curve is given by

$$\hat{t} = \frac{\partial \vec{r}(s)}{\partial s}. \tag{1.2}$$

Now $\vec{dr} \cdot \vec{dr} = ds^2$. Hence we have $\hat{t} \cdot \hat{t} = 1$. $\hat{t}$ is therefore a unit vector which is tangent to the curve at the point s. With these definitions, we can now write down the bending energy of a polymer described as a continuous curve of contour length L as

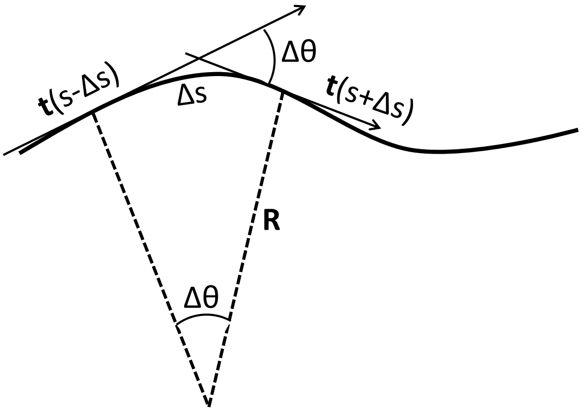

$$H_{\text{bend}} = \frac{\kappa}{2} \int ds \left| \frac{\partial \vec{t}}{\partial s} \right|^2 \tag{1.3}$$

where κ is the bending modulus with units of energy times length. It is easy to see that a length scale automatically emerges if one considers $k_B T$ as the unit of energy as $l_p = \kappa / k_B T$ which is the persistence length. To see the emergence of the bending energy as written down in Eq. 1.3, note that the curvature of the polymer is given as

$$\mathcal{H}(s) = \frac{1}{R} = \lim_{\Delta s \to 0} \frac{\Delta \theta}{\Delta s}. \tag{1.4}$$

If $\Delta\theta$ is the change in the angle between points separated by a distance Δs along the contour, then

$$\begin{aligned}\cos(\Delta\theta) &= \hat{t}(s-\Delta s/2)\cdot\hat{t}(s+\Delta s/2)\\ &= 1-\left(\frac{\partial\vec{t}}{\partial s}\right)^2\left(\frac{\Delta s}{2}\right)^2+\left(\vec{t}\cdot\frac{\partial^2\hat{t}}{\partial s^2}\right)\left(\frac{\Delta s}{2}\right)^2+O(\Delta s^3). \qquad (1.5)\end{aligned}$$

Differentiating the equation $\hat{t}\cdot\hat{t}=1$ twice, with respect to s, we get $\hat{t}\cdot\partial^2\hat{t}/\partial s^2+(\partial\hat{t}/\partial s)^2=0$. When substituted in Eq. 1.5, we get

$$\begin{aligned}1-\frac{1}{2}\Delta\theta^2 &= 1-\frac{1}{2}\left(\frac{\partial\vec{t}}{\partial s}\right)^2\Delta s^2\\ \mathcal{H}(s)=\left|\frac{\Delta\theta}{\Delta s}\right| &= \left|\frac{\partial\hat{t}}{\partial s}\right|=\left|\frac{\partial^2\vec{r}(s)}{\partial s^2}\right|. \qquad (1.6)\end{aligned}$$

Noting that the bending energy should be a quadratic in the curvature gives us Eq. 1.3

1.3.1.1 Tangent-tangent correlation

In terms of the angle θ given above, a discrete approximation of Eq. 1.3 gives, $\sum_i(\Delta\theta_i)^2/\Delta s$. If $\Delta\theta_i$ are considered as independent degrees of freedom, then by the equipartition theorem,

$$\langle\Delta\theta_i^2\rangle=\frac{k_BT\Delta s}{\kappa}. \qquad (1.7)$$

The thermal average, $\langle\cos(\theta_m-\theta_n)\rangle=\langle\cos(\Delta\theta_m)\rangle^{m-n-1}$. Then the tangent-tangent correlation function can be shown to decay as

$$\langle\hat{t}(s)\cdot\hat{t}(s')\rangle=e^{-|s-s'|/l_p}. \qquad (1.8)$$

1.3.1.2 Mean squared end to end distance

We can calculate the mean square end-to-end distance of the WLC polymer using Eq. 1.8. In the discrete sense, if we think of the polymer as being made up of $n+1$ monomers, i.e. with n bonds, then the end-to-end vector is obtained by summing over all the bond vectors : $\vec{R}_n=\sum_{i=1}^{n}\vec{r}_i$. The mean squared end-to-end distance is then given as

$$\langle R^2\rangle=\langle\vec{R}_n\cdot\vec{R}_n\rangle=\sum_{i=1}^{n}\sum_{j=1}^{n}\langle\vec{r}_i\cdot\vec{r}_j\rangle. \qquad (1.9)$$

For an inextensible polymer with all bond vectors of the same length $b=|\vec{r}_i|$,

$\vec{r}_i \cdot \vec{r}_j = b^2 \cos\theta_{ij}$ where θ_{ij} is the angle between the two bond vectors. Substituting and using Eq. 1.8, we get

$$\begin{aligned} \langle R^2 \rangle &= \int_0^L \int_0^L e^{-|s-s'|/l_p} ds ds' \\ &= 2l_p L - 2l_p^2(1 - e^{-L/l_p}). \end{aligned} \tag{1.10}$$

For chains much longer than the persistence length,

$$\langle R^2 \rangle \approx 2l_p L \qquad \text{for} \quad L \gg l_p, \tag{1.11}$$

which is the ideal chain limit. For chains much smaller than the persistence length, $e^{-L/l_p} \approx 1 - L/l_p + L^2/2l_p^2 + ...$ In this limit,

$$\langle R^2 \rangle \approx L^2 \qquad \text{for} \quad L \ll l_p, \tag{1.12}$$

which is the rigid rod limit. In d-dimensions, the average mean square end-to-end distance takes the form

$$\langle R^2 \rangle = \frac{4\kappa L}{(d-1)k_B T} - \frac{8\kappa^2(1 - e^{-\frac{(d-1)Lk_B T}{2\kappa}})}{(d-1)^2 k_B^2 T^2}. \tag{1.13}$$

In three dimensions ($d = 3$) and using Eq. 1.1, Eq. 1.13 reduces to Eq. 1.10.

1.3.1.3 Probability distribution of end-to-end vector

Here we discuss the probability distribution of the end-to-end vector, $P(R, L)$, of a worm like chain assuming that its two ends are at a fixed separation R. For this spherically symmetric situation, the radial probability distribution, $S(R, L)$, is related to $P(R, L)$ as

$$S(R, L) = CR^{d-1}P(R, L) \tag{1.14}$$

where C is a constant equal to the area of a d-dimensional unit sphere. In dimensionless units, $\tilde{r} = R/L$ and $u = L/l_p$, the distribution can be written as

$$P(R, L) = \frac{1}{L^d} p\left(\frac{R}{L}, \frac{L}{l_p}\right) = \frac{1}{L^d} p(\tilde{r}, u). \tag{1.15}$$

In 2-dimensions, the area of the unit sphere, $d = 2\pi$. Therefore,

$$\begin{aligned} S(R,L) &= 2\pi R\frac{1}{L^2}p(\tilde{r},u) \\ &= 2\pi\tilde{r}\frac{1}{L}p(\tilde{r},u) \\ 2\pi p(\tilde{r},u) &= \frac{LS(R,L)}{\tilde{r}}. \end{aligned} \tag{1.16}$$

In order to obtain the conformational statistics of a worm like chain, like the mean squared end-to-end distance and the probability distribution of the end-to-end vector, we performed numerical simulations. Here, we briefly describe the numerical techniques to simulate a passive semiflexible polymer.

1.3.2 Simulation techniques

The polymer is modelled as beads connected by harmonic springs. The springs allow for a stretching energy given as

$$H_{\text{stretch}} = \frac{A}{2}\int_0^L ds\varepsilon^2(s), \tag{1.17}$$

where $\varepsilon(s) = \partial r/\partial s - t$ is the extensional strain and A is the bond stiffness. The total Hamiltonian for the semiflexible harmonic chain is then given as

$$H = H_{\text{bend}} + H_{\text{stretch}} \tag{1.18}$$

In the inextensible limit, $\varepsilon(s)$ can be neglected and the semiflexible harmonic chain reduces to the worm like chain model. The force is obtained by differentiating the Hamiltonian.

1.3.2.1 Langevin dynamics

The equation of motion for a ith monomer of the polymer is given as

$$m\frac{d^2\vec{r}_i}{dt^2} = \vec{f}(\vec{r}_i) - \zeta\frac{d\vec{r}_i}{dt} + \vec{\eta}_i = \vec{F}_i \tag{1.19}$$

where $-\zeta\frac{d\vec{r}_i}{dt}$ is the drag force and $\vec{\eta}_i$ is the random force which satisfies the fluctuation-dissipation theorem, $\langle\vec{\eta}\rangle = 0$ and $\langle\vec{\eta}(t)\vec{\eta}(t')\rangle = 2\zeta k_B T\delta(t-t')$. To solve Eq. 1.19, we use the velocity Verlet algorithm which updates the positions and velocities at every time step as

$$\begin{aligned}\vec{r}_i(t+\Delta t) &= \vec{r}_i(t) + \vec{v}_i(t)\Delta t + \frac{\Delta t^2}{2m}\vec{F}_i(t) \\ \vec{v}_i(t+\Delta t) &= \vec{v}_i(t) + \frac{\Delta t}{2m}(\vec{F}_i(t) + \vec{F}_i(t+\Delta t)). \end{aligned} \qquad (1.20)$$

This algorithm is suitably modified to deal with the random force. The semiflexible harmonic chain in the presence of the heat bath is allowed to evolve according to the equations described above for sufficiently long time to reach equilibration. Configurations of the polymer were generated from 50 initial conditions and for every initial condition the averaging of the results were done over 10^7 steps.

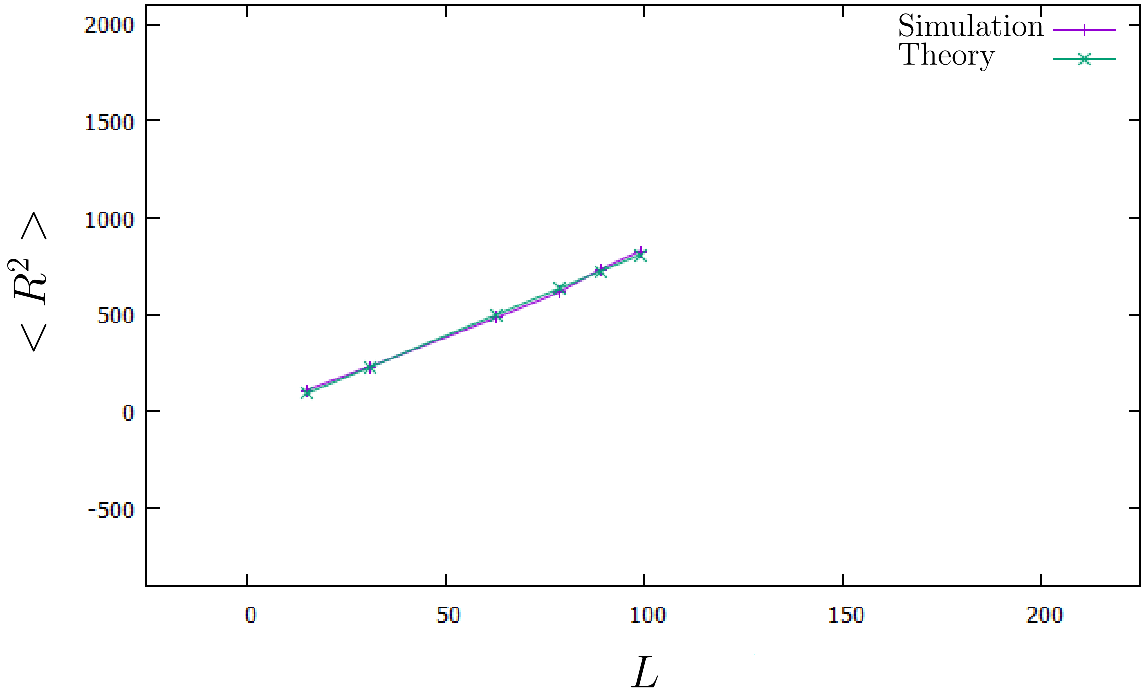

Figure 1.3: Mean squared end-to-end distance, $\langle R^2 \rangle$ for different lengths of the polymer, L, in two dimensions. Simulations and theory (Eq. 1.13) are in excellent agreement.

1.3.2.2 Simulation results

In Fig. 1.3, we show the mean squared end-to-end distance for different lengths of the polymer. The results are compared with the exact expressions obtained for a semiflexible polymer as in Eq. 1.13. Here we have compared results for 2-dimensions. As observed, the simulation results are consistent with the analytical results for varying lengths and stiffness of the polymer. Next we look at the probability distribution for the end-to-end vector of the polymer. Fig. 1.4, shows the result in two dimensions for $p(\tilde{r})$ as a function of $\tilde{r} = R/L$ for different values of $u = L/l_p$. For large u, i.e $L \gg l_p$, the polymer is in the ideal chain limit and $p(\tilde{r})$ shows a single maximum near $\tilde{r} = 0$. The polymer shows more coiled configurations. In the opposite limit of small u, i.e. $L \ll l_p$, the polymer is in the rigid rod limit and $p(\tilde{r})$ shows a single maximum near $\tilde{r} = 1$, i.e. $R = L$ as expected. In between the two limits, an interesting phenomena is observed as we change u. At some critical value of u, the probability distribution shows two maxima at nonzero values of $\tilde{r}$ [40]. This non-trivial feature appears due to the competing effects of polymer entropy which favors crumpled configurations and bending energy which tries to keep the polymer in the extended state.

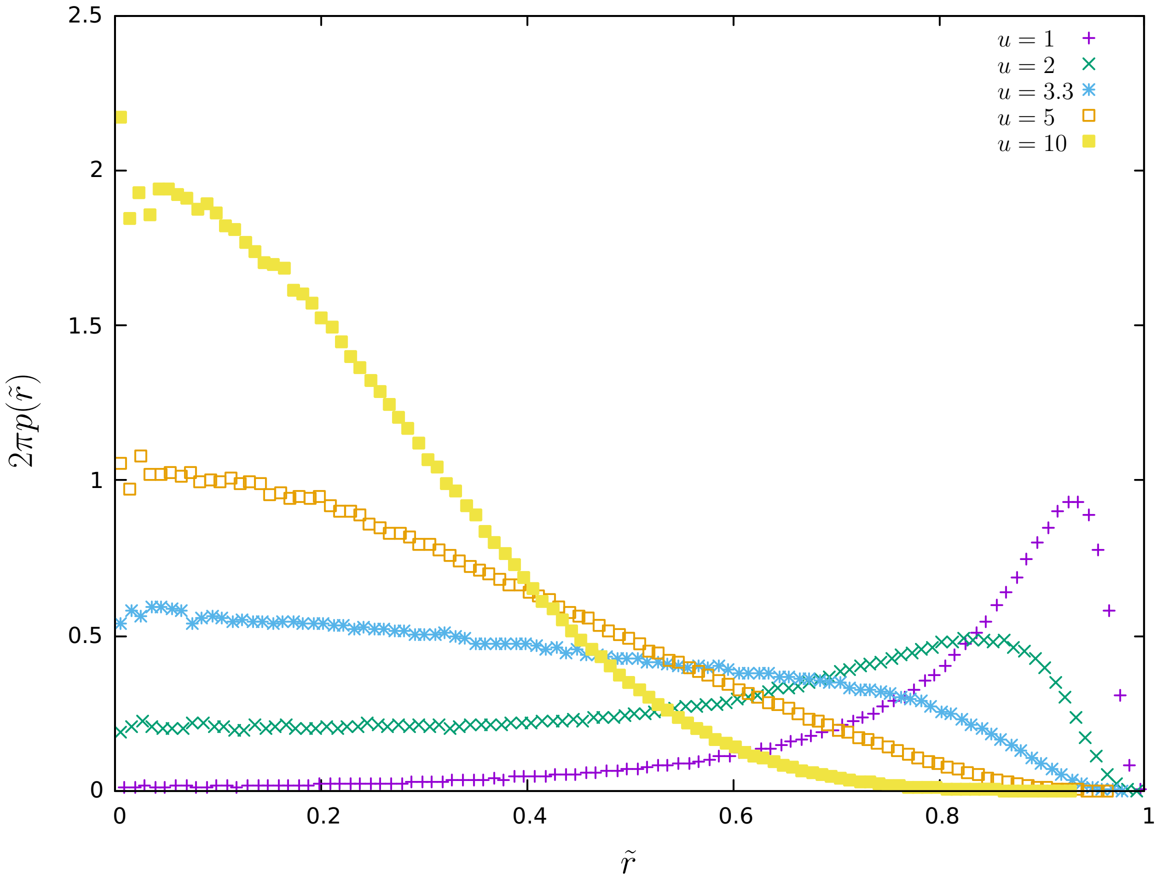

Figure 1.4: Probability distribution of end-to-end vector, $p(\tilde{r})$ for different u values in two dimensions. The distribution shows that for polymer with lower stiffness (large u) the peak is near $\tilde{r} \approx 0$ while that for higher stiffness (small u) is near $\tilde{r} \approx 1$.

1.4 Theoretical modeling : Molecular motor

To model the molecular motor, we focus our approach on the bead assay set up described before where the movement of a fluorescently labeled bead held by an optical trap and attached to a molecular motor is tracked as it moves along a filament. The motion of the bead is due to a force F that is applied by the optical tweezer and is considered a load force if it opposes the motion of the molecular motor. Our model for the molecular motor is a coarse grained one, with the motor characterized by a binding and unbinding rate which may depend on the load force.

1.4.1 Binding and unbinding rates

The binding step involves a diffusion of the bead with the molecular motor attached to it. If it comes within a certain distance of the filament it can bind to it. The binding process is a complex molecular process. In our approach, we neglect the molecular details and the diffusion step and instead consider the binding event as a single event with a probability which is constant in time. The binding event happens when the cargo-filament distance is within a capture radius r_c. The binding event is independent of the load force and is given as ω_{on}.

The unbinding rate on the other hand depends on the load force. Here again we consider the probability of unbinding to be constant in time and the bare unbinding rate, which is defined as the unbinding rate in the absence of load force, as ω_0. In the presence of load force, the probability of detachment increases. Therefore, the unbinding rate can be modeled according to the Bell's theory as

$$\omega_{\text{off}} = \omega_0 \exp\left(f_l/f_d\right) \tag{1.21}$$

where f_d is the detachment force and sets the scale. This exponential increase of the detachment rate with the load force is supported by *in-vitro* bead assay experiments on kinesin. Note that for dynein motors, which show catch-bond unbinding characteristics, this detachment rate will have to be modified. The modification will be discussed in Chapter 4.

1.4.2 Motor velocity

The final characterization of the molecular motors is their velocity in the bound state. In-vitro experiments have revealed the step length of molecular motors as they walk on the filaments. In the absence of any load force, the motor walks with a constant velocity v_0. In the presence of a load force, the motor slows down. As the load force is increased, the velocity of the motor $v_a^t(f_l)$ decreases further until it reaches the stall force f_s, when the motor stops. If load forces higher than stall force are applied, then the motor takes small backward steps although they can be mostly ignored. In our study, we have considered two models of motor velocity dependent on the load force.

- In the first model, the velocity is linearly dependent on the load force as

  $$v_a^t(f) = v_0(1 - f/f_s). \tag{1.22}$$

  This form is used in our study on bidirectional transport of cellular cargo in Chapters 4 and 5.

- In the other approach we look at the force velocity data for kinesin molecules and discuss the analysis presented in [41]. The velocity of the processive kinesin motor is dependent on the concentration of ATP and its dependence is reproduced using Michaelis-Menten kinetics [42]. As we had discussed before in the section on kinesin motors, the kinesin motor head M binds to ATP and undergoes ATP hydrolysis

  $$\mathrm{M} + \mathrm{ATP} \underset{r_d}{\overset{r_a}{\rightleftharpoons}} \mathrm{M.ATP} \xrightarrow{r_h} \mathrm{M} + \mathrm{ADP} + \mathrm{P}_i$$

  where r_a is the rate of binding of ATP to kinesin, r_d is the rate of unbinding and r_h is the rate of ATP hydrolysis. This gives the following dependence of the motor velocity

  $$v(f) = d\,r_h(f)\Psi([\mathrm{ATP}]) \tag{1.23}$$

  where d is the step taken by the kinesin motor per ATP hydrolysis, $K_M = (r_h+r_d)/r_a$ is the Michaelis-Menten constant, $\Psi([\mathrm{ATP}]) = [\mathrm{ATP}]/([\mathrm{ATP}]+K_M)$, [ATP] denotes ATP concentration.

  The time scale of hydrolysis can be divided into two time scales : (i) t_1 is the time required when force is absent and (ii) $t_2 \exp(f\delta/k_bT)$ the time required in the presence of a force. The second time scale is easy to understand from our discussion of unbinding rate of motor proteins (Eq. 1.21). $f\delta$ is the energy barrier to overcome with and δ is a characteristic molecular length scale. Therefore, the rate of ATP hydrolysis is given by $r_h(f) = 1/t(f) = 1/(t_1+t_2 \exp(f\delta/k_BT))$.

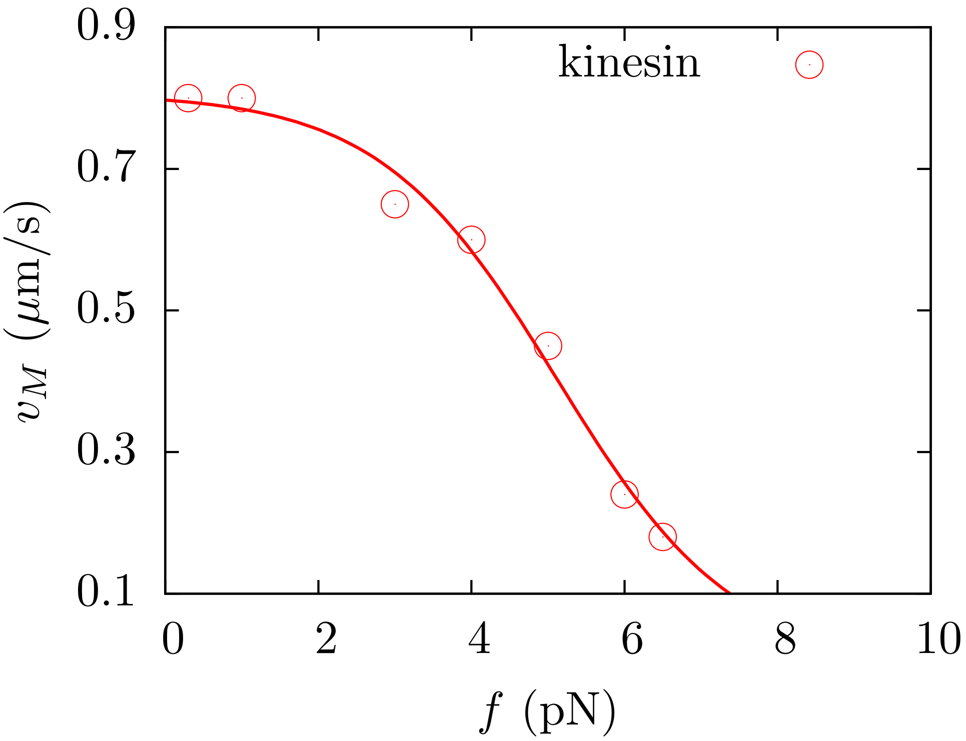

Figure 1.5: (Color online) Force-velocity data for kinesin molecules at 2 mM ATP concentration extracted from Ref. [42]. The line is a fit to Eq. 1.25 with $v_0 = 0.807\,\mu\text{m}\,s^{-1}$, $d_0 = 0.01$ and $f_s = 1.16$ pN. Figure adapted from [41]

So a general form for the rate of ATP hydrolysis can be written as [42],

$$r_h(f) = \frac{r_h(0)}{1 + d_0 \exp(f/f_s)} \tag{1.24}$$

where $f_s = k_B T/\delta$, $r_h(0) = 1/t_1$, $d_0 = t_2/t_1$. In the absence of load force, the motor slides with a velocity $v_0 = r_h(0) d\, \Psi([\text{ATP}])$ which at high enough concentration saturates to $v_0 = r_h(0)d$. Therefore, the motor velocity in the presence of load force in general can be written as

$$v_M(f) = \frac{v_0}{1 + d_0 \exp(f/f_s)}. \tag{1.25}$$

Fitting this form with kinesin force-velocity data obtained at large ATP concentration of 2 mM gives $v_0 = 0.807\,\mu\text{m}\,s^{-1}$, $d_0 = 0.01$ and $f_s = 1.16\,\text{pN}$ [42]. This expression of the motor velocity with the different parameters is chosen for our study on the transport of cytoskeletal filament on motor protein substrate in Chapters 2 and 3.

1.5 Organization of the Thesis

The thesis is organized as follows :
In Chapter 2, we consider an explicit model of a cytoskeletal filament moving in two dimensions on a substrate decorated with motor proteins. This mimics the *in vitro* gliding assay set up. The filament is modeled as a semiflexible polymer which glides on motor proteins modeled as elastic springs which stochastically attaches/detaches to/from the filament. The detachment rate increases exponentially with increasing local load experienced by the motor protein. When attached, the motors moves along the filament towards one of its ends. The velocity of the attached motor protein depends non-linearly on the extension of the spring. The filament which is driven out of equilibrium, moves in a direction opposite to that of the motor protein movement. We study the morphological properties of the polymer by looking at the end-to-end distribution and tangent-tangent correlations. End-to-end distributions show dramatic changes as the local load dependence of the detachment rate and the active velocity is varied. As active velocity is increased, the polymer shows a co-existence between open and spiral chains, which is quantified in terms of an order parameter.

In Chapter 3, we continue the study of a semiflexible filament on a motor protein substrate, now focusing on the dynamics of the polymer chain in the presence of activity due to the motor proteins. Specifically, we look at the mean squared displacement of the polymer center of mass as a function of time as the active velocity is increased. This shows multiple ballistic-diffusive crossovers unlike any other active matter system. We further quantify these crossovers in terms of the end-to-end extension, orientation of the end-to-end vector and the root mean squared fluctuation of the center of mass position along a single trajectory. We show that the multiple crossovers cannot be explained using an effective active polymer model which predicts a single crossover. Rather this can be explained by identifying three relaxation time scales, the inertial, orientational and speed relaxations times of the center of mass velocity. The existence of multiple time scales is quantified in terms of autocorrelations of the center of mass velocity vector, focusing on the speed and orientation separately.

In Chapter 4, we turn our attention to motor protein specific attachment/detachment properties and their role in guiding intracellular transport. In the previous study we had assumed that the detachment rate of motor proteins increases with increasing local load force, a feature reminiscent of a *slip* bond. While this is in general true for most motor proteins, dynein shows a different detachment characteristic. Experiments have revealed that dynein detachment rate follows a *slip-catch-slip* behavior : increasing for small load forces up to a force value, then decreasing as the force is increased and finally increasing at large force values. Incorporation of this effect into the gliding assay problem is a natural choice. However, we first attempted to look at how one of the most well studied phenomena of bidirectional transport of cargo by two sets of motor proteins, kinesin and dynein, affected by this non-monotonic change in the detachment characteristics of dynein. We show that incorporation of a catch bond detachment rate in dynein motors leads to dramatic changes in the average processivity of the cargo. Increasing kinesin motors which moves in the positive direction of a microtubule track, keeping the number of dynein motors (which move in the negative direction) fixed, is expected to lead to enhanced transport in the plus direction. However, average processivity shows large negative direction movement which is a direct consequence of catch-bonded dynein.

In Chapter 5, we continue the study of bidirectional transport and quantify the motility states of the cargo. To do so, we solve the master equation for the time evolution of the probability of the cargo to be in a state specified by the number of attached kinesin and dyneins. The stationary state solution gives the probabilities. Maxima of the probability distributions give the motilty states of the cargo as plus directed motion, minus directed motion and pause states. We also identify combinations of these motility states and plot the phase diagrams for a set of parameter values like the stall force and strength of the catch bond.

In Chapter 6, we summarize.

Chapter 2

Morphological properties of a semiflexible filaments on a motor protein substrate

The cytoskeleton is made of semiflexible filaments like actins and microtubules and their associated motor proteins like myosin, dynein and kinesin [2, 43–49]. *In vitro* experiments, as we have discussed in Chapter 1 of this thesis, has provided a plethora of information regarding the workings of the individual cytoskeletal components as well as their collective dynamics [30, 36, 37, 50–55].In this chapter, we use theoretical modeling to analyze one such *in vitro* set up, the gliding assay, and look at the morphological properties of the cytoskeletal filament in the presence of motor proteins [1].

This led to observation of collective motion, e.g., formation of spiral and aster patterns in microtubules driven by kinesin [52] or dynein molecules [37], or swirling patterns in high density F-actins floating on a myosin motility assay [36]. Single molecule experiments on motor proteins revealed details of their dynamics, e.g., force-velocity relation, dependence of turnover on load experienced, and dependence of activity on ATP concentration [42,45,55,57–61]. Motion of rigid cargo under collective drive of molecular motors has been studied both experimentally and theoretically [62–70].

---

[1] The work discussed in this chapter is published in [56]

2.1 Theoretical models

The patterns observed in several of the experiments mentioned above, were explained within an active hydrodynamics framework, and agent based models [36, 37, 71, 72]. The active hydrodynamics framework describes such systems as active gels. The first step in writing down the theory is to identify the fluxes and forces. The fluxes correspond to the mechanical stress associated with the mechanical behavior of the cell, the time variation of the polar order and ATP consumption rate. The activity of the cytoskeleton is incorporated in the generalized force which is the chemical difference $\Delta\mu$ between the chemical potentials of ATP and the products of ATP hydrolysis. The conjugate force to the polarization changes is the local field which is obtained by the functional derivative of a free energy. This free energy is written down in the same vein as the polar liquid crystals. The hydrodynamics equations are then constructed following Martin, Parodi and Pershan including the symmetries and the activity. These equations depend on a set of phenomenological parameters, a number of which have already been introduced in describing liquid crystals and polymeric liquids. This active hydrodynamics approach has been used to varying degree of success in understanding organization of microtubules in the presence of molecular motors and motion of the cell lamellipodium.

Early theoretical approaches to explain experimental observations of spiral rotation or flagella like beating of a single F-actin filament in myosin gliding assay, modeled activity as a constant tangential force along the filament contour [51, 53]. Observations of emergent vortex structures in F-actin- myosin assay in Ref. [36] was explained using a hydrodynamic interaction, while the same in microtubule- dynein assay [37] was explained using polymer collision based arguments. Independent numerical simulations of self-propelled filaments are shown to spontaneously get into spiral rotation in presence and absence of hydrodynamic interaction [73–75]. Numerical simulations of active polymers composed of a permanent distribution of stresslets along its contour or chemically active / self propelled beads in the presence of hydrodynamics have shown similar results [76–79]. Generic consideration of a stiff filament in an active medium leads to the possibility of both increase or decrease of effective bending rigidity, depending on the orientation of filament segments with respect to contractile or extensile medium [80, 81]. The collective dynamics of such active self-propelled filaments has revealed activity driven crossovers from coherently free flowing filaments to frozen spiraling ones [82, 83]. Studies of semiflexible polymers under active correlated fluctuations showed a cross-over from bending rigidity dominated to flexible polymer- like dynamics [84].

2.2 Limitations of earlier studies

Previous studies either modeled the motor proteins explicitly considering the driven object as a rigid cargo, or modeled the mechanical properties of the driven polymer explicitly, using self propulsion devoid of any underlying mechanism for relaxation. Thus the impact of stress dependent dynamics of motor proteins on the filament properties, despite its importance, remains elusive within such models. In this chapter, we consider an explicit model of a cytoskeletal filament moving in two dimensions on a substrate decorated with motor proteins. This mimics the *in vitro* gliding assay set up. We study the morphological properties of the polymer by looking at the end-to-end distribution and tangent-tangent correlations. End-to-end distributions show dramatic changes as the local load dependence of the detachment rate and the active velocity is varied.

2.3 Model and Simulations

We consider an extensible semiflexible filament described as a bead-spring chain of N beads (identical and indistinguishable except for their positions) constituting $(N-1)$ bonds of equilibrium length σ such that the chain length $L = (N-1)\sigma$, spring constant A, and finite bending rigidity κ. The Hamiltonian given by Eq. 1.18 is discretized to give,

$$\beta H = \sum_{i=1}^{N-1} \frac{A}{2\sigma} \left[\mathbf{b}(i) - \sigma \mathbf{t}(i)\right]^2 + \sum_{i=1}^{N-2} \frac{\kappa}{2\sigma} \left[\mathbf{t}(i+1) - \mathbf{t}(i)\right]^2 , \tag{2.1}$$

with $\beta = 1/k_B T$, the inverse temperature. The bond vector $\mathbf{b}(i) = \mathbf{r}(i+1) - \mathbf{r}(i)$, where $\mathbf{r}(i)$ denotes the position of the i-th bead. This allows one to define the local tangent $\mathbf{t}(i) = [\mathbf{r}(i+1) - \mathbf{r}(i)]/b(i)$. In the limit of large A, instantaneous bond lengths $b(i) \approx \sigma$, and the polymer maps to a worm like chain [40]. In addition, excluded volume interactions between the non-bonded beads of the polymer is incorporated via a Weeks-Chandler-Anderson (WCA) potential

$$\beta V_{WCA}(r_{ij}) = \begin{cases} 4[(\sigma/r_{ij})^{12} - (\sigma/r_{ij})^{6} + 1/4] & \text{for } r_{ij} \le r_{cut} \\ 0 & \text{for } r_{ij} > r_{cut} \end{cases} \tag{2.2}$$

where r_{cut} is set at minimum of this potential which is at $2^{1/6}\sigma$.

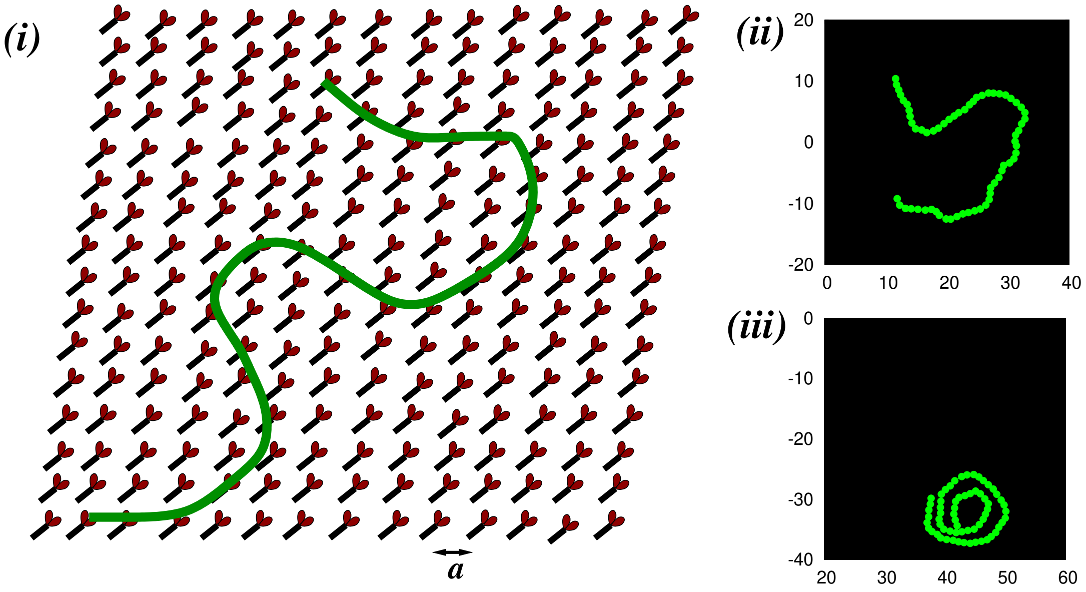

Figure 2.1: (color online)(i) Schematic of the system showing the molecular motors arranged on a square grid. The semiflexible polymer glides on the bed of molecular motors. (ii) and (iii) Simulation snapshots of the polymer in an open and spiral state for a polymer with persistence ratio $u = 3.33$, under the influence of MP activity $Pe = 100$, and bare processivity ratio $\Omega = 5/6$..

The polymer is placed on a substrate of motor protein (MP) assay. We explicitly model MPs and their dynamics, unlike several recent studies that used effective active polymer models [75, 84–86]. The MPs are modeled as *active* elastic linkers. The *tail* of i-th MP is attached irreversibly to the substrate at position $\mathbf{r}_0^i = (x_0^i, y_0^i)$, while the *head* is free to bind (unbind) to (from) the polymer. The attachment process is diffusion limited. The head of a MP attaches to a polymer segment if it lies within a capture radius r_c with an attachment rate $\omega_{\rm on}$. The extension $\Delta\mathbf{r}$ of the MP in the attached state generates an elastic load $\mathbf{f}_l = -k_m \Delta\mathbf{r}$. An attached MP unbinds from a polymer segment with a rate $\omega_{\rm off}$ which depends on the stress felt by the MP as

$$\omega_{\rm off} = \omega_0 \exp(f_l/f_d), \tag{2.3}$$

where ω_0 is the bare off rate, $f_l = |\mathbf{f}_l|$ and f_d is the detachment force. The ratio $\omega_{\rm on} : \omega_{\rm off}$ does not obey detailed balance. When attached, a MP can move on the filament towards one of its ends, depending on the MP and filament type. For example, attached Kinesin moves towards positive end of the microtubule with *active* velocity

v_t^a along the local tangent of the filament given by [42, 87]

$$v_t^a(f_t) = \frac{v_0}{1 + d_0 \exp(f_t/f_s)}, \tag{2.4}$$

where $f_t = -\mathbf{f}_l.\mathbf{t}$, $d_0 = 0.01$ and f_s is the stall force. Here v_0 denotes the velocity of MP in the absence of stress.

We perform numerical simulations of the model to investigate structural and dynamical properties of the polymer, actively driven by MPs. The molecular dynamics of polymer is performed using the velocity-Verlet algorithm in presence of a Langevin heat bath. The bath fixes the ambient temperature k_BT through a Gaussian white noise obeying

$$\langle \eta_i(t) \rangle = 0 \qquad \text{and} \qquad \langle \eta_i(t)\eta_j(t') \rangle = 2\alpha k_B T \delta_{ij} \delta(t - t') \tag{2.5}$$

where α denotes viscosity of the environment. The unit of energy is set by k_BT, length is set by σ and time by $\tau = \alpha\sigma^2/k_BT$. This defines a diffusion coefficient, $D = k_BT/\alpha$. In these reduced units we choose, $r_c = 0.5\,\sigma$, $f_s = 2\,k_BT/\sigma$, $f_d = f_s$, $A = 100\,\sigma^{-1}$, $k_m = A/\sigma$ and density of motor proteins in the 2d assay, $\rho = 3.8\,\sigma^{-2}$.

In absence of MPs, the polymer shows established equilibrium properties. The attachment (detachment) of MP heads are stochastic, and performed using probabilities $\omega_{\rm on}\,\delta t(\omega_{\rm off}\,\delta t)$. The extension in the attached state has two contributors – the MP head is dragged along with the filament segment to which it is attached, and it can slide from one segment to another with an active velocity v_t^a. We study the influence of the active bed of MPs on the static and dynamic properties of the polymer as we vary the

- bare processivity

$$\Omega = \frac{\omega_{\rm on}}{\omega_{\rm on} + \omega_0} \tag{2.6}$$

- a dimensionless Péclet number defined as

$$Pe = \frac{v_0 \sigma}{D}. \tag{2.7}$$

The numerical integrations are performed using $\delta t = 10^{-3}\tau$ for $Pe = 1$, and $\delta t = 10^{-4}\tau$ for $Pe = 10, 100$. We have checked that the fluctuations of the length of the semi flexible polymer are never more than 10-15 for the parameter ranges of the simulations.

2.4 Results

At equilibrium, mechanical and structural properties of a semiflexible filament are determined by the persistence ratio $u = L/l_p$, where L is the contour length of the chain, and l_p is the persistence length, which for a worm-like-chain (WLC) is related to bending rigidity κ by $l_p = 2\kappa/(d-1)$ [40].

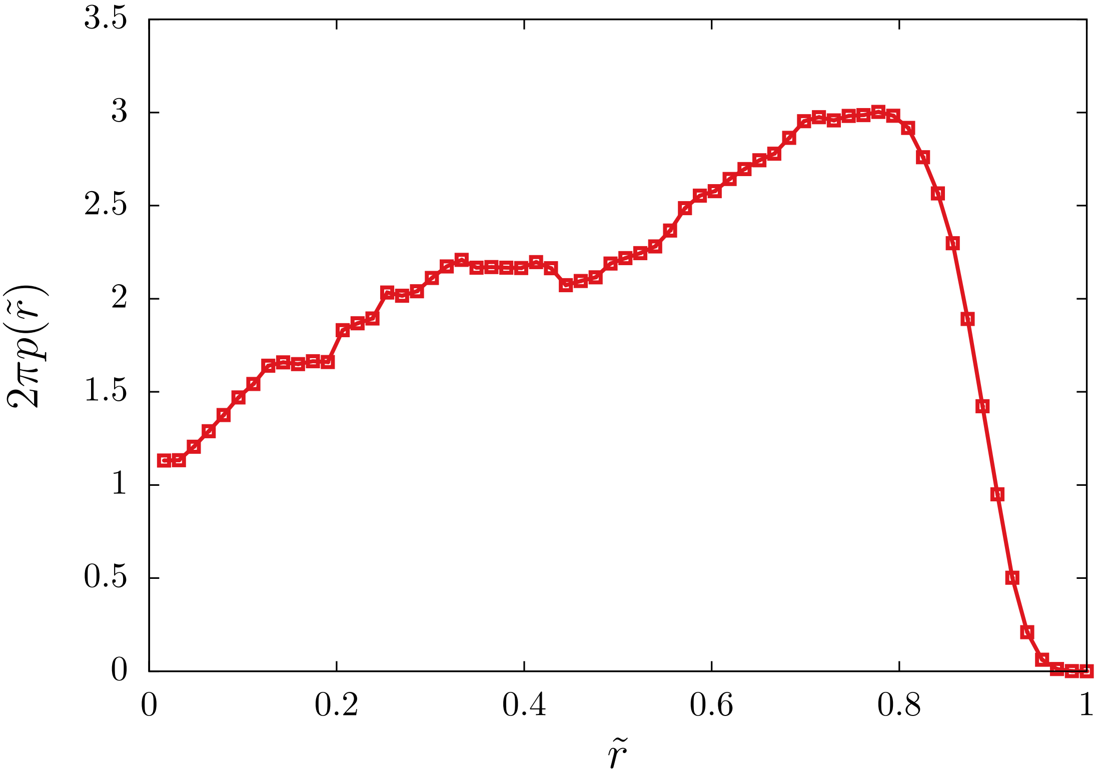

Figure 2.2: (color online) The end-to-end distribution of the semiflexible polymer at equilibrium $p_{eq}(\tilde{r})$ in the absence of motor proteins. Note that excluded volume interactions suppress the peak at $\tilde{r} = 0$.

The active drive from processive MPs attaching (detaching) to (from) the filament generates non-equilibrium stress which have profound effect on the steady state conformational properties of the polymer. To characterize the conformational properties, we obtain probability distribution of the end-to-end distance, $P(r, L)$, of the polymer. At equilibrium, this has the scaling form,

$$P(r, L) = \frac{1}{L^d} p(r/L, L/l_p) = \frac{1}{L^d} p(\tilde{r}, u)$$

where $\tilde{r} = r/L$ and $u = L/l_p$. The WLC limit of our polymer model is obtained in the limit of large bond-stiffness A. In equilibrium, $p(\tilde{r}, u)$ for WLC shows a first-order-like transition from a single maximum at $\tilde{r} = 0$ for the flexible limit of large u to a maximum at $\tilde{r} = 1$ for a very rigid polymer with small u [40, 88].

The transition point was determined to be near $u = 3.33$ where semiflexibility is most strongly pronounced in two and three dimensions. In all our simulations, unless stated otherwise, we use $\kappa = 9.45\,\sigma$ that corresponds to $u = 3.33$ for $L = 63\,\sigma$ chains. In presence of self-avoidance, the probability of end-to-end separation $p(\tilde{r}, u)$ at $\tilde{r} = 0$ gets suppressed (see Fig. 2.2). In *in vitro* experiments, the ratio u may be tuned by controlling persistence length of the chain by, e.g., changing salt concentration in the medium thereby changing interaction, or by stabilising the chain lengths. In all our simulations, unless stated otherwise, for $L = 63\,\sigma$ chains, $u = 3.33$ sets $l_p = 18.92\,\sigma$. Two configurations of the MP driven polymer is shown in Fig.2.1 for $Pe = 100$ and $\Omega = 5/6$.

2.4.1 Polymer morphology in the presence of motor proteins

In this section we talk about the activity dependence of end-to-end distribution functions and their difference from equilibrium for a filament with $N = 64$ having persistence ratio $u = 3.33$. The MP activity is controlled by turnover with a bare processivity $\Omega = 5/6$, and non-zero active velocity v_0 set by $Pe = 1$.

Under the active drive of the gliding assay of MPs, the morphology of the polymer changes. In Fig.2.3 and Fig.2.4 we show how this impacts the end-to-end distribution function $p(\tilde{r}, u)$. For comparison, the equilibrium distribution p_{eq} is shown in Fig.2.2. The conformational change with respect to the equilibrium is well captured by the logarithmic ratio,

$$\Delta\Sigma = \ln\left[\frac{p(\tilde{r})}{p_{eq}(\tilde{r})}\right]. \tag{2.8}$$

In Fig.2.3 we show how the dimensionless quantity $\Delta\Sigma$ changes with activity. If the activity of MPs is independent of the load force acting on them, $\omega_{\text{off}} = \omega_0$ and $v_t^a = v_0$. This corresponds to the limit of infinitely large f_d and f_s. It is expected that the deviation $\Delta\Sigma$ would be large for large non-equilibrium driving, quantified in terms of f_d, f_s and Ω. We first consider the situation in which $\omega_{\text{off}} = \omega_0$ is kept fixed so that $\Omega = 5/6$, and the active velocity v_t^a is varied (Fig.2.3) for three possible situations. (i) In the absence of any directed motion of the polymer, i.e., with $v_0 = 0$,

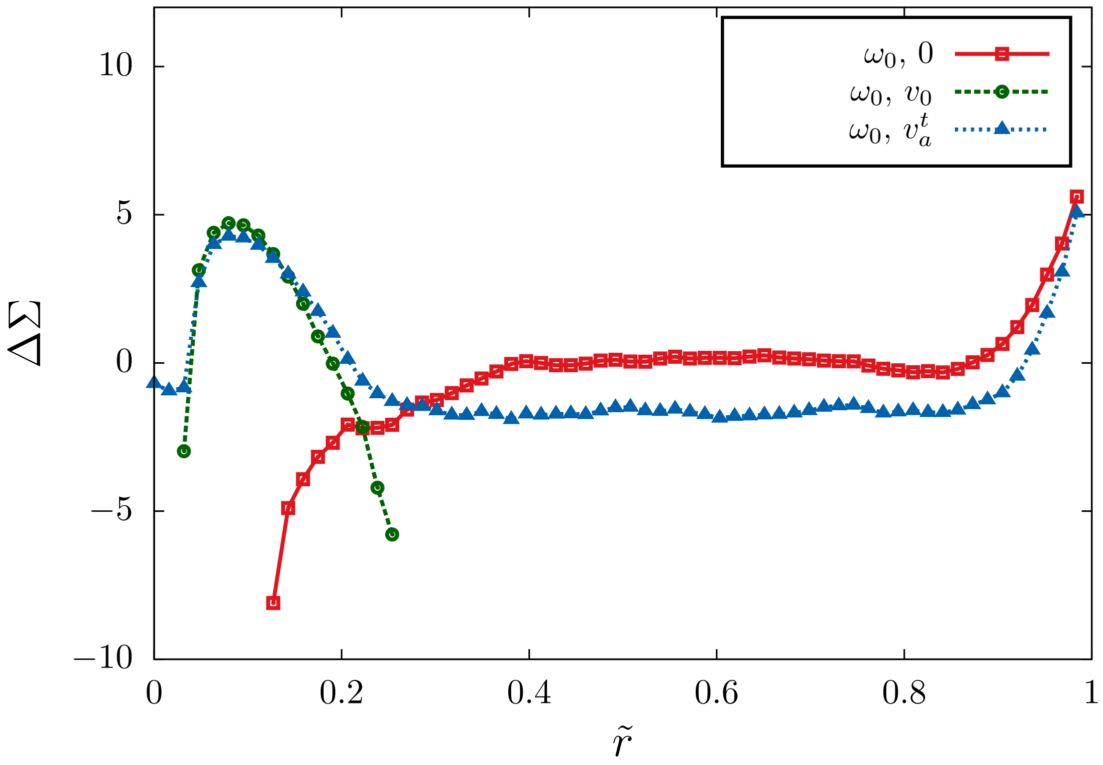

Figure 2.3: (color online) The logarithm of the ratio of the end-to-end probability distributions of the filament under active drive with respect to that of the equilibrium polymer, $\Delta\Sigma$, provides a measure of the difference in distributions. The legends denote parameter values (detachment rate, MP velocity), where, in this figure, all data sets correspond to a constant detachment rate ω_0, and MP velocity varies between constant values 0, v_0, and stretching dependent active velocity v_t^a as denoted by Eq.(2.4).

$\Delta\Sigma$ shows a dip near $\tilde{r} = 0$, indicating a relative bias to the *open* conformations of the polymer. This indicates that a mere stochastic attachment/detachment kinetics of MPs, that does not obey detailed balance, leads to an enhancement of effective stiffness of the filament. (*ii*) When attached, MPs move, and if the active velocity is assumed to be *independent* of the load experienced, we use $v_t^a = v_0$. The effect is dramatic. The filament, gliding on the attached MPs, undergoes a transition to a rotating spiral configuration (discussed further in Sec. 2.5.3). This gives rise to a peak in $\Delta\Sigma$ near $\tilde{r} = 0.1$. (*iii*) If we incorporate local stress dependence in v_t^a, the polymer is still softened but now switches between gliding and spiral states more freely. Thus in addition to the peak near $\tilde{r} = 0.1$, a non-zero value at higher $\tilde{r}$ appears in $\Delta\Sigma$. The statistics, dynamics and mechanical properties of the polymer under MP drive is determined by a competition between processive active velocity of MPs and bending

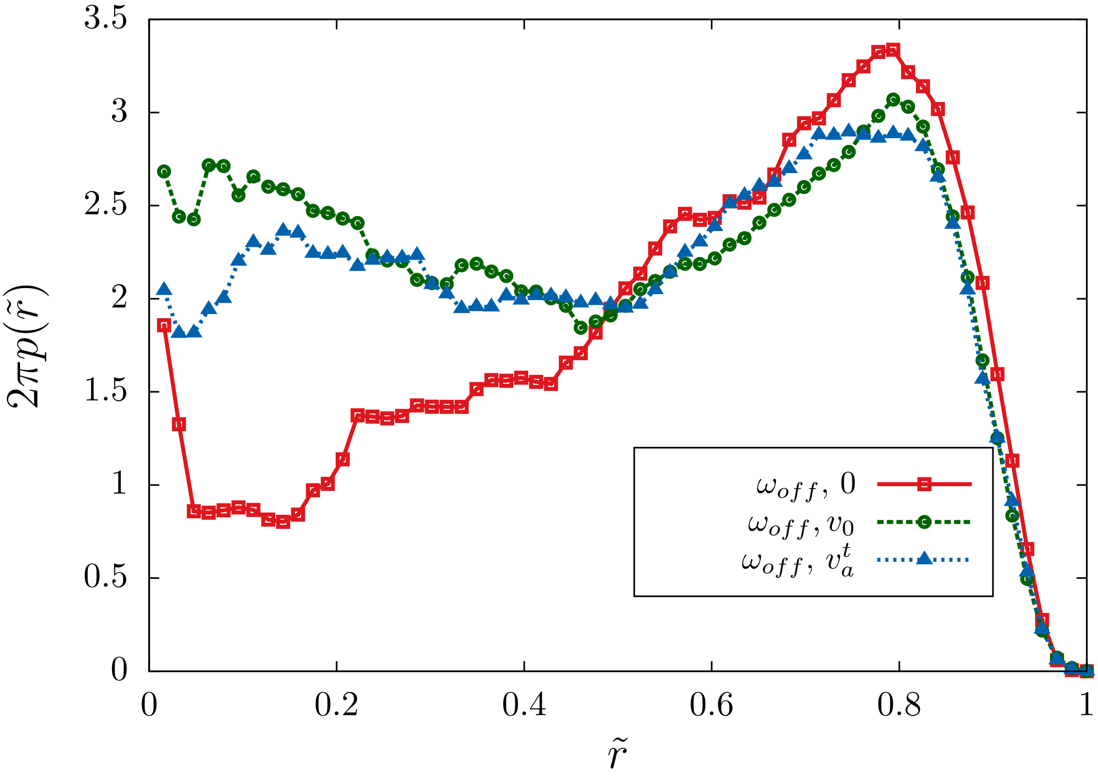

Figure 2.4: (color online)The end-to-end distribution of stretchable semiflexible polymer $p(\tilde{r})$, with local strain dependent detachment ω_{off} as in Eq.2.3. The variation of MP active velocities are as in Fig.2.3.

stiffness of the polymer.

We next consider the situation allowing the detachment rate ω_{off} to be *dependent* on the load force felt by individual MPs (Eq.2.3). In this case, the end-to-end distributions are very similar to the equilibrium distribution. Therefore, $\Delta\Sigma \approx 0$ (Fig.2.2) and the corresponding non-equilibrium end-to-end distributions are shown explicitly in Fig.2.4. Unlike the previous scenario where the unbinding rate was a constant, independent of the load force, here the non-equilibrium stress that is built up due to the attachment and subsequent directed walk of the motor proteins, is easily relaxed due to the load dependence of the unbinding rate. The stretched motor proteins enhances the unbinding rate, therefore allowing the polymer morphology to adopt equilibrium-like conformations. The distribution is closest to equilibrium when the attached motor proteins are static, i.e. $v_t^a = 0$. When velocity is switched on but is kept load independent so that the attached motor proteins are moving at a constant velocity on the filament, $v_t^a = v_0$, the end-to-end distribution shows the strongest non-equilibrium feature. At this point the distribution clearly shows a bi-modality with two maxima at $\tilde{r} \approx 0.1, 0.8$. When the active velocity is made load dependent as in Eq.2.4, the maximum at $\tilde{r} \approx 0.1$ shifts towards $\tilde{r} \approx 0$, as the polymer switches between gliding and spiral states more easily.

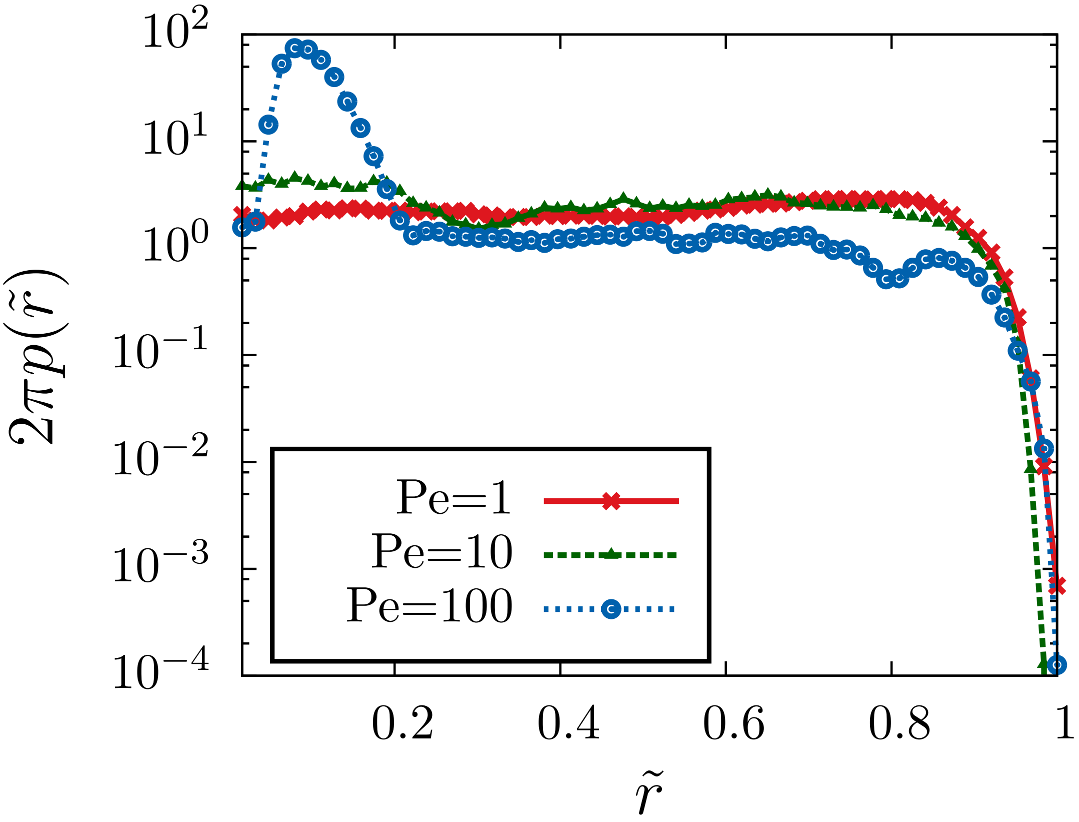

Figure 2.5: (color online) End-to-end distribution for three different values of Pe using stretching dependent turnover ω_{off} for $N = 64, \Omega = 5/6, u = 3.33$.

2.4.2 Dependence on Peclet number

In most biologically relevant situations, both the turnover and active motion of individual MPs depend on their instantaneous extension. The activity is most strongly reflected in terms of the bare velocity of MPs, v_0. As was shown in Ref. [42], this velocity of unloaded Kinesin MP increases from 1 nm/s to finally saturate to $\sim 1\,\mu$m/s, as the ambient ATP concentration increases from $1\,\mu$M to 1 mM. The change in v_0 is captured by changing Pe in our current setup. In Fig.2.5, we show how polymer properties vary with increasing Pe when both ω_{off} and v_a^t are treated as local strain dependent quantities. For low values of Pe, the local forces acting on the polymer backbone due to binding kinetics and motor movement is not sufficient to cause significant local curvature. As Pe is increased, due to tangential velocity of MPs and enhanced directional fluctuations, the polymer starts to coil up and rotates with a spiral configuration in the steady state (discussed further in Sec. 2.5.3). The impact shows up in terms of a maximum in $p(\tilde{r})$ near $\tilde{r} = 0.2$ appearing for large Peclet, $Pe = 100$ (Fig.2.5). As shown in the next section, this feature is robust with respect to change in Ω.

2.5 End-to-end distributions for different Ω

In Fig. 2.6, we show the dependence of the conformational properties of the polymer as the bare processivity $\Omega = \omega_{\text{on}}/(\omega_{\text{on}} + \omega_0)$ is varied. Here we consider the scenario where both the detachment rate and the active velocity depend on the local stress. For a fixed Ω we plot the end-to-end distribution of the polymer as Pe is changed. As in Fig. 2.6(c), the distributions look similar to equilibrium distribution $p(\tilde{r})$ for low Pe and a peak near $\tilde{r} \approx 0$ appears for high Pe, indicating the emergence of spiral states. Therefore we conclude that for stress dependent ω_{off}, varying Ω does not affect the conformational properties significantly. Recall that a stress independent ω_{off} with non-zero Pe results in coiled states of the polymer. Switching on local stress dependence in ω_{off} allows the polymer to relax back to its equilibrium conformations whenever stress builds up beyond a limit, even if the processivity Ω is high. As Pe is increased, it triggers an instability towards spiral states and we see the emergence of a peak near $\tilde{r} = 0$ in the steady state distributions.

2.5.1 Competition between activity and bending stiffness

For a semiflexible polymer in equilibrium, the end-to-end distribution $p(\tilde{r}, u)$ is determined by the dimensionless ratio $u = L/l_p$. On the other hand, in presence of motor proteins, the statistical and mechanical properties are expected to be determined by an interplay of activity and bending rigidity. To probe that within our model, here, we fix $\omega_{\text{off}} = \omega_0$, and vary the chain length $L = (N-1)\sigma$ by changing N, the ratio

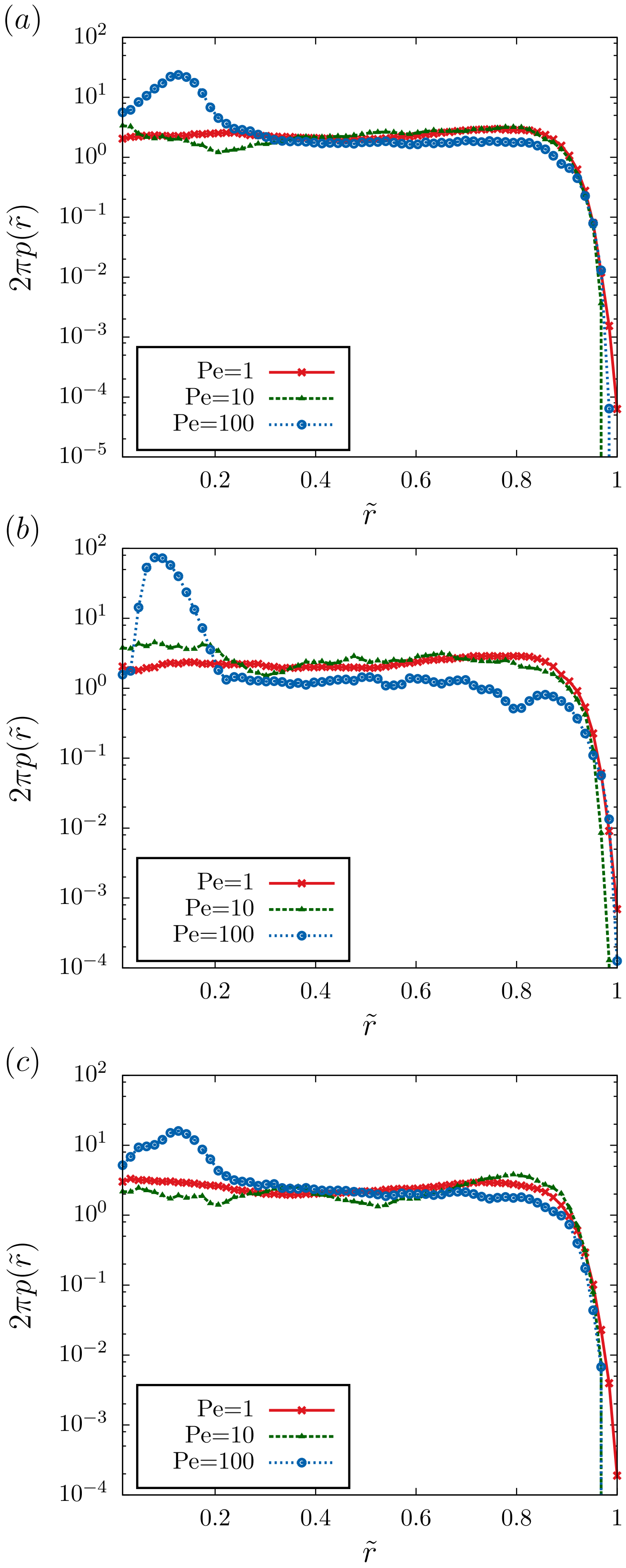

Figure 2.6: (color online) End-to-end distribution at $Pe = 1$, 10, 100 for different values of bare processivity Ω, using stress dependent active velocity and detachment rate with $N = 64, u = 3.33$. The graphs correspond to (a) $\Omega = 2/3$, (b) $\Omega = 5/6$, and (c) $\Omega = 20/21$.

$u = L/l_p$, and persistence length l_p of the polymer to study their impact on conformational properties. We use both stress dependent and independent v_a^t, and plot the end-to-end distributions for three different active velocities in Fig. 2.7. A comparison of Figs. 2.7(a) and (b) clearly shows that for the same u and different L, unlike in equilibrium semiflexible chains, the conformational properties of the polymer are significantly different. For example, for $N = 128$ and $u = 3.33$ (Fig. 2.7(b)), the distribution for $v_0 = 0$ indicates a much stiffer polymer compared to $N = 64$ (Fig. 2.7(a)).

For non-zero active velocity, the spiral states observed for $N = 64$ disappears for $N = 128$, leading to stiffer conformations devoid of spirals. If, however, we keep the value of l_p fixed as we change the length of the polymer from $N = 64$ to $N = 128$ (Fig. 2.7(c)), the distributions we get compares much better with Fig. 2.7(a). This suggests that, for a given processivity Ω, the conformational properties of polymers driven by MPs are determined by a competition between active velocity and bending rigidity, and not by the ratio u.

Within active polymer models with constant tangential drive, arguing that active force f_p may generate compression, a torque balance leads to a critical active force $f_p^c \sim l_p/L^3$, beyond which straight filaments are unstable towards buckling [89]. In the limit of stress independent activity, a simple extension of this relation to the instability of the filament under MP driving can be obtained by replacing $f_p^c = \alpha\Omega v_0^c$. This leads to a relation $v_0^c \sim l_p/\alpha\Omega L^3$. Thus buckling instabilities are expected to be controlled by the dimensionless number $\mathcal{F} = \alpha\Omega v_c L^3/l_p$. However, for polymers driven by real MPs that shows stress dependent activity and turnover, the determining factors turn out to be more subtle.

2.5.2 Determination of effective stiffness

To further characterize the steady state conformational properties of the polymer, we consider the tangent-tangent correlation function, $\langle \mathfrak{t}(s) \cdot \mathfrak{t}(s') \rangle$ for different Pe. For an equilibrium worm like chain, one expects a single exponential decay of the correlations, characterized by the persistence length l_p as, $\langle \mathfrak{t}(s) \cdot \mathfrak{t}(s') \rangle = \exp(-|s - s'|/l_p^{\text{eff}})$.

In the long separation limit, the presence of self-avoidance leads to an effective power law correlation function determined by the Flory exponent, a behavior we ignore for relatively short length scales in the ensuing discussion. This results in a l_p^{eff} that is larger than l_p in equilibrium simulations. The tangent-tangent correlation provides a measure for structural rigidity of the filament and can be determined from experiments by fluorescent imaging of polymer conformations.

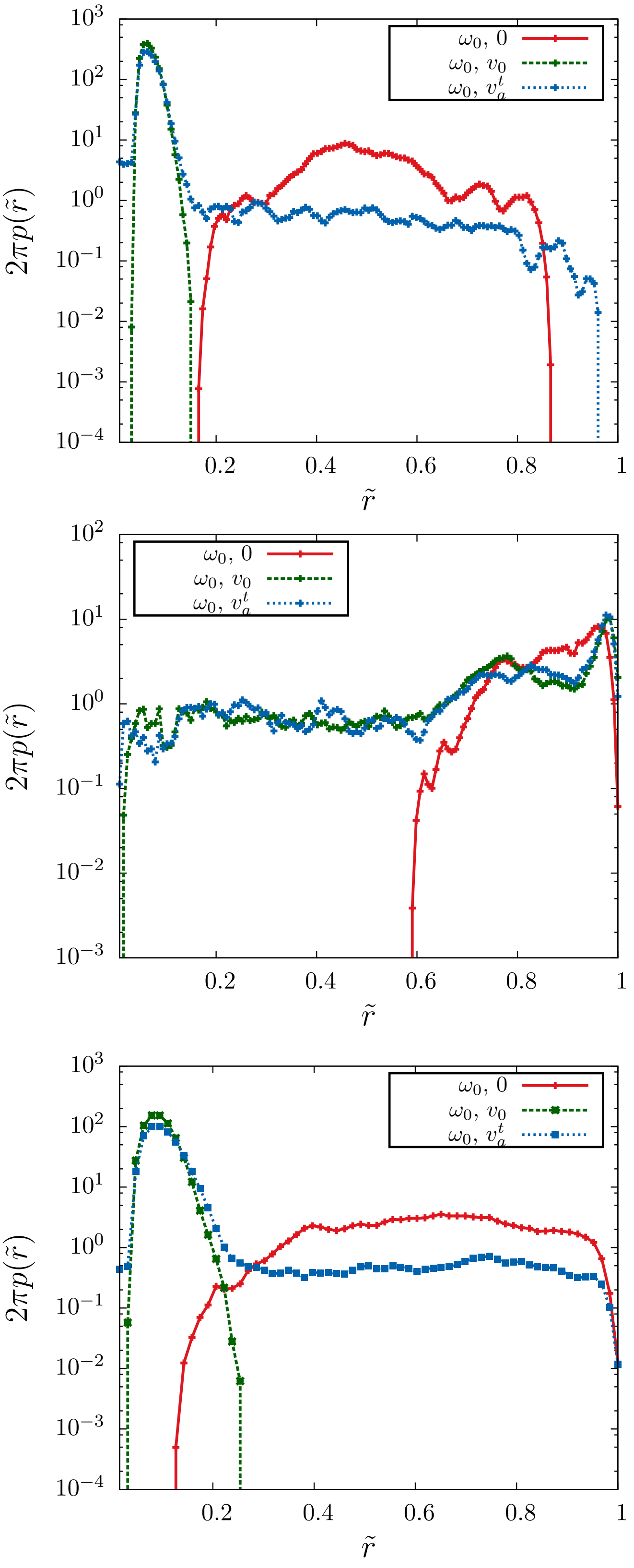

Figure 2.7: (color online) End-to-end distribution functions. We use constant detachment rate ω_0 with $\Omega = 5/6$ for all the figures. The variation of MP active velocities are as in Fig.2.3, with the non-zero active velocities set by $Pe = 1$. The three graphs show results for (a) $N = 64$, $u = 3.33$, $l_p = 18.92\,\sigma$. (b) $N = 128$, $u = 3.33$, $l_p = 38.14\,\sigma$ (c) $N = 128$, $u = 6.66$, $l_p = 18.92\,\sigma$.

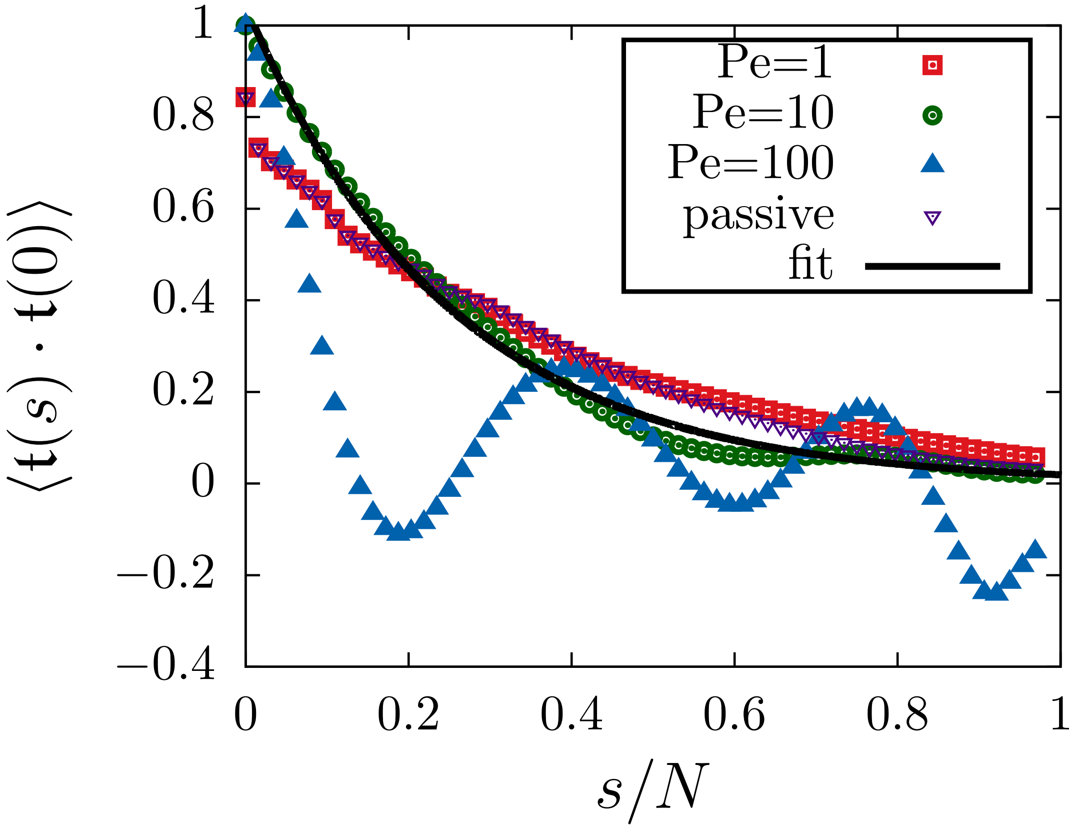

Figure 2.8: (color online) Tanget-tangent correlation function for a chain of $N = 64, u = 3.33$, and activity v_t^a set by $Pe = 1, 10$ and 100 and load dependent detachment rate ω_{off} with $\Omega = 5/6$. The data set *passive* denotes equilibrium result. The solid line shows a single exponential fit to $Pe = 10$ data used to extract the effective persistence length $l_p^{\text{eff}} = (15.99 \pm 0.24)\,\sigma$.

In Fig. 2.8, we observe that the correlation function for small activity, $Pe = 1$, shows a characteristic exponential decay that follows the equilibrium correlation function very closely. Fig. 2.8 shows that the correlation length decreases with increase in Pe. This is indicative of a softening of the polymer with the emergence of strong bending fluctuations. Up to $Pe = 10$ shown in the graph, the overall nature can be described by a single exponential decay, which is fitted to extract the effective persistence length l_p^{eff}, directly.

For higher values of Pe, e.g., at $Pe = 100$, the correlations start showing oscillations, capturing emergence of spiral conformations that occur at higher activity. In such cases, the crossing of zero by the correlation function is interpreted as the persistence length. The variation of this effective persistence length with activity is listed in Table 2.1.

Pe	$l_p^{\mathrm{eff}}/\sigma$
equilibrium	23.59 ± 0.39
1	25.21 ± 0.23
10	15.99 ± 0.24
100	8.89

Table 2.1: Activity modulated effective persistence length of a chain of length $L = 63\,\sigma$ (with $N = 64$) and $l_p = 18.92\,\sigma$. The table shows l_p^{eff} obtained from tangent-tangent correlation function. With Pe, the persistence length first increases, and then decreases.

2.5.3 Coexistence of spiral and open chains

In order to quantify the observations of the different conformational states of the polymer, we use the turning number [90], $\psi(s) = (1/2\pi)\int_0^s ds'\,(\partial\vartheta/\partial s')$ where $\vartheta(s)$ is the angle subtended by the unit tangent $\hat{t}(s)$ with x-axis. This $\psi(s)$ is a good order parameter, clearly distinguishing an open polymer from a spiral one and also separates clockwise and anticlockwise spiral states (Fig. 2.9). The steady state probability distribution of $\psi(s = L)$ is a Gaussian with a peak at $\psi(L) = 0$ for small Pe, indicating the absence of spiral states. Increasing Pe has a dramatic effect on the distribution, with symmetric peaks emerging for non-zero $\psi(L)$ indicative of coexisting spiral states with equal probabilities of clockwise and anticlockwise winding, along with the open state characterized by $\psi(L) = 0$ (Fig. 2.10) . Such phase coexistence is a characteristic feature of a non-equilibrium first order phase transition.

Similar coexistence of spiral and open conformations were observed earlier in an active polymer model characterized by constant tangential force [75]. It was not *a priori* clear that our current model would give rise to a similar conformational behavior, given that the activity in our model gets modified by the build up and release of local strain via load dependent activity and turnover. As we have already shown, in fact, the effect of local strain dependence reflects strongly in the end-to-end distribution functions $p(\tilde{r})$. Further, as we show in the following section, this implies dynamical crossovers in mean squared displacement that are unlike the active polymer model.

2.6 Conclusions

Using stochastic molecular dynamics simulations we have investigated the conformational properties of a semiflexible polymer in the presence of motor proteins, which (un)bind (from) to the polymer and perform directed active motion. Unlike in the

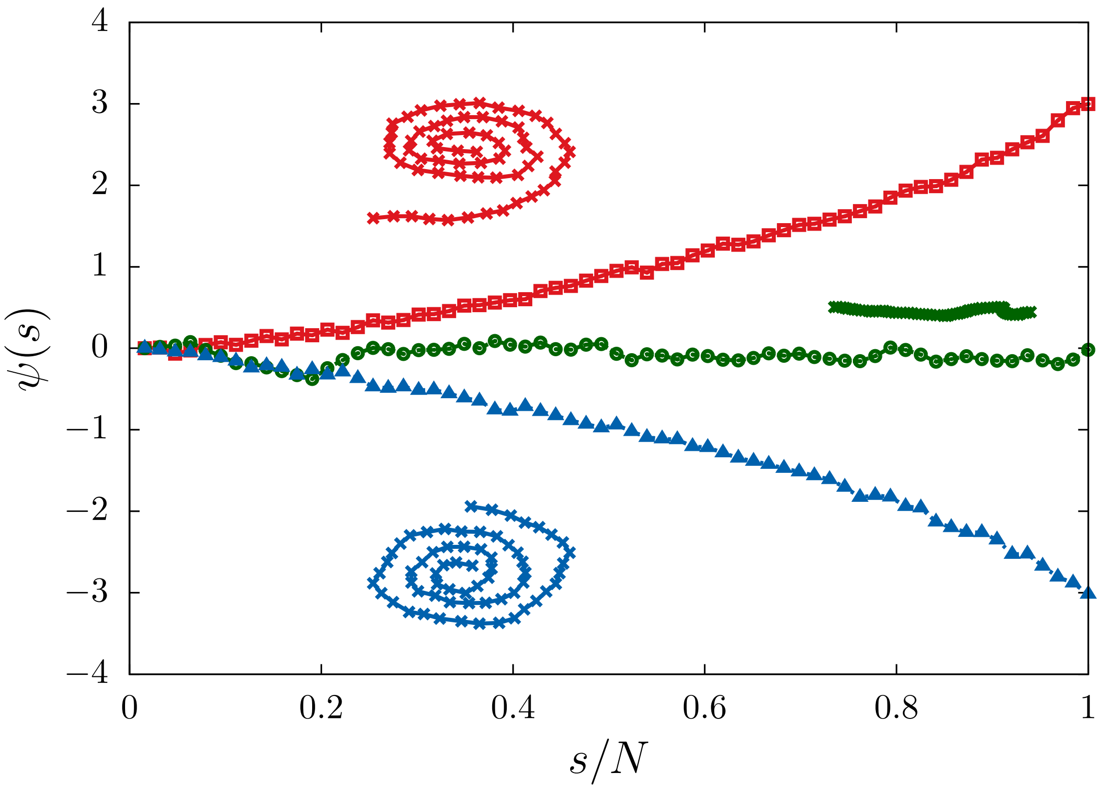

Figure 2.9: (color online) Plot of turning number $\psi(s)$ for three different configurations with $Pe = 100$. It shows that $\psi(s)$ is an effective order parameter, distinguishing between the open state (green), clockwise spiral (blue) and anti-clockwise spiral (red). For $N = 64, u = 3.33$ and load dependent detachment ω_{off} with $\Omega = 5/6$ with activity v_t^a set by Pe.

equilibrium worm like chain, the end-to-end statistics in this case is not controlled by the ratio of persistence length and chain length, but results from a local competition between the processive active velocity and bending rigidity. As is shown in this chapter, local stress dependence of turnover and active velocity provides new relaxation mechanisms giving rise to steady states unlike the active polymer models with constant tangential self-propulsion. The activity influences polymer morphology, and mechanical properties in a concerted manner. With increasing activity of the motor proteins, we observed that the end-to-end distribution characterising polymer conformation shows both stiffening and softening relative to the equilibrium morphology associated with the build up of local active stress and its relaxation.

While our system reproduces some of the predictions of the standard active polymer model, some other properties that we observe are entirely due to the strain dependence of the activity and turnover of MPs. For example, the observed activity dependent reduction of effective bending stiffness, and the coexistence of spiral and

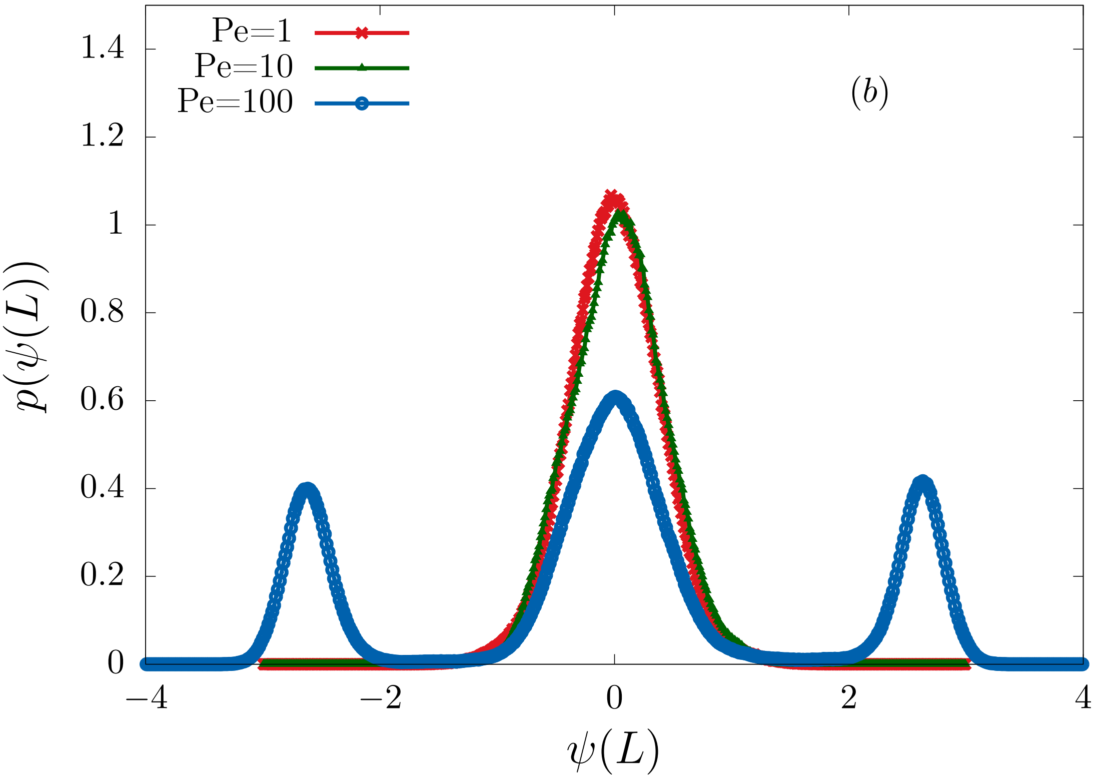

Figure 2.10: (color online) Probability distributions for $\psi(L)$ using $N = 64, u = 3.33$ and load dependent detachment ω_{off} with $\Omega = 5/6$ at $Pe = 1, 10$ and 100.

open conformations at an activity beyond a critical value are expected within the active polymer model. On the other hand, the detailed nature of end-to-end distribution functions, and the series of ballistic-diffusive crossovers observed in the center of mass dynamics are features that are unlike active polymer models [75].

Chapter 3

Dynamical properties of a semiflexible filament driven by molecular motors

In this chapter, we continue the discussion on semiflexible filament properties on a motor protein substrate with a focus on the dynamics of the filament. Earlier active polymer models, which model activity as a self-propulsion force acting tangentially on the monomers of the polymer, have showed a single crossover from a short time ballistic, to long time diffusive behavior of the center of mass of the polymer [75, 86]. In contrast, as we show in this paper, the more microscopic consideration of both the cytoskeletal filament and motor proteins which we described in detail in Chapter 2, leads to a series of ballistic-diffusive crossovers of the filament center of mass.[1].

3.1 Anomalous dynamics of the center of mass

In Fig. 3.1 we show mean squared displacement (MSD) of the polymer center of mass as a function of time, for three different Pe values that are separated over two decades. At very short time scales the MSD shows an approximate *ballistic* scaling $\langle \Delta r_{cm}^2 \rangle \sim t^2$ up to $t \approx 1$ at all Pe. With increasing time, five crossovers at $Pe = 1$ can be clearly seen, these include three ballistic-diffusive crossovers and two diffusive-ballistic crossovers. At $Pe = 10$, numerical integration required a smaller step size restricting the results to a shorter total time t. Otherwise, all the crossovers are retained at $Pe = 10$, with a reduction in crossover times. The qualitative behavior changes as the activity is increased to a larger value, $Pe = 100$. At this regime the first

---

[1] The work discussed in this chapter is published in [56]

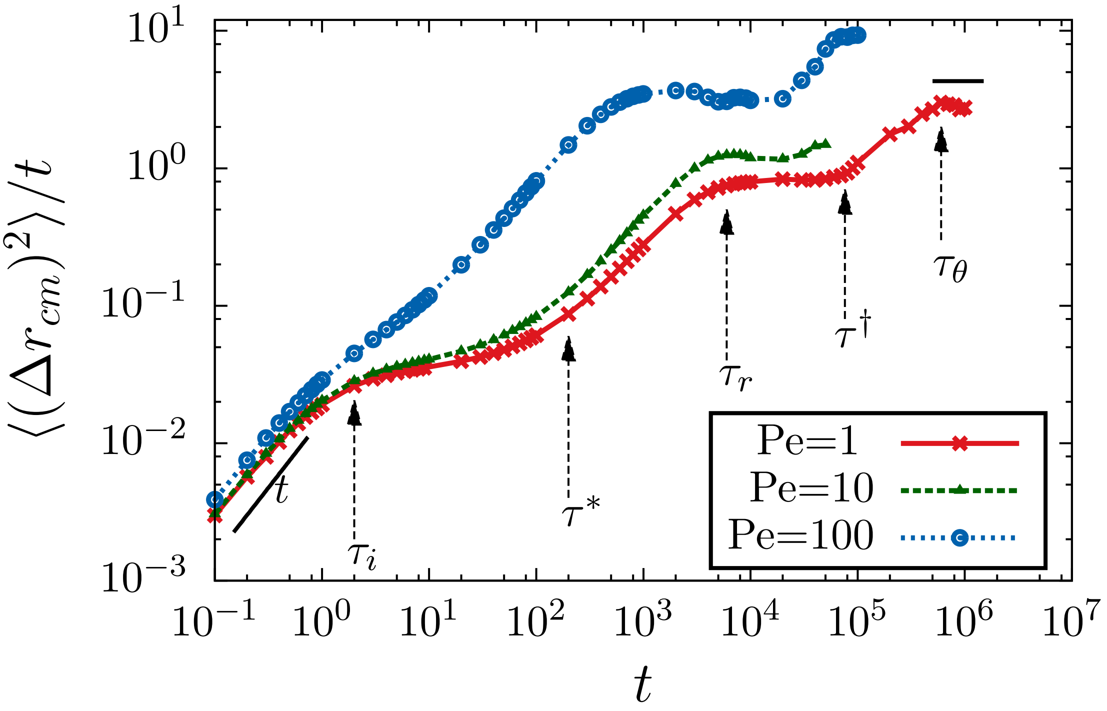

Figure 3.1: (color online) Dynamics of center of mass for a chain of $N = 64, u = 3.33$, with load dependent MP activity v_t^a controlled by Pe and detachment rate ω_{off} determined by $\Omega = 20/21$. Mean squared displacement of the center of mass at different Péclet ($Pe = 1, 10, 100$).

ballistic-diffusive crossover almost vanishes. At $t \approx 1$ one finds a barely discernible change in the slope which quickly gets back to ballistic scaling. This is due to an effective merger of the first diffusive-ballistic crossover to the first ballistic-diffusive one. The ballistic-diffusive crossovers discussed in this section is a recurring feature of active systems [75, 86, 91, 92]. It is known that a persistent random walker undergoes a crossover from initial ballistic to a final diffusive motion, while directed random walkers show a crossover from short time diffusive to long time ballistic scaling [91]. In the following section we present a detailed explanation of the crossovers observed.

In Fig. 3.2, we show time evolution of the center of mass position of the polymer at $Pe = 100$, indicating its various conformations associated with the trajectory. As the polymer takes a folded conformation, which is often a spiral in our system, the force generated in different segments by the gliding assay cancel each other, and the net directed force on the center of mass is negligible. As a result, the center of mass moves diffusively, getting mostly localized in a narrow region, albeit with an enhanced diffusivity. When the polymer retains a more open conformation, the gliding assay indeed generates directed force on the center of mass, leading to a ballistic motion

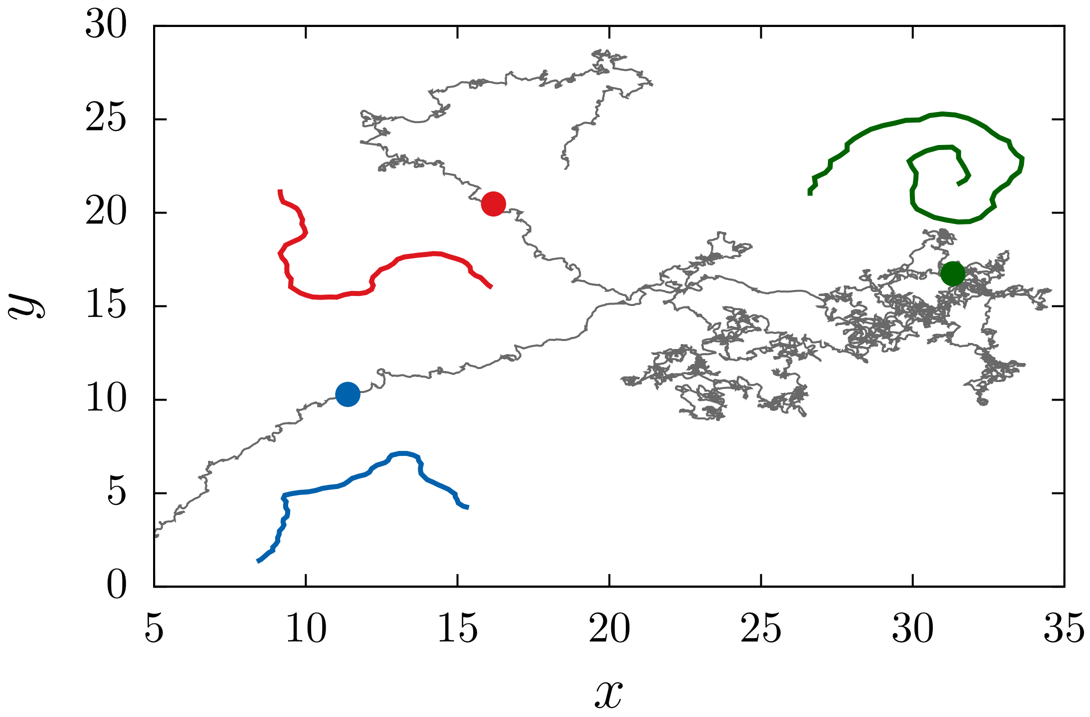

Figure 3.2: (color online) Dynamics of center of mass for a chain of $N = 64, u = 3.33$, with load dependent MP activity v_t^a controlled by Pe and detachment rate ω_{off} determined by $\Omega = 20/21$. (Numerical analysis of the dynamics at $Pe = 100$ is presented. The gray line shows a center of mass trajectory. Structure of polymer corresponding to the blue, red, and green points indicated on the trajectory are shown in the respective colors.

over such periods shown by long directed trails.

More quantitatively, the ballistic- diffusive crossovers are associated with changes in the evolution of the end-to-end extension r_{ee}, the orientation of the end-to-end vector ϕ, and the root mean squared (RMS) fluctuation of the center of mass position $\sqrt{\Delta r_{cm}^2}$ along a single trajectory. In Fig. 3.3 we show this at $Pe = 100$. Clearly there are time-spans over which r_{ee} remains close to zero, i.e., the polymer remains in a folded (spiral at $Pe = 100$) state, e.g., between $t \approx 4.5 - 5 \times 10^5\,\tau$. It should be noted that the formation of spiral happens at high Pe as was shown in Sec. 2.5.3. However, even at smaller Pe, the chain switches between open and non-spiral folded conformations. Non-spiral folds show a little higher value of r_{ee} than when spirals form. There are other time windows over which r_{ee} fluctuates rapidly between open and spiral states (e.g., between $t \approx 0 - 4 \times 10^5\,\tau$).

As is shown in Fig. 3.3, ϕ changes ballistically on a timespan over which r_{ee} remains close to zero in a spiral state. In particular, between $t = t_1$ and t_2 the spiral rotates *clockwise* ballistically reflected in a linear change in ϕ with a negative

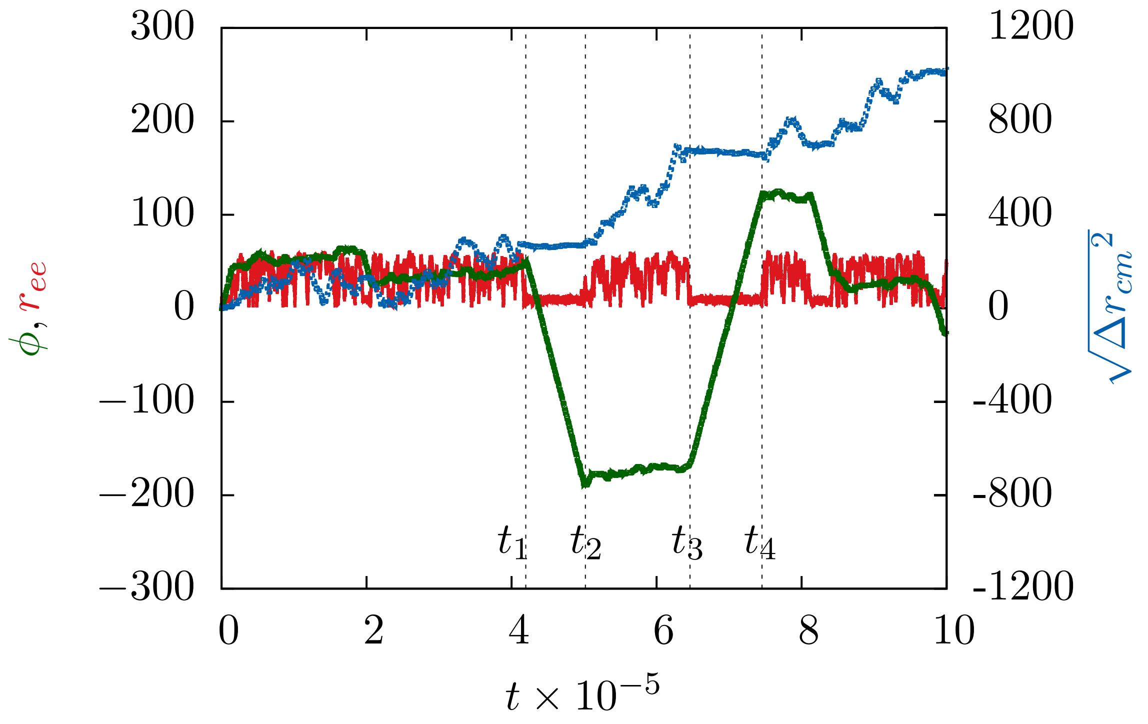

Figure 3.3: (color online) Dynamics of center of mass for a chain of $N = 64, u = 3.33$, with load dependent MP activity v_t^a controlled by Pe and detachment rate $\omega_{\rm off}$ determined by $\Omega = 20/21$. Numerical analysis of the dynamics at $Pe = 100$ is presented. The end-to-end length r_{ee} (red line), end-to-end orientation ϕ (green line), and root mean squared fluctuations of the center of mass position (blue line) for a single trajectory are shown as a function of time at $Pe = 100$.

slope. During such time spans, the r_{ee} of spirally folded polymer remains small, and the center of mass position of the polymer does not change appreciably, as is shown by the flat segment of $\sqrt{\Delta r_{cm}^2}$ in Fig. 3.3 in this time-window. In the window of $t = t_2$ and t_3 the filament opens up switching between relatively close and open conformations stochastically captured by the strong fluctuations in r_{ee}. In such a state the directed rotation practically stops, captured by the flat, approximately parallel to t-axis portion of the $\phi(t)$ curve. The polymer encounters directed drive from MPs during the time-spans over which it opens up leading to appreciable displacement $\sqrt{\Delta r_{cm}^2}$ of the centre of mass. Between $t = t_3$ and t_4, the polymer folds back into a spiral state again, and starts rotating in the *anti-clockwise* direction this time, captured by the linear increase in ϕ, associated with characteristic flat segments of r_{ee} and $\sqrt{\Delta r_{cm}^2}$.

3.2 Can an effective polymer model describe the dynamics?

The polymer under gliding assay, switching between attached and detached states, can be represented by an effective active polymer model [93], provided the attachment-detachment rates $\omega_{\rm on}$, $\omega_{\rm off}(=\omega_0)$ and active velocity $v_a = v_0$ of MPs in the attached state are assumed to be independent of the MP stretching. As we have shown, in the large activity limit the effective bending rigidity gets strongly compromised. Thus ignoring bending stiffness contribution, one may write the dynamics of polymer segments $\mathbf{r}(s)$ as

$$\gamma \frac{\partial \mathbf{r}}{\partial t} = A\frac{\partial^2 \mathbf{r}}{\partial s^2} + f_p \frac{\partial \mathbf{r}}{\partial s} + \eta_a(t), \tag{3.1}$$

where $f_p = \gamma v_0 \Omega$ with processivity $\Omega = \omega_{\rm on}/(\omega_0 + \omega_{\rm on})$. The active noise due to (de)attachment has mean $\langle \eta_a \rangle = 0$ and correlation

$$\langle \eta_a(s,t)\eta_a(0,0)\rangle = D_a \exp(-t/\tau)\, L\delta(s) \tag{3.2}$$

with noise strength $D_a = f_p^2(\omega_{\rm off}/\omega_{\rm on})$ and turnover time-scale $\tau = (\omega_{\rm on}+\omega_{\rm off})^{-1}$. Note that in the effective dynamics, both the mean active force and strength of active noise depend on active velocity v_0 of MPs, whereas the correlation time in active noise is given by the effective turnover rate.

Analysis of the Eq. 3.1 in presence of f_p is not straight-forward, as the mean force acts along the local tangent that itself evolves with time. Decoupling the mean active force, and correlated random noise, as was often done in earlier publications, simplifies the analysis [84,86]. This provides some useful insight into the dynamical cross-overs. Using $f_p = 0$ along with a non-zero D_a allows one to expand solutions of Eq.(3.1) into a complete set of eigen functions $\phi_n(s) = \sqrt{2/L}\cos(n\pi s/L)$ corresponding to the eigenvalue equation $A d^2\phi_n/ds^2 = -\epsilon_n \phi_n$, with eigen values $\epsilon_n = A(n\pi/L)^2$, and orthonormality condition

$$\int_0^L ds\, \phi_n(s)\phi_m(s) = \delta_{nm}. \tag{3.3}$$

The expansions

$$\mathbf{r}(s,t) = \sum_{n=0}^{\infty} \phi_n(s)\mathbf{r}_n(t), \qquad \vec{\eta}(s,t) = \sum_{n=0}^{\infty} \phi_n(s)\vec{\eta}_n(t), \tag{3.4}$$

lead to a simple relation for the center of mass position $\mathbf{r}_c(t) = \mathbf{r}_{n=0}(t)/\sqrt{2L}$. The correlation between modes $\langle \eta_m(t)\eta_n(0)\rangle = LD_a e^{-t/\tau}\delta_{m,n}$, along with the solution

$$\mathbf{r}_n(t) = \frac{1}{\gamma}\int_{-\infty}^{t} dt' e^{-(t-t')/\tau_n} \vec{\eta}_n(t'), \tag{3.5}$$

gives $(\mathbf{r}_0(t) - \mathbf{r}_0(0)\,) = (1/\gamma)\int_0^t dt'\vec{\eta}_0(t')$ as $\tau_0^{-1} = 0$. Finally one gets,

$$\langle[\mathbf{r}_0(t) - \mathbf{r}_0(0)]^2\rangle = \frac{2D_a L}{\gamma^2}\,\left[t + \tau(e^{-t/\tau} - 1)\,\right]. \tag{3.6}$$

As it is clear, in the short time limit $t \ll \tau$ this predicts a ballistic behavior $\langle[\mathbf{r}_c(t) - \mathbf{r}_c(0)]^2\rangle \approx (D_a L/\gamma^2\tau)\,t^2$, whereas in the long time limit $t \gg \tau$ that crosses over to normal diffusion, $\langle[\mathbf{r}_c(t) - \mathbf{r}_c(0)]^2\rangle \approx (2D_a L/\gamma^2)\,t$ [86].

It is easy to show that in the presence of a thermal noise with $\langle\eta_{th}(s,t)\eta_{th}(0,0)\rangle = 2D_{th}\delta(t)\,L\delta(s)$, fluctuations $\langle[\mathbf{r}_0(t) - \mathbf{r}_0(0)]^2\rangle = 2LD_{th}t\,/\,\gamma^2$. As a result, the full expression for displacement fluctuations is

$$\langle[\mathbf{r}_c(t) - \mathbf{r}_c(0)]^2\rangle = \frac{2D_{th}L}{\gamma^2}\,t + \frac{2D_a L}{\gamma^2}\,\left[t + \tau(e^{-t/\tau} - 1)\,\right]. \tag{3.7}$$

Thus at short time, $t \ll \tau$, the overlap of ballistic and diffusive behavior $\langle[\mathbf{r}_c(t) - \mathbf{r}_c(0)]^2\rangle = (2D_{th}L/\gamma^2)\,t + (D_a L/\gamma^2\tau)\,t^2$ predicts an overall super-diffusive dynamics, which crosses over to diffusive scaling with an enhanced diffusion constant $2L(D_{th} + D_a)/\gamma^2$ at longer time $t \gg \tau$. This explains a single crossover from super-diffusion to diffusion with increase in time. However the multiple crossovers that we see in our work cannot be explained within this picture. A more quantitative theoretical analysis will require solution of the effective Langevin equation incorporating the presence of f_p and bending rigidity explicitly. In what follows, we attempt to give an understanding of these multiple crossovers using three relaxation time scales.

3.3 Ballistic to diffusive cross overs

To analyze the crossovers of the centre of mass MSD, let us first consider the dynamics of a particle in a Langevin heat bath in absence of any active drive, $m\,dv/dt = -\alpha v + \eta(t)$ where the Gaussian random noise obeys $\langle\eta(t)\rangle = 0$ and $\langle\eta(t)\eta(0)\rangle = 2\alpha k_B T\delta(t)$. The corresponding displacement fluctuation of passive origin is given by

$$\langle\Delta r_p^2(t)\rangle = 6\frac{k_B T}{m}\tau_I^2\left[\frac{t}{\tau_I} - 1 + e^{-t/\tau_I}\right], \tag{3.8}$$

where $\tau_I = m/\alpha$. For time scales $t \ll \tau_I$ this leads to a ballistic scaling of MSD, $\langle \Delta r_p^2(t) \rangle \approx 3v_{eq}t^2$, with a velocity $v_{eq} = (2k_BT/m)^{1/2}$. At longer times $t \gtrsim \tau_I$, this crosses over to a diffusive scaling $\langle \Delta r_p^2(t) \rangle = 6D_{eq}t$ with $D_{eq} = k_BT/\alpha$. As is shown in Fig.3.1, the polymer centre of mass shows such a crossover near $\tau_I = 1$ in our simulations [1]. Because of the molecular motor drive, further ballistic-diffusive crossovers beyond t_I are observed. Following Ref. [91], we identify two possible mechanisms related to activity, (i) the persistence of the direction of centre of mass velocity described by the correlation time τ_θ, and (ii) the correlated fluctuations of the speed of the centre of mass with correlation time τ_s.

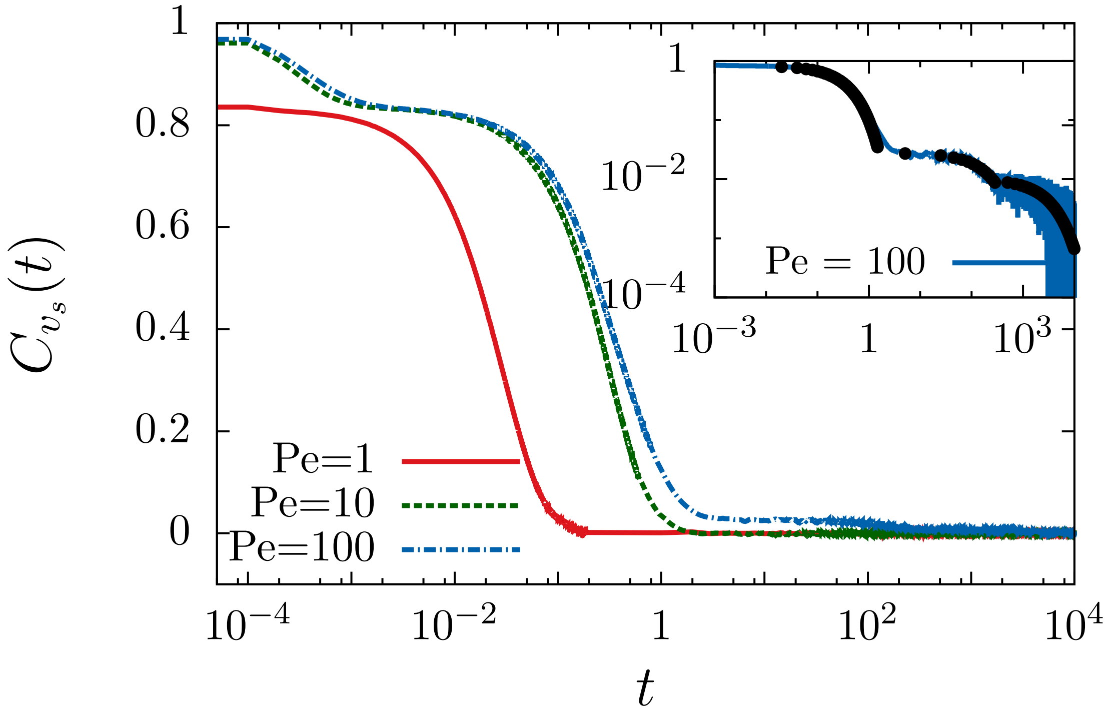

Figure 3.4: (color online) Speed autocorrelation of the centre of mass of the polymer. Single exponential decays are observed for both $Pe = 1$, 10, with correlation times $t_s \approx 0.1\tau$, 1.0τ respectively. (Inset) In the log-log plot, for $Pe = 100$, multiple exponential decays with $t_s \approx 1\tau$, 250τ, 2000τ are shown. The three exponential fits are indicated by black points.

We analyse autocorrelation of the centre of mass velocity vector, focussing on the speed $v_s(t)$, and orientation $\theta(t)$ separately. Here we distinguish between the direct measures of the correlation times t_s and t_θ associated with multi-exponential decays of correlations, from the assumptions of single exponential decays with τ_s, τ_θ used in the analysis of dynamical cross-overs in Sec. 3.3. In Fig. 3.4 we show the auto-correlation of speed, $C_{v_s}(t) = \langle \delta v_s(t) \delta v_s(0) \rangle / \langle \delta v_s^2 \rangle$. A fast single exponential decay $\exp(-t/t_s)$ is observed at both $Pe = 1$, 10, with $t_s \approx 0.1\tau, 1.0\tau$, respectively. However, at $Pe = 100$, we observe multiple exponential decays with time scales $t_s \approx 1\tau$, 250τ, 3600τ (see the inset of Fig. 3.4).

---

[1] Given that both mass and viscous friction scales similarly with the chain length, $\tau_I = 1$.

The orientational correlation $C_\theta(t) = \langle e^{i[\theta(t)-\theta(0)]} \rangle$, shows multiple exponential decays at all Pe values (Fig. 3.5). The initial decay is fast with $t_\theta \approx 1\tau$. For $Pe = 1, 10$ we can extract the longer time scales, as shown in the log-log plot in the inset for $Pe = 1$, to give $t_\theta = 1500\tau, 2000\tau$ respectively. However, for $Pe = 100$, in the absence of better averaging, it is difficult to extract the longest time scale.

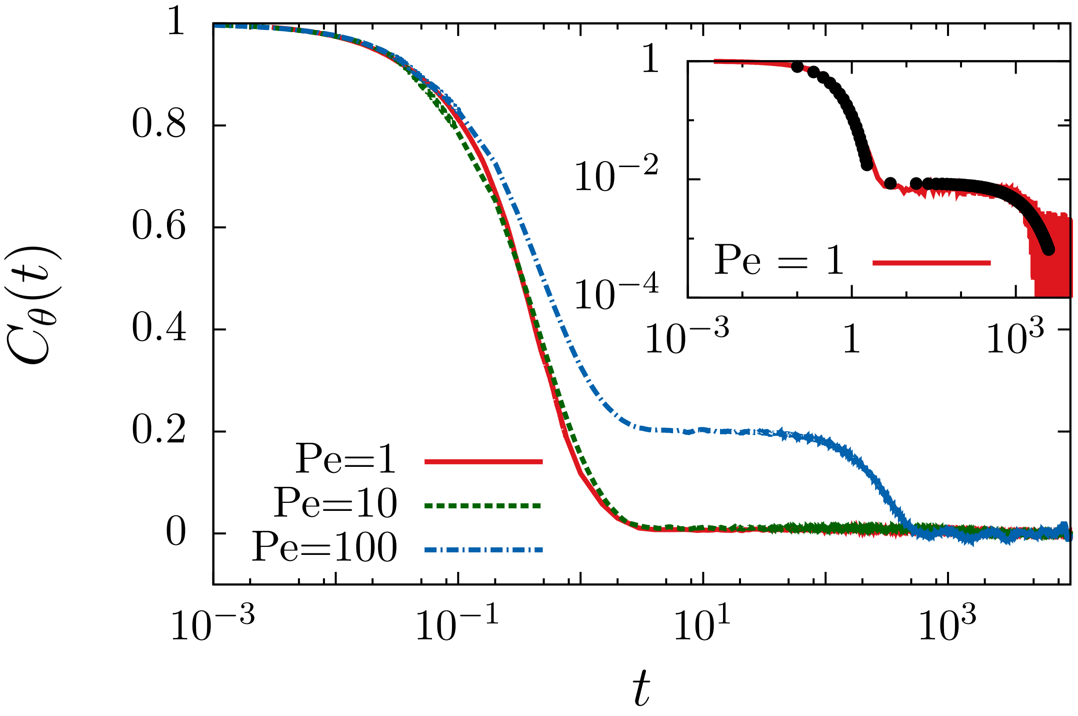

Figure 3.5: (color online) Orientational autocorrelation of the centre of mass velocity vector. This shows multiple exponential decays for all Pe. (Inset) For $Pe = 1$, the log-log plot shows multiple exponential decays with time scales $t_\theta \approx 1\tau$, 1500τ. The two exponential fits are indicated by black points.

Moreover, the speed and orientations remain correlated. The cross-correlation functions $C_{v_s,\theta}(t) = \langle v_s(t)\theta(0) \rangle / [\sqrt{\langle \delta v_s^2 \rangle} \sqrt{\langle \delta \theta^2 \rangle}]$ calculated for $Pe = 1$, 10, 100 are shown in Fig. 3.6. All of them show significant correlation, which remarkably do not decay with increasing time-gap. The asymmetry of the data around $t = 0$ captures the break-down of time-reversal symmetry due to the non-equilibrium molecular motor drive.

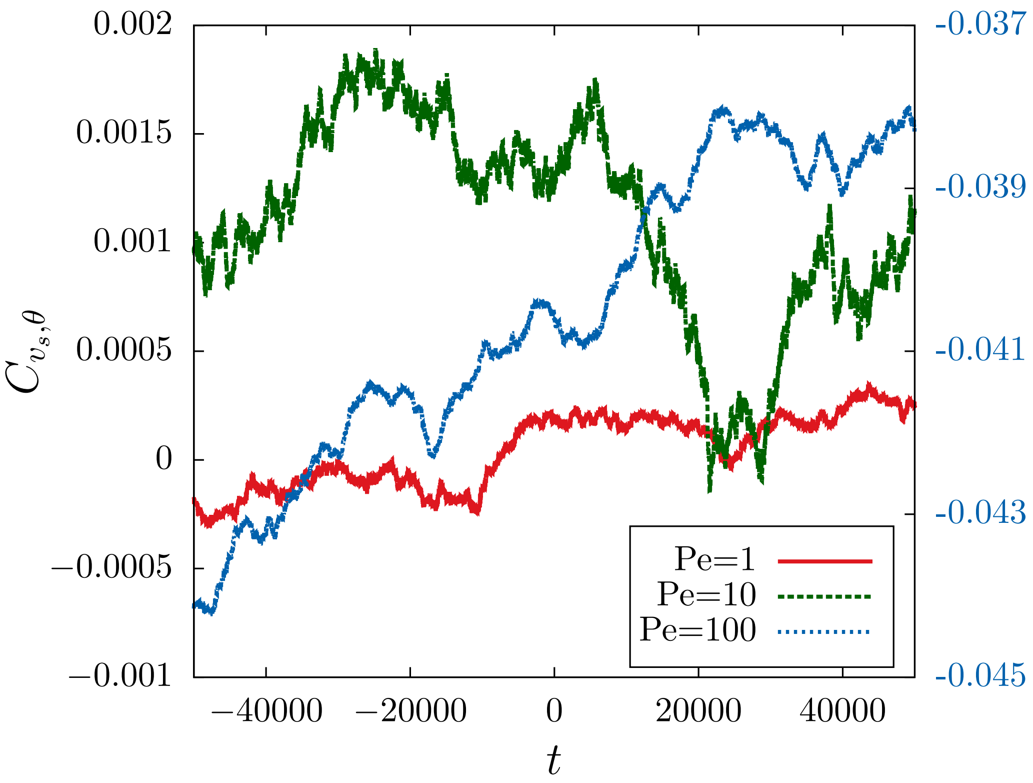

Figure 3.6: (color online) Cross-correlation of the orientation and speed of the centre of mass velocity for $Pe = 1$ (red), 10 (green) and 100 (blue, and values correspond to right ordinate).

Such correlations can be ignored to use the expression of active displacement fluctuations,

$$\begin{aligned}\langle \Delta r^2(t)\rangle &= \langle \Delta r_p^2(t)\rangle + 2\langle v_s\rangle^2 \tau_\theta^2 \left(\frac{t}{\tau_\theta} - 1 + e^{-t/\tau_\theta}\right) \\ &\quad + 2\langle \delta v_s^2\rangle \tau_r^2 \left[\frac{t}{\tau_r} - 1 + e^{-t/\tau_r}\right], \end{aligned} \tag{3.9}$$

where, $\tau_r^{-1} = \tau_\theta^{-1} + \tau_s^{-1}$. In the above expression the speed $\langle v_s\rangle$ and its fluctuations $\langle v_s^2\rangle$ are due to activity controlled by Pe. If $\langle \delta v_s^2\rangle = 0$, the above expression would suggest a ballistic dynamics for $t \ll \tau_\theta$, crossing over to diffusion at $t \gtrsim \tau_\theta$ as the direction of persistent motion diffuses. This is expected for structureless active Brownian particles with constant active speed.

However, in presence of speed fluctuations in the polymer, the other time-scale $\tau_r < \tau_\theta$ intervenes. The total mean squared displacement of the polymer center of mass has contributions from both thermal fluctuations Eq.(3.8) and activity Eq.(3.9).

If the three time-scales $\tau_I \ll \tau_r \ll \tau_\theta$ present in the problem are well separated, they are expected to lead to three ballistic-diffusive crossovers: (a) At $t \ll \tau_I$ one expects a ballistic motion $\langle \Delta r_{cm}^2 \rangle \approx 3v_{eq}t^2$ with a velocity $v_{eq} = (2k_BT/m)^{1/2}$. (b) At $t \gtrsim \tau_I$ one crossover to diffusive regime takes place, with equilibrium diffusion constant $D_{\mathrm{eq}} = k_BT/\alpha$. This is the first ballistic-diffusive crossover, and is independent of activity. (c) This regime lasts until $\tau^* = 3(v_{eq}^2/\langle \delta v_s^2 \rangle)\tau_I$ at which the chain starts to respond to the active force that drives it in a directed manner. This gives rise to the first diffusive-ballistic crossover. For $\tau^* < t \ll \tau_r$, we find a ballistic behavior dictated by the active speed fluctuation $\sim \langle \delta v_s^2 \rangle t^2$. A sufficiently strong activity can enhance $\langle \delta v_s^2 \rangle$ to reduce τ^* to merge this active ballistic regime to the equilibrium ballistic scaling, as is seen for $Pe = 100$ in our simulations. (d) As t crosses τ_r, the scaling of $\langle \Delta r^2(t) \rangle$ crosses over to another diffusive regime, the second ballistic-diffsuive crossover, with effective diffusion constant $D \approx D_{\mathrm{eq}} + \dfrac{1}{3}\langle \delta v_s^2 \rangle \tau_r$. (e) This regime persists until $\tau^\dagger = 3(v_{eq}^2/\langle v_s \rangle^2)\tau_I + 2(\langle \delta v_s^2 \rangle/\langle v_s^2 \rangle)\tau_r$. Beyond this point the second diffusive-ballistic crossover takes place. For $\tau^\dagger < t \ll \tau_\theta$, the ballistic behavior is dictated by $\sim \langle v_s \rangle^2 t^2$. (f) For $t \gtrsim \tau_\theta$, this ballistic regime slowly crosses over to the final diffusive behavior, the third ballistic-diffusive crossover, dictated by an effective diffusion constant $D \approx D_{\mathrm{eq}} + \dfrac{1}{3}(\langle \delta v_s^2 \rangle \tau_r + \langle v_s \rangle^2 \tau_\theta)$. This qualitatively explains the ballistic-diffusive crossovers obtained in Fig.3.1.

Before ending this section, we note that, the fluctuations in active speed and orientation in the polymer arise essentially from the same driving mechanism due to molecular motors, and conformational relaxation of the polymer. Thus the two quantities may have similar fluctuations and significant cross-correlation.

3.4 Conclusions

While our system reproduces some of the predictions of the standard active polymer model, some other properties that we observe are entirely due to the strain dependence of the activity and turnover of MPs. For example, some of our results, e.g., the transitions between open and spiral states, reproduce behavior already observed in tangentially propelled polymers. However, a priori it is not clear that to what extent a polymer driven by a molecular motor bed would behave similar to such active polymer models. For example, within our model the amplitude and orientation of active drive due to molecular motors felt by each monomer is subject to the local stress felt, and is not constant unlike the tangentially propelled polymers. On the other hand, the detailed nature of end-to-end distribution functions, and the series of ballistic-diffusive crossovers observed in the center of mass dynamics are features that are unlike active polymer models [75]. We have shown, these crossovers can be explained using three fundamental relaxation time scales, the inertial time τ_i, the correlation time of active speed τ_s, and correlation time of orientations of active drive τ_θ. Each of these quantities show multiple exponential relaxation, from which we separately determine the corresponding time scales. Although, our explanation of multiple crossovers assumes single exponential decay of correlations, the real dynamics turn out to be more complex, as is evident from their multiple relaxation times. Within a given time-window of mean squared displacement, the longest relaxation times corresponding to the speed and orientation may dominate the observed dynamical behavior.

Chapter 4

Dynein catch bond as a mediator of codependent bidirectional cellular transport

Molecular motors such as kinesin, myosin and dynein generate forces to drive the transport of vesicles and cargo, cytokinesis, cellular motility and a number of cellular processes [1,94]. A plethora of *in-vitro* studies on single motor proteins have revealed fascinating details about their structure, function and the forces exerted by them in carrying out these cellular processes. However, motor proteins *in-vivo* are known to work together in large numbers and their emergent collective behavior is far from properly understood [17,68,95–98].

The force generation of single motor proteins is of the order of a few piconewtons. Several such proteins acting together could generate large forces. Experiments have revealed that this teamwork between motor proteins is also different for different classes of these proteins [94]. For example, dynein is known to work better in a team than kinesin, generating larger forces to perform several key cellular processes such as retrograde transport, separation of chromosomes, etc. Apart from generating large forces, this teamwork of several motor proteins also leads to large distance transport of cargo. Kinesin and dynein motors are known to be primarily responsible for these transport processes. How these motors act in tandem to facilitate effecient transport is an important question and has been hotly debated. Experiments have suggested that the cooperative action of several such motor proteins help to distribute the load therefore enabling transport over large distances. The difficulty in performing controlled *in-vivo* experiments to look at motor protein functionality inside cells has made theoretical modelling a useful tool to understand these processes.

Bidirectional transport is ubiquitous in nature in the context of intracellular transport [94, 99–101]. Within the cell, oppositely directed motor proteins such as dynein and kinesin motors walk on microtubule (MT) filaments [94, 102] to transport diverse cellular cargo [94]. A theoretical framework proposed to explain the bidirectional transport is based on the *tug-of war* hypothesis [94, 97, 98, 100, 102–105], which posits that the motors stochastically binds to and unbinds from the filament while mechanically interacting with each other through the cargo that they carry (Fig. 4.3) [98, 103, 104]. The resultant motion arises due to the competition between the oppositely directed motors [103, 104].

The *tug-of-war* model predicts that inhibiting the activity of one motor species would lead to an enhancement of motility in the other direction. While many experiments have provided support for this mechanical tug-of-war picture [96, 102, 103, 106, 107], there remain a large class of experiments which are incompatible with the predictions of this model and show that there exists some coordination mechanism due to which inhibition of one motor species results in an overall decline in the motility of the cargo [98, 99, 108–111]. This apparently counterintuitive finding has been referred to as the *paradox of codependence* [94, 98]. The resolution of this paradox in terms of the underlying mechanisms which govern bidirectional transport remains an important open question.

Recently it has been demonstrated experimentally that dynein motors work together to generate large forces which increases linearly with the number of such motors bound to the cargo [17, 112]. Moreover the size of a step that each dynein takes during its motion is dependent on the load, leading to clustering of dyneins. Curiously, as force is increased, dyneins show “catch bond” like behavior, the detachment rate of dynein decreasing with increasing force [113]. Catch bond behavior [114–116] have been observed in several biological protein receptor-ligand complexes, particularly important being the case of cell adhesion complexes [117, 118], actin/myosin complex [119, 120] and microtubule-kinetochore attachments [121]. *In vitro* experiments on dynein have shown that the detachment rate of a dynein motor initially increases with increasing force, with a peak aroung 2 pN before showing the characteristic catch-bond behavior at higher forces [113]. This suggests a very interesting slip-catch-slip transition which demands a thorugh study.

In our thesis so far, we have looked at the role of motor proteins in governing the morphology and dynamics of a single filament in an *in vitro* gliding assay set up. However, to understand the role of the specific nature of dynein detachment characteristics, we turn our attention to a bead assay set up where the geometry is inverted : motor proteins have their tail domains attached to a cargo while their head domains can attach/detach to/from a cytoskeletal filament fixed on the substrate. When attached to the filament, the head domains walk along the filament leading to cargo transport. Within this set up, we ask the following question : how does catch bonding in dynein influence the transport properties of a cargo which is capable of bidirectional transport on a microtubule filament due to oppositely directed motor proteins such as dynein and kinesin motors?[1]

4.1 Modelling dynein catch bond.

Cytoskeletal motors carrying cargo undergo attachment (detachment) to (from) the associated cytoskeletal filament during long range transport. The detachment of a motor protein under a constant load force F is modelled as a barrier crossing problem, where the rupture of the bond between the motor and the cytoskeletal filament is explained as an escape over a transition state barrier brought about by thermal activation. Defining a force scale $F_d = k_BT/l$, where k_BT is the thermal energy and l is the length scale which characterizes the binding-unbinding transition, we can write the dissociation rate of a single motor protein as $\varepsilon = \varepsilon_0 \exp(F/F_d)$, where ε_0 is the dissociation rate in the absence of force. This implies that the dissociation rate increases with increasing load, a result remniscent of a "slip" bond. The behavior of catch bonds however are known to be completely different. The detachment rate for catch bond decreases as we increase the force and at large enough forces it increases, exhibiting a minima at intermediate forces. There is therefore a "catch-slip" transition at a critical force. Different mechanisms have been proposed for the catch bond such as the two-state two-pathway model [123, 124], the one-state two-pathway model [125–127] and the bond deformation model [126]. We discuss two models for the detachment rate which has proven successful in explaining a catch-slip transition.

Two pathway model. This model considers two paths to the detachment process - the catch pathway which opposes the load and the slip pathway which favors it. The detachment rate under the constant force F is then given by

$$\varepsilon(F) = \varepsilon_0^s \exp\left(\frac{F}{F_d^s}\right) + \varepsilon_0^c \exp\left(-\frac{F}{F_d^c}\right) \tag{4.1}$$

---

[1] The work discussed in this chapter is accepted in Phys. Rev. Research. The arxiv version is [122]

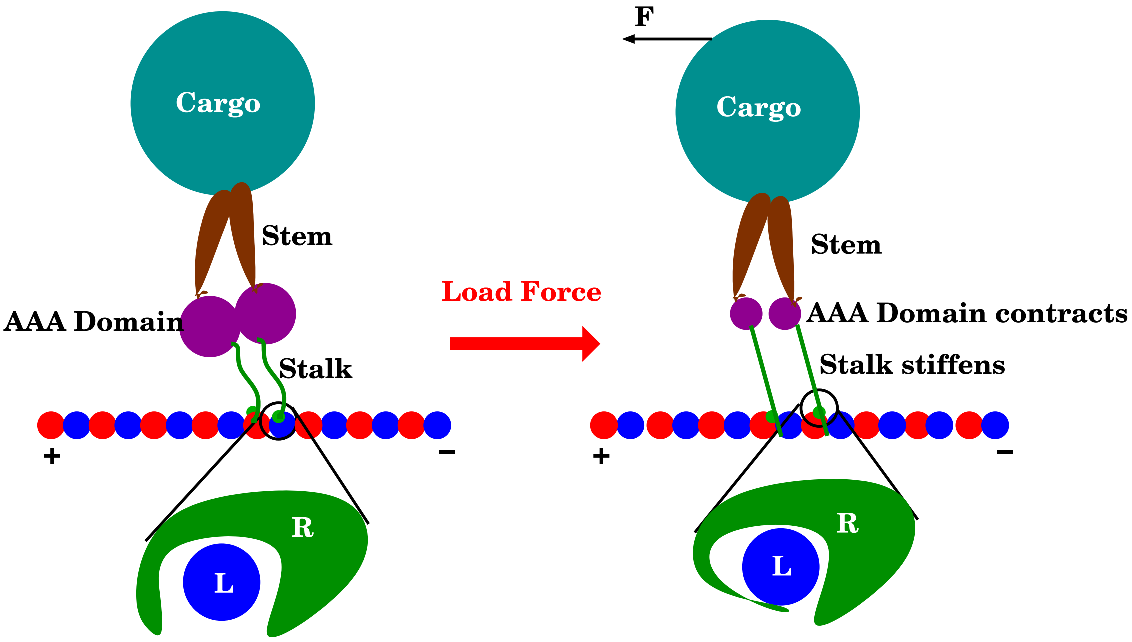

Figure 4.1: (Color online) Here we show the schematics of a dynein motor walking on a microtubule filament. Catch bond behavior is anticipated to be happening due to a conformational change at the microtubule binding domain of the stalk of the dynein motor. Adapted from [70]

where $\varepsilon_0^s, \varepsilon_0^c$ are the dissociation rates in the absence of force for the slip and catch pathways respectively and F_d^s, F_d^c are the corresponding force scales. Note that to get catch bond behavior we require $\varepsilon_0^c \gg \varepsilon_0^s$. If the catch barrier is initially lower than the slip barrier, the system demonstrates a catch-slip transition with increasing force.

Deformation model. The deformation model, on the other hand, proposes that force alters the conformation space in a fashion that strengthens receptor-ligand binding, and hence decreases the detachment rate. If the minimum of the potential decreases faster with force than the height of the barrier, one again obtains a catch-slip behaviour [126]. The deformation energy is given by, $E_d(F) = \alpha[1 - \exp(-\frac{F}{F_0})]$, where α characterizes the strength of the deformation energy and F_0 sets a force scale.

Cytoplasmic dynein has two heads and they perform processive movement on the microtubule track (see Fig. 4.1). The head of the dynein motor has a globular region constisting of six AAA domains. This globular region is thought to contract under a load force which leads to an extension of the stalk which is attached to the niicrotubule [17, 128, 129]. Now the region where the stalk binds to the microtubule has a receptor-ligand binding. Beyond a certain critical load force, allosteric deformations can lead to a locking of the receptor-ligand domain giving rise to a catch bond (Fig. 4.1). At intermediate or low loads, the force is not strong enough for the allosteric deformation to occur and the motor moves via the usual differential stepping mechanism [17].

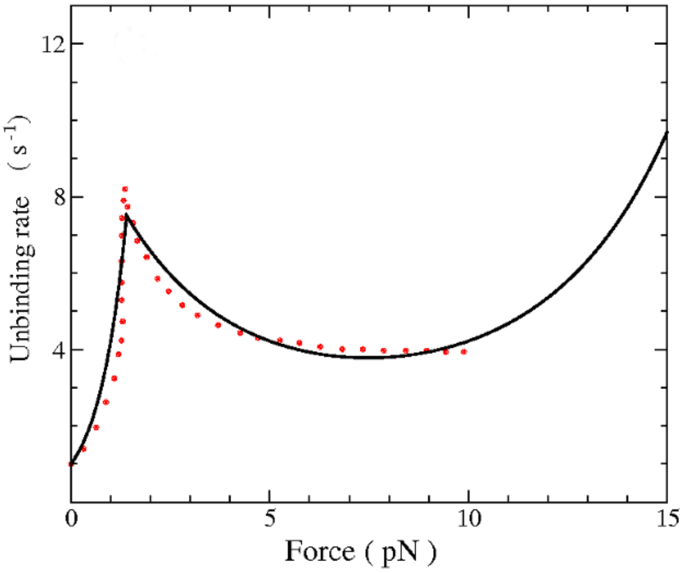

Figure 4.2: Single dynein unbinding rate from experiments [113] (points) and the corresponding fit (solid line) from the TFBD model [130].

As discussed earlier, experimental evidences on dynein detachment kinetics reveal that the rate initially increases with force up to a stall force, $F_s = 2$pN, which is defined as the load force at which the cargo stalls. Beyond F_s, dynein exhibits catchbonding characterized by a decrease in detachment rate with increasing opposing load (see Fig. 4.2). At large enough times, the rate of detachment increases again as expected. This slip-catch-slip behavior is incorporated in our work by a threshold force bond deformation model with the deformation energy now given by

$$E_d(F) = \Theta(F - F_s)\alpha \left[1 - \exp\left(-\frac{F - F_s}{F_0}\right)\right], \tag{4.2}$$

and the unbinding rate of the cargo carried with n attached motors attached to filaments is

$$\varepsilon(F) = \varepsilon_0 \exp\left[-E_d(F) + F/F_d\right] \tag{4.3}$$

where the second term represents the usual slip contribution which exponentially grows with applied load. This TFBD Model exhibits a *slip-catch-slip* behavior for a single motor unbinding rate as a function of applied force on the motor (see Fig. 4.2).

Using this TFBD model for dynein motors, it was earlier shown that in the context of unidirectional transport of cargo by a team of only dynein motors, catch bonding gives rise to dramatic results which are in sharp contrast to transport by cargo by a team of kinesin motors with slip bond detachment kinetics [70]. Due to the non-monotonic nature of the catch bond, the average velocity of the cargo was predicted to increase with increasing load force. Phase diagrams in experimentally accessible regimes were also obtained in this study.

4.2 Theory and Simulation

4.2.1 Model

The theory outlined here is the *tug-of-war* model introduced in [103–105]. We consider a cargo which is attached to N_+ kinesin motors and N_- dynein motors. These motors stochastically bind/unbind to/from a cytoskeletal filament. Depending on the number of kinesin and dynein motors that bind to the filament, the state of the cargo is determined at time t. We consider n_+ and n_- as the number of bound kinesin and dynein motors respectively. Since the maximum number of kinesins and dyneins that can attach to the filament are $N+$ and $N-$, we have $0 < n_+ < N_+$ and $0 < n_- < N_-$. The probability of the cargo to have n_+ attached kinesins and n_- attached dyneins at time t is given as $p(n_+, n_-, t)$. The time evolution of this probability distribution is governed by a master equation which we will discuss in Chapter 5. Let $\pi_\pm(n_+, n_-)$ and $\varepsilon_\pm(n_+, n_-)$ define the binding and unbinding rates of a single kinesin (plus) and single dynein (minus) motor when the cargo is in the state (n_+, n_-).

To write down these rates from the single motor rates that we had discussed in Chapter 1, we assume that the motors act independently and that the load force is shared equally between the motors. In this scenario, if F_+ and F_- denotes the load forces felt by each plus and each minus motor (therefore generating $-F_+$ and $-F_-$ forces themselves), force balance gives $n_+F_+ + n_-F_- = 0$ so that,

$$F_c(n_+, n_-) \equiv n_+F_+ = -n_-F_- \tag{4.4}$$

is the force on the cargo. The effective unbinding rate of a plus motor is given by

$$\varepsilon_+(n_+, n_-) = n_+\varepsilon_{0+} exp[F_c/(n_+F_{d+})] \tag{4.5}$$

and the binding rate is given by

$$\pi_+(n_+, n_-) = (N_+ - n_+)\pi_{0+}. \tag{4.6}$$

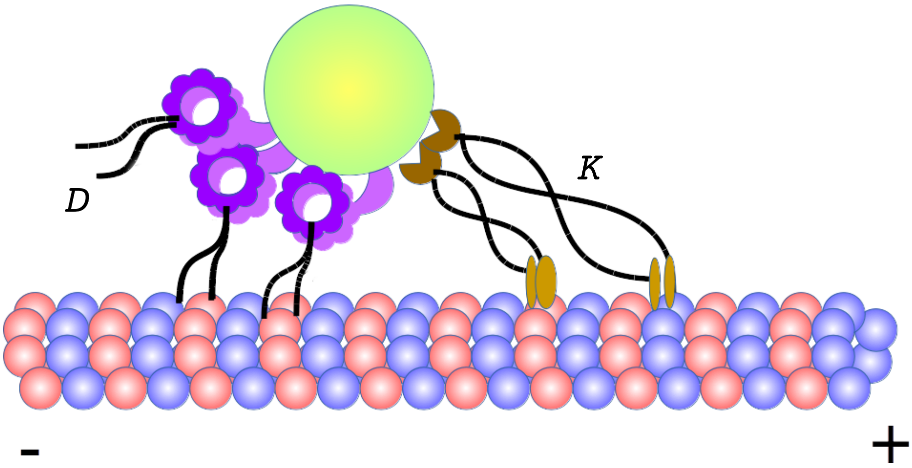

Figure 4.3: Schematic of bidirectional motion of cargo (C) attached to both kinesin (K) and dynein (D) motors on a microtubule (MT) filament.

Dynein motors exhibit catchbonding at forces larger than the stall force, F_{s-}, defined as the load force at which the cargo stalls [17, 113, 131]. This catchbonding regime is characterized by a decreasing detachment rate with increasing opposing load (see Fig. 4.2). With the assumption of equal load sharing, the phenomenological TFBD model for the unbinding rate of a dynein in an (n_+, n_-) state [130, 132], gives

$$\varepsilon_- = n_- \varepsilon_{0-} \exp[-E_d(F_c) + F_c/(n_- F_{d-})] \tag{4.7}$$

where the deformation energy E_d sets in at $F > F_{s-}$, and is given as [130],

$$E_d(F_c) = \Theta(F_c/n_- - F_{s-})\alpha \left[1 - \exp\left(-\frac{F_c/n_- - F_{s-}}{F_0}\right)\right] \tag{4.8}$$

The parameter α sets the strength of the catch bond, while F_{d-} and F_0 characterize the force scales for the dissociation energy and the deformation energy respectively. The binding rate of dynein motor is given as

$$\pi_-(n_+, n_-) = (N_- - n_-)\pi_{0-}. \tag{4.9}$$

The expression for the cooperative force felt by the motors is given by [104]

$$F_c(n_+, n_-) = \frac{n_+ n_- F_{s+} F_{s-}}{n_- F_{s-} v_{0+} + n_+ F_{s+} v_{0-}} (v_{0+} + v_{0-}) \tag{4.10}$$

Parameter	Kinesin	Ref.	Dynein	Ref.
$F_{s\pm}$	6 pN	[42]	1 pN (Weak) 7 pN (Strong)	[133] [134]
$F_{d\pm}$	3 pN	[42]	0.67 pN	[113, 130]
$\pi_{0\pm}$	5/s	[135]	1/s	[136]
$\varepsilon_{0\pm}$	1/s	[42]	(0.1 - 10)/s	[137]
$v_{F\pm}$	$0.65\mu m/s$	[138]	$0.65\mu m/s$	[139]
$v_{B\pm}$	$1nm/s$	[138]	$1nm/s$	[140, 141]

Table 4.1: Single motor parameter values used in the simulations. The deformation force scale F_0 is a phenomenological parameter, as determined in Ref. [130].

and the cargo velocity is given by

$$v_c(n_+, n_-) = \frac{n_+F_{s+} - n_-F_{s-}}{n_-F_{s-}/v_{0-} + n_+F_{s+}/v_{0+}} \tag{4.11}$$

Here, $v_{0\pm}$ denotes the velocity of kinesin (or dynein) motors,

$$v_{0+} = \begin{cases} v_{F+} & if \quad v_c > 0 \\ v_{B+} & if \quad v_c < 0 \end{cases} \text{ and } v_{0-} = \begin{cases} v_{F-} & if \quad v_c < 0 \\ v_{B-} & if \quad v_c > 0 \end{cases}$$

where, v_F and v_B are the forward and backward motor velocities. Finally the stall forces for the two motor species are denoted by $F_{s\pm}$. The parameters used in the study are taken from the literature, and are summarized in Table 4.1.

4.2.2 Methods

4.2.2.1 Stochastic Simulation Algorithm (SSA) with equal load sharing

In order to obtain dynamical quantities we first perform simulations of cargo movement in one dimensions over a track, using the Gillespie algorithm [142, 143]. Individual trajectories are generated by performing binding/unbinding kinetics of cargo and allowing the motion of the cargo with velocity v_c when bound. All possible initial configurations were generated for a (N_+, N_-) pair, and 1000 trajectories were evolved for each initial configuration. A run finishes if the simulation continues until the maximum time $T_{max} \sim 10^4 s$ or if all motors detach from the MT. The run length was then averaged over all initial configurations and all iterations. Probability distributions were also computed from the SSA trajectories after discarding initial transients. In these simulations we assume that the load is shared equally by the motors. In the following section, we discuss brownian dynamics simulations of cargo in presence of motor proteins where this mean field condition is relaxed and the load is shared stochastically.

4.2.2.2 Brownian dynamics with stochastic load sharing

.

In order to ensure that the codependent transport characteristics obtained are not artifacts of the mean field assumption, where motors are assumed to share the load force equally, we also performed Brownian dynamic simulations where the load is shared stochastically, with each motor having a different extension, and hence facing a different opposing load. In the simulation, N motors are attached to the cargo. The motors are modeled as elastic springs with spring constant $k = 0.32$ pN/nm. The springs have a rest length l_0 and generate a restoring force only when stretched beyond the rest length. The rest length of the springs are chosen in accordance with earlier simulations, $l_0 = 100$ nm for kinesin and $l_0 = 50$ nm for dynein. In this one dimensional model, we start by putting the bead at the origin and all N motors attached irreversibly to the cargo at one end. The other end of the motors are allowed to bind to any point on the track within the rest length of the corresponding motor, on either side of the bead.

At every time step, all the N motors are visited to determine if they are in the attached or detached state. Each motor position and their state are updated only once in a time step. If the motor is in the detached state, then it can re attach with a probability $P_{\text{on}} = \pi_{\pm}\Delta t$, where $\pi_{\pm}$ are the binding rates of kinesin and dynein as defined earlier. The attachment happens within a distance l_0 on either side of the bead. If the ith motor is in an attached state, then the load force, F_i is calculated by multiplying the extension of the spring with the spring constant k. Depending on the load force, the motor could detach, with probability $P_{\text{off}} = \varepsilon_{\pm}(F_i)\delta t$, where $\varepsilon_{\pm}$ are the unbinding rates of kinesin and dynein. If the motor does not detach, then we calculate the probability of taking a step, $P_{\text{step}} = k_{\text{step}}\Delta t$, where $k_{\text{step}} = (v_{0\pm}/d)(1 - F_i/F_{s\pm})$, where $v_{0\pm}$ is the unloaded velocity of the single motor, $F_{s\pm}$ is the stall force of the motor and $d = 8$ nm is the step length of the motor. Note that this form is used for forward loads $F_i < F_s$. For backward loads $F_i > F_s$, $P_{\text{step}} = 0$. For no loads, $F_i = 0$. If the motor steps, its position is updated from x_i to $x_i + d$. All motor states and their positions are updated simultaneously in a given time step. Two sets of motors with their characteristic parameters as given in Table 4.1, move in opposite directions.

To update the position of the cargo (modeled as a bead of radius σ), we calculate the total force acting on the cargo due to both sets of molecular motors moving in

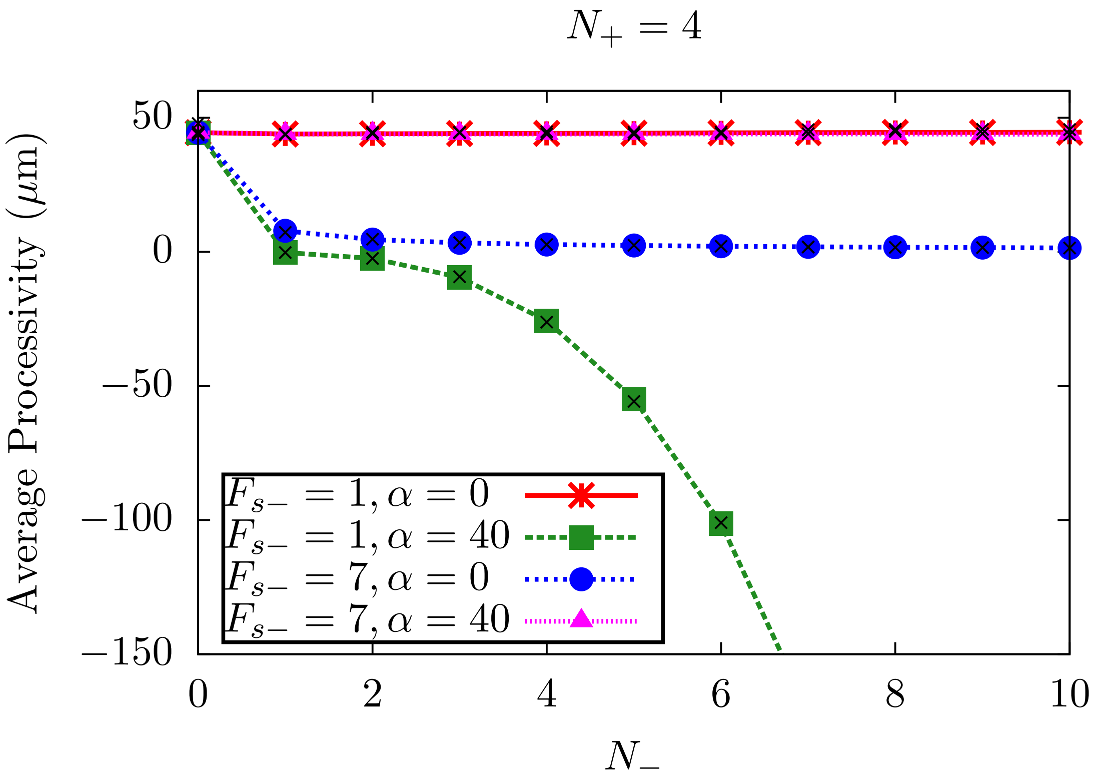

Figure 4.4: Average processivity as a function of N_- for $N_+ = 4$. The colored points and lines are obtained using SSA. The zero-force (un)binding rates for dynein are $\varepsilon_{0-} = \pi_{0-} = 1/s$.

opposite directions, $F_{\text{tot}} = \sum F_i$. Note that the detached motors do not contribute to the total force, neither do the motors which lie within a rest length from the bead position. The bead is under the influence of both thermal and viscous forces with $\xi = 0.001$ pN-s/$\mu - m^2$ being the viscosity of the medium. The bead diffuses with diffusion constant $D = k_B T/\zeta$ where $\zeta = 6\pi\xi\sigma$ is the friction constant. When the cargo is subjected to the force F_{tot} it moves with the velocity $v_d = F_{\text{tot}}/\zeta$. In the presence of thermal noise, the overdamped Brownian dynamics of the cargo is given by

$$\mathbf{x}(t + \Delta t) = \mathbf{x}(t) + v_d \Delta t + \eta \tag{4.12}$$

where η are drawn Gaussian distribution with $\langle \eta(t) \rangle = 0$ and $\langle \eta(t)\eta(t') \rangle = 2D\delta(t-t')$.

4.3 Results

4.3.1 Cargo Processivity Characteristics

In Fig. 4.4, we show SSA results which look at the effect of variation of number of dynein motors, N_-, on processivity, defined as the net displacement of the cargo until it unbinds. In the absence of catch bond ($\alpha = 0$), for a fixed value of N_+, the processivity decreases continuously with increasing N_- although staying positive throughout, indicating a decreasing net movement in the positive direction, as expected from the conventional tug-of-war argument. Within the range of parameters investigated in our model, the dynein stall force has no effect on the behavior. When catch bond is incorporated ($\alpha > 0$), the consequences are quite dramatic. For 'strong' dynein ($F_{s-} = 7$pN), the processivity in the positive direction drops significantly even for one dynein motor, almost stalling the cargo. Increasing N_- further, eventually stalls the cargo, with no movement observed in either direction. For 'weak' dynein ($F_{s-} = 1$pN), increasing N_- not only stalls the cargo, but also forces it to move in the negative direction. 'Weak' dynein switches on its catchbond at smaller values of load force, leading to an increased propensity to latch on to the filament. This results in negative-end directed motion even for a small number of dynein motors. 'Strong' dynein does not engage its catchbond until at relatively high values of load force. Although this helps lowering the processivity, it is not sufficient to pull it in the negative direction, therefore bringing it to a stall. This feature simultaneously highlights the role of catchbonding in mediating codependent transport, including reversal of direction of cargo traffic, and the role of the stall forces of the dynein motors in determining transport behavior of cellular cargo.

Diverse experiments have indicated that mutations of conventional kinesin in *Drosophila* can hamper motion of cellular cargo in both directions, by effectively reducing the number of motors attached to the cargo [109, 110, 144–146]. To investigate this, in Fig. 4.5, we look at the effect of variation of N_+ on processivity, for a fixed value of N_-. Remarkably, the average processivity for weak dynein shows a non-monotonic behaviour with increasing N_+. In particular *there is decrease of processivity in the negative direction on decreasing the number of plus-end directed motors.* This is a singular feature arising solely due to catchbonding in dynein, contrary to usual tug-of-war predictions, and is reminiscent of the *paradox of codependence.*

This codepedent behaviour exemplified in processivity characteristics may be understood in terms of the catchbond mechanism at play. In the absence of opposing load, increasing N_+ has the effect of increasing processivity in the plus direction. How-

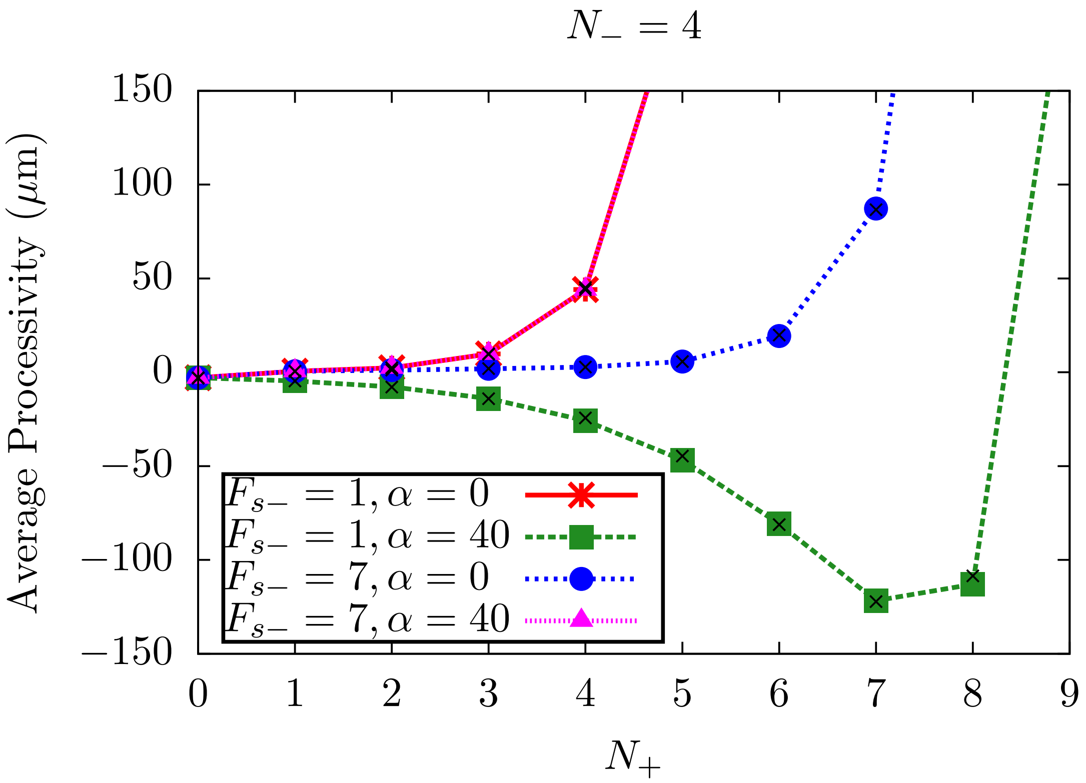

Figure 4.5: Average processivity as a function of N_+ for $N_- = 4$. The colored points and lines are obtained using SSA. The zero-force (un)binding rates for dynein are $\varepsilon_{0-} = \pi_{0-} = 1/s$.

ever in the presence of dynein, with larger number of kinesins, the load per dynein is higher, leading to engagement of the catchbond and thus fewer detachment events for dynein. The cargo is now in a tug-of-war state, leading to higher detachment forces on the opposing kinesins, which detach with the usual slip kinetics. Thus, on average, for some parameter regime, the kinesins detach at a higher rate than dyneins, leading to more configurations where there are no kinesins opposing the dynein team. Thus although the direct effect of the catch bond is a larger value of average unbinding time for dyneins, this leads to more configurations where the dyneins can walk towards the negative end leading to codependent transport.

The robustness of this catchbond mediated phenomenon can be further observed from the results of our brownian dynamics simulations where the load is shared stochastically between the motors. In Fig. 4.6, we show the results of average processivity for different values of the cargo size. As with the mean field results where load is equally shared, we observe that the average processivity during stochastic load sharing also gives rise to negative processivity with increasing number of kinesin motors. This non-monotonic feature is more pronounced at larger bead sizes. The

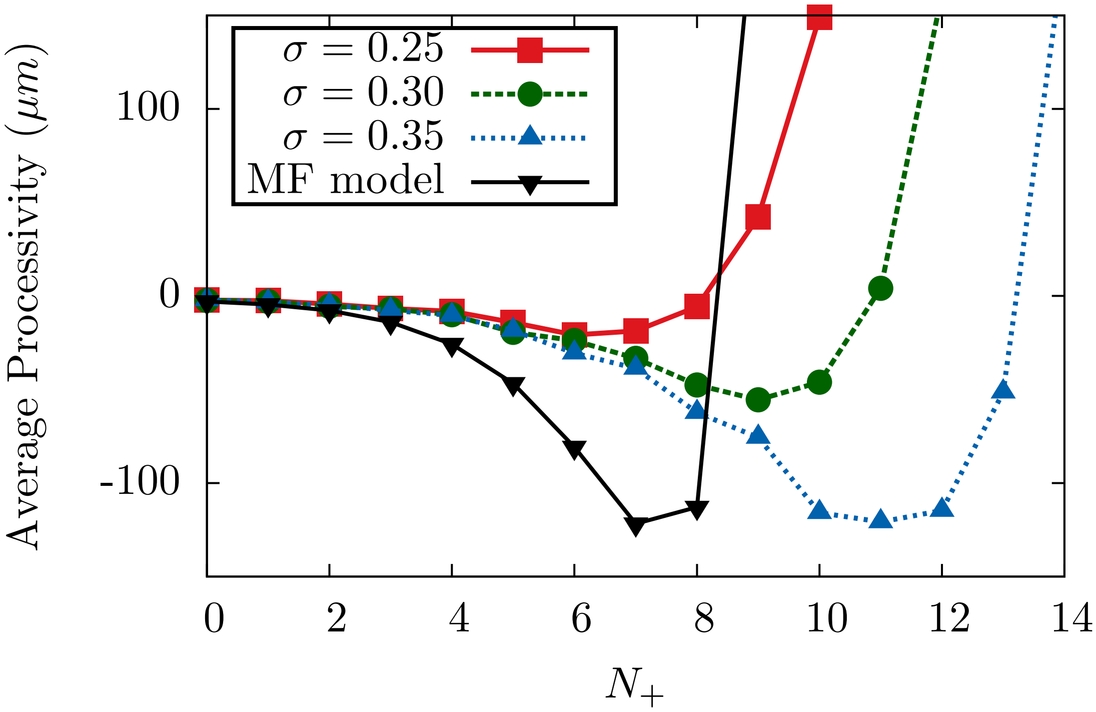

Figure 4.6: Average processivity as a function of N_+, as the bead size σ is changed. Note that the friction constant ζ changes as a result. The blue curve shows the corresponding result under the equal load sharing assumption. Here $N_- = 4$, $\alpha = 40$ and $F_o = 7pN$.

change in size of the cargo (σ) changes the friction ζ. At higher values of σ, the processivity in the negative direction increases as the effect of catch-bond is in full effect at higher loads.

The corresponding contour plots of the processivity of the cargo, which provide an experimental testbed, in the ($N_+ - N_-$) plane are shown in Figs. 4.7, 4.8, for 'weak' dynein where the effect of dynein catch-bond is robust. As expected, in the absence of catch-bond ($\alpha = 0$) (Fig. 4.7), there is a smooth transition from negative-directed runs to positive directed runs. In the presence of catch-bonded dynein (Fig. 4.8), we observe a distinct regime where the processivity increases in the negative direction on increasing N_+, reminiscent of anomalous codependent transport. Plus-end directed motion now occurs only for large N_+ and low N_-. This non-trivial effect of the catch bond is a robust feature that is observed for other values of kinesin and dynein motors.

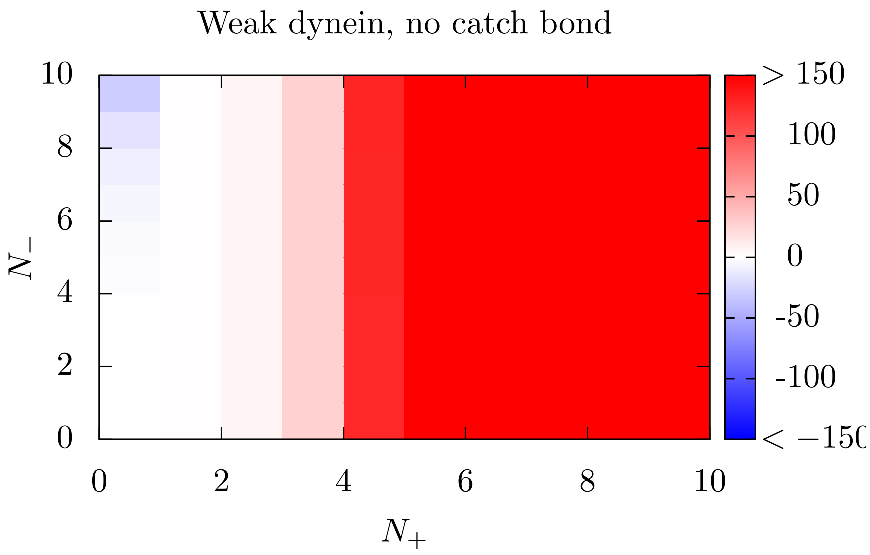

Figure 4.7: Contour plots for processivity obtained using SSA in the $N_+ - N_-$ plane for $F_{s-} = 1pN, \alpha = 0$, The color bar indicates the average processivity (in μm). The zero-force (un)binding rates for dynein are $\varepsilon_{0-} = \pi_{0-} = 1/s$.

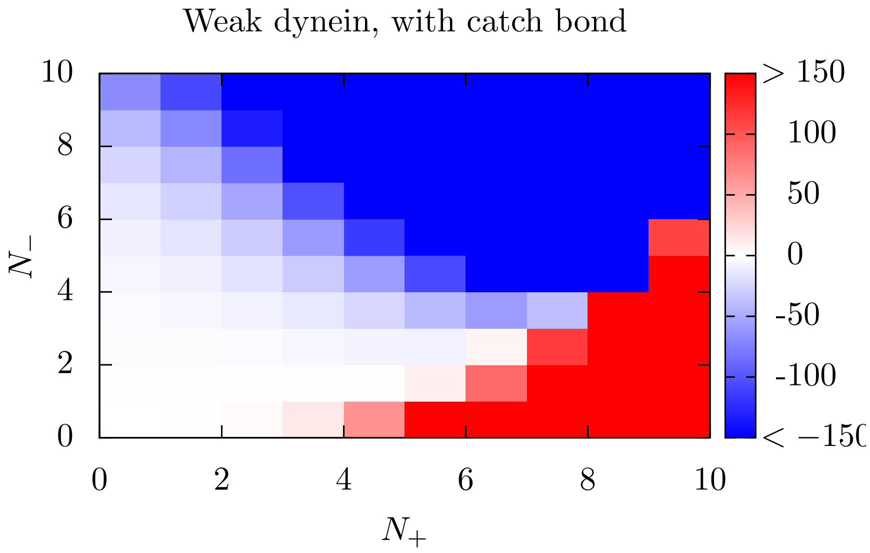

Figure 4.8: Contour plots for processivity obtained using SSA in the $N_+ - N_-$ plane for $F_{s-} = 1pN, \alpha = 40k_BT$, The color bar indicates the average processivity (in μm). The zero-force (un)binding rates for dynein are $\varepsilon_{0-} = \pi_{0-} = 1/s$.

4.3.2 Probability distribution of runtimes and cargo velocities

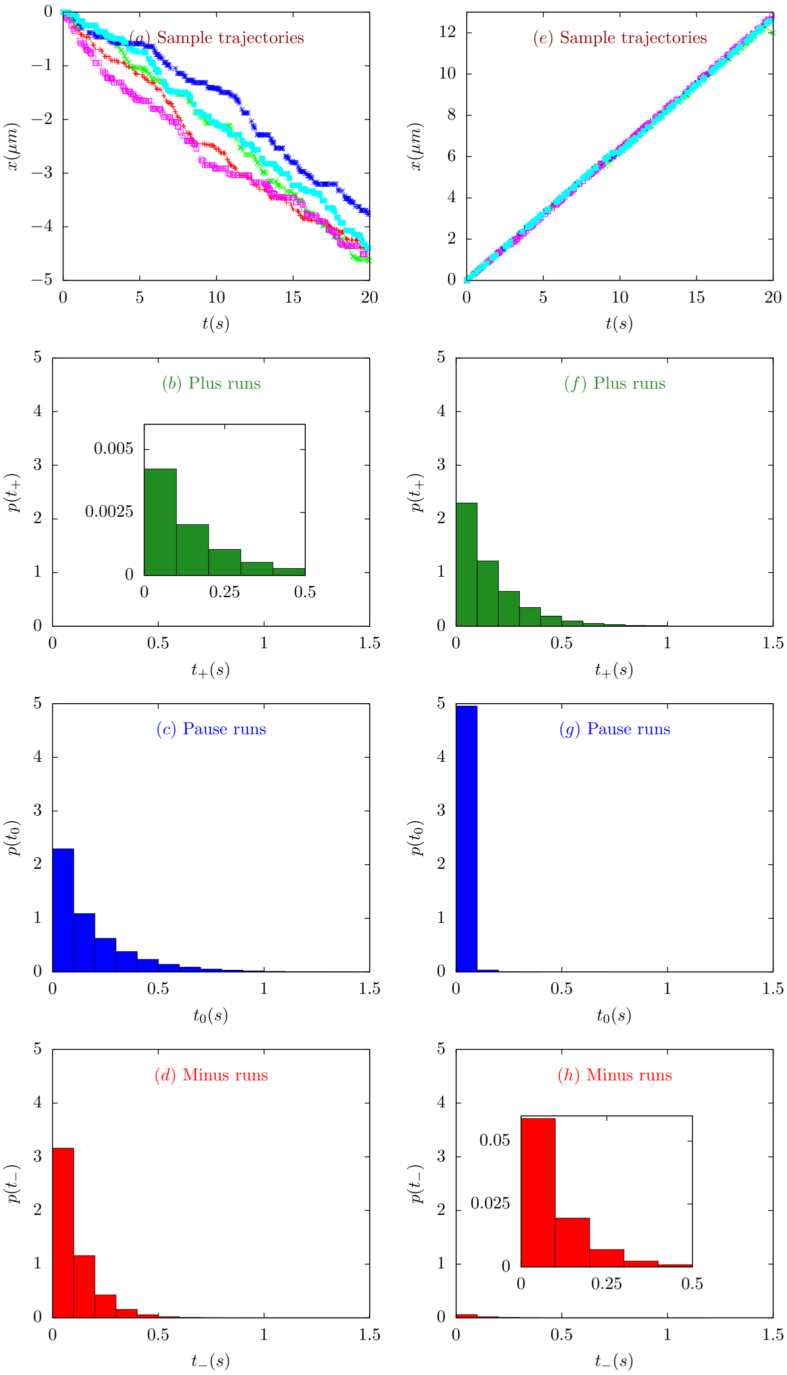

Figure 4.9: Probability distributions of runtimes for $N_+ = 2$, $N_- = 6$. The left panels show the normalized histograms and sample trajectories for dynein in the presence of catch bond ($\alpha = 40$). The right panels show the corresponding quantities in the absence of catch-bond ($\alpha = 0$). (a) and (e) Sample trajectories; (b) and (f) distributions of runtimes for plus directed runs (shown in green); (c) and (g) pause time distributions (shown in blue); (d) and (h) distributions of runtimes for minus directed runs (shown in red); and insets in (b) and (h) show magnified views of the corresponding distributions.

In order to highlight the role of catchbond we provide quantitative measures which are biologically relevant for comparison with experimental data related to trajectories of cellular cargo carried by molecular motors. We analyze the probability distribution of the time the cargo spends in the paused (*tug-of-war*) state versus the time it spends in the moving plus-end directed and minus-end directed state, as well as the probability distribution of the velocities of the cargo.

Motivated by experiments on *dictyostelium* cell extracts [96], we study the transport behaviour of a cargo with $N_+ = 2$ and $N_- = 6$ (Fig. 4.9). In the absence of catchbonding, cargoes predominantly move with positive velocity and the resultant motion is strongly plus-end directed (Fig. 4.9(e)). The probability distributions of runtimes show that there are many more kinesin runs (Fig. 4.9(f)) than dynein runs (Fig. 4.9(h)), and the average runtime is also higher in the case of kinesins. The pauses in this case are also of extremely short duration (Fig. 4.9(g)).

In contrast, when dynein catch bond is switched on, the picture changes dramatically. While the cargo is in a paused state a siginificant fraction of time, around 35% of its runs are negative directed (Fig. 4.9(d)). Minus-ended runs become much more frequent than plus-ended runs, while the average pause time also increases by an order of magnitude compared to the non-catchbonded case, and becomes comparable to the average minus directed runtimes. This is shown in Figs. 4.9(b)-(d). This prediction of minus-ended runs with intermittent pauses qualitatively agrees with the experimental observation of transport of endosomes in *Dictyostelium* cells [96].

In a separate set of experiments on early endosomes in fungi, a team of many kinesin motors (3-10) are involved in *tug-of-war* with 1 or 2 dynein motors during transport [102]. The results displayed in Fig. 4.10 for a cargo being transported by six kinesins and two dyneins illustrates that while in the absence of catchbonding in dynein, the resultant motion would be strongly plus-end directed, with very small pause times, incorporation of catchbonding results in the frequency of minus-ended runs exceeding the frequency of plus-ended runs by almost one order of magnitude. However, the average duration of the minus-ended runs is about one order of magnitude lower than that of the plus-end directed run duration. Further there are now substantial duration of pauses ($1 - 4$ sec) during transport. These characteristics of the probability distributions result in typical cargo trajectories which exhibits bidirectional motion with pauses.

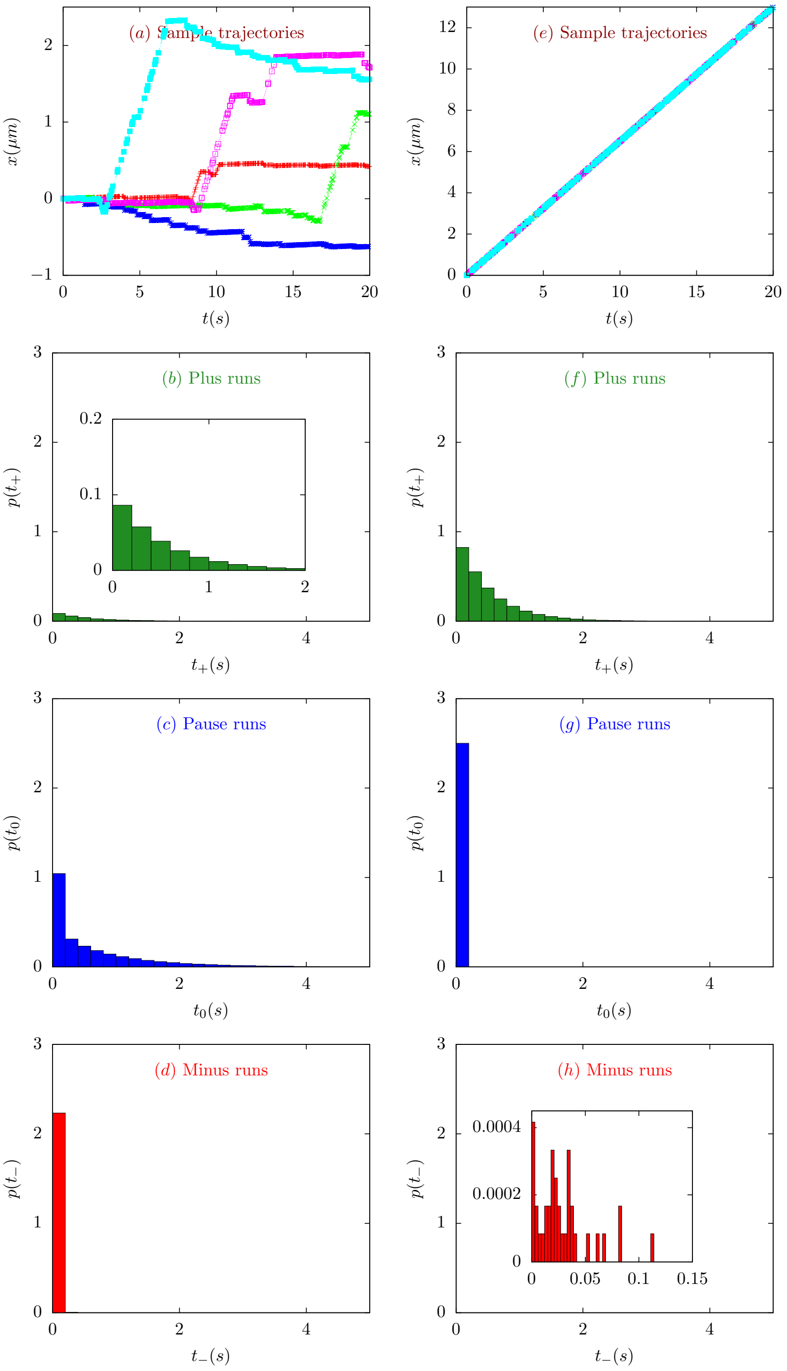

Figure 4.10: Probability distributions of runtimes for $N_+ = 6$, $N_- = 2$. The left panels show the normalized histograms and sample trajectories for dynein in the presence of catch bond ($\alpha = 40$). The right panels show the corresponding quantities in the absence of catch-bond ($\alpha = 0$). (a) and (e) Sample trajectories; (b) and (f) distributions of runtimes for plus directed runs (shown in green); (c) and (g) pause time distributions (shown in blue); (d) and (h) distributions of runtimes for minus directed runs (shown in red); and insets in (b) and (h) show magnified views of the corresponding distributions.

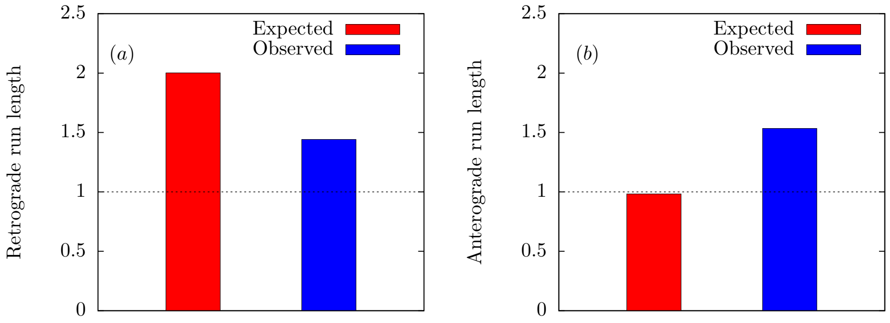

Figure 4.11: Histograms showing scaled (a) retrograde and (b) anterograde run lengths with *non-catchbonded* (Expected, red, $\alpha = 0$) and *catchbonded* (Observed, blue, $\alpha = 40k_BT$), when N_+ is changed from 3 to 2, while $N_- = 4$. The scaling is done with respect to the control (without kinesin inhibition) and corresponds to $N_+ = 3$. The zero-force (un)binding rates for dynein are $\varepsilon_{0-} = \pi_{0-} = 1/s$

4.3.3 Quantitative comparison with experiments

In order to provide a quantitative comparison of our results with in-vivo experiments, we consider the specific case of kinesin inhibition in mouse neurons [111]. It was observed that inhibiting kinesin resulted in smaller retrograde run lengths of prion protein vesicles, which is contrary to expectations - a signature of codepedent transport behaviour. In our model, kinesin inhibition is incorporated by reducing the number of kinesins (N_+) from 3 to 2 while the dynein number is held fixed ($N_- = 4$). As shown in Fig. 4.11, this reduction in kinesin motors leads to smaller retrograde run lengths and larger anterograde run lengths when catch bond is switched on in dynein, as opposed to the situation when dynein unbinding exhibits slip behavior. This is the scenario of co-dependent transport and compares well with the experimental observations. Our assumption that kinesin inhibition leads to reduction in its number is a simplified view of the effect of the inhibition experiment in in-vivo conditions. Nonetheless, even with this assumption our results definitively points to the role of catchbond mediated mechanism in determining codependent transport behaviour.

4.4 Conclusion

In summary, the findings of our model point to the crucial role played by catchbonding in dynein motors in internally regulating transport and providing a possible resolution of the paradox of codependence. It also provides a framework to interpret diverse set of experiments where regulation of transport is achieved by different modes of modification of the motor properties. For instance, while decreasing N_- has the effect of weakening the dynein motor action, the manifestation of these two effects in the transport characteristics can in general be distinct. The results of these experiments can then qualitatively be understood in the light of Fig. 4.4, where weakening the dynein motor can lead to stalled motion of the cargo. Interestingly, while kinesin exhibits a conventional slip bond, the cooperative force exerted by the catch bonded dynein on kinesins, and vice-versa, introduces a complex interplay which results in signatures of codependent transport being observed even on varying effective kinesin numbers. This effect is reflected in a preliminary comparison of processivity measurements for prion protein vesicles in mouse neurons [111] with our model predictions.

Apart from the internal regulatory mechanism described here, external regulation by associated proteins is also expected to play an important role in determining the transport characteristics. Various candidate proteins such as *Klar* and JIP1 have been shown to modify transport behaviour [94, 100, 110, 147–154]. Further, various other factors, such as memory effects during motor rebinding [131], interactions between multiple motors [155, 156], variable dynein step sizes [113, 128], and stochastic load sharing could also modify the transport behaviour of the cargo. However we show using simulations incorporating a stochastic sharing of load between attached motors, that the codependent behavior of cargo processivity is robust and is preserved even with additional inputs such as viscous friction and thermal noise.

Various regulatory mechanisms are expected to achieve coordination through different means which may be reflected in the transport characteristics of the cargo. For example, in the case of the catch-bonded tug-of-war mechanical model, the pause state would in general be characterized by a slow velocity of the cargo. On the other hand, for mechanical inhibition [98, 157], microtubule tethering mechanism [98, 158] or steric disinhibition [98, 159], the motion of the cargo would either be diffusive or would show no movement. Increasing the binding rates of either motor species would result in shorter pause times if coordination is achieved through mediation by the catch bond, while it would have no effect on the pause times for some other mechanism. A careful examination of high resolution spatio-temporal measurement of cargo processivity and pause durations obtained in various experiments is required to delineate the relative importance of these internal regulatory mechanisms.

To conclude, we show that catchbonding in dynein dramatically alters the transport characteristics, and manifests as an internal regulatory mechanism that provides one possible resolution of the *paradox of codependence*.

Chapter 5

Motility diagrams for bidirectional transport in the presence of dynein catch bond

In the previous chapter, we have outlined the motivation of studying bidirectional transport of cargo when the detachment characteristics of dynein show a unique slip-catch-slip behavior. We studied bidirectional transport in the context of the *tug-of-war* model which is based on the hypothesis that the motors act independently, stochastically binding and unbinding from the filament and mechanically interacting with each other through the cargo that they carry. The resultant motion arises due to the competition between the oppositely directed motors with the direction of transport being determined by the stronger set of motors.

Experimental support for this mechanical interaction between the two sets of motors in the tug-of-war model comes from measurements of stall forces for beads bound only to kinesin, as compared to beads bound both by kinesin and dynein, the stall forces were lowered in the second case, supporting the hypothesis of mechanical competition between the motors. Further both in-vitro and in-vivo experiments to study transport of neuronal vesicles show good qualitative and quantitative agreement of simulated cargo trajectories with observed experimental data. In particular the experiments exhibited cargo trajectories which were characterized by (a) robust runs in both direction, (b) net plus-end runs with frequent pauses, when the dynein stall force was reduced (c) and smooth plus-end directed run when the dissociation rates of dynein was reduced substantially. These characteristics were reproduced in the simulated cargo trajectories for the theoretical tug-of-war model with the specific values of the biological parameters that corresponded to the experimentally measured value of these parameters. Similar agreement of cargo trajectories was observed for the case of endosome transport in D. discoideum cells. Further, these experiments observed vesicle elongation when attached to both motor species providing further support for the mechanical tug-of-war hypothesis.

However, as we showed in Chapter 4, there are a large number of experiments which are in contradiction with this model. Incorporating the exact nature of the dynein detachment rate in the tug-of-war picture using the TFBD model that we have discussed in detail, we showed that incorporation of catchbonding behaviour reproduces both the tag-of war model transport characteristics and codependent transport characteristics in appropriate biological regimes. In this chapter, we continue the discussion and report preliminary results on the motility states of the cargo which are obtained from the stationary state solution of the master equation given below.

5.1 Master equation

In our model, we had taken two sets of molecular motors : N_+ kinesin motors and N_- dynein motors which are attached to a cargo. The motors stochastically attach and detach from a MT filament. The force generated due to the opposing teams of motors is assumed to be distributed equally between the attached motors. The state of the cargo at any instant of time is specified by the number of attached motors : n_+ kinesin and n_- dynein. The time evolution of the cargo is then governed by the master equation

$$\begin{aligned}\frac{\partial p(n_+, n_-, t)}{\partial t} &= p(n_+ + 1, n_-)\epsilon_+(n_+ + 1, n_-) + p(n_+, n_- + 1)\epsilon_-(n_+, n_- + 1) \\ &\quad + p(n_+ - 1, n_-)\pi_+(n_+ - 1, n_-) + p(n_+, n_- - 1)\pi_+(n_+, n_- - 1) \\ &\quad - p(n_+, n_-)\left[\epsilon_+(n_+, n_-) + \epsilon_-(n_+, n_-) + \pi_+(n_+, n_-) + \pi_-(n_+, n_-)\right]\end{aligned} \tag{5.1}$$

where $p(n_+, n_-, t)$ is the probability to find the cargo with n_+ attached kinesins and n_- attached dyneins at a time t. $\pi_\pm$ and $\varepsilon_\pm$ denote the attachment and detachment rates of kinesin and dynein motors as discussed in Chapter 4. Note that the dynein detachment rate is given by the TFBD model as described in the previous chapter.

5.2 Motility states

We write master equation as product of rate matrix and probability column vector on one side and the time derivative of probability column vector on the other side.

$$\begin{bmatrix} r_{11} & r_{12} & .. & .. & r_{1N^*} \\ r_{21} & r_{22} & .. & .. & .. \\ .. & & & & \\ .. & & & & \\ .. & & & & \\ .. & & & & \\ r_{N^*1} & .. & .. & & r_{N^*N^*} \end{bmatrix} \begin{bmatrix} p_1(0,0) \\ p_2(0,1) \\ .. \\ p_s(1,0) \\ p_{s+1}(1,1) \\ .. \\ p_{N^*}(N_+,N_-) \end{bmatrix} = \begin{bmatrix} \frac{\partial p_1(0,0)}{\partial t} \\ \frac{\partial p_2(0,1)}{\partial t} \\ .. \\ \frac{\partial p_s(1,0)}{\partial t} \\ \frac{\partial p_{s+1}(1,1)}{\partial t} \\ .. \\ \frac{\partial p_{N^*}(N_+,N_-)}{\partial t} \end{bmatrix}$$

where $N^* = (N_+ + 1) \times (N_- + 1)$ and the transition matrix elements $r_{m,n}$ are given in terms of the attachment and detachment rates, $\pi_\pm$ and $\varepsilon_\pm$, of kinesin and dynein motors. For stationary state, all elements of the right hand side column vector is zero and we get,

$$\begin{bmatrix} r_{11} & r_{12} & .. & .. & r_{1N^*} \\ r_{21} & r_{22} & .. & .. & .. \\ .. & & & & \\ .. & & & & \\ .. & & & & \\ .. & & & & \\ r_{N^*1} & .. & .. & & r_{N^*N^*} \end{bmatrix} \begin{bmatrix} p_1(0,0) \\ p_2(0,1) \\ .. \\ p_s(1,0) \\ p_{s+1}(1,1) \\ .. \\ p_{N^*}(N_+,N_-) \end{bmatrix} = \begin{bmatrix} 0 \\ 0 \\ .. \\ 0 \\ 0 \\ .. \\ 0 \end{bmatrix}$$

The stationary state solution of the above equation is then solved as the null space of the transition matrix in *Mathematica*. The probability of the cargo to be in a state (n_+, n_-) is determined and the maxima of the distribution $p(n_+, n_-)$ identifies the different states of the cargo. The possible states that can be identified are as follows :

- Positive end directed fast motion (+) : This happens when $n_- = 0$ and $n_+ > 0$ so that the cargo has only kinesin motors attached and it moves rapidly in the positive direction.

- Negative end directed fast motion (−) : This happens when $n_+ = 0$ and $n_- > 0$ so that the cargo has only dynein motors attached and it moves rapidly in the negative direction.

- Pause or very slow movement (0) : This happens when $n_- > 0$ and $n_+ > 0$. The cargo moves in the direction of the motor type which win the tug-of-war. However, the motion is small since the motors which walk backward very slowly.

- Unbound state : This happens when $n_+ = n_- = 0$ and the cargo is unbound.

5.2.1 Symmetric tug-of-war

Here, we consider the situation where the number of plus and minus directed motors are the same, i.e. $N_+ = N_-$. Further, both sets of motors are assumed to have the same single-motor parameters. We take both sets to have the same dynein parameters as we compare the scenario where the detachment rate is a slip bond with the slip-catch-slip scenario. The maxima in the probability distribution are obtained as combinations of the states described above : a no motion state (0), a fast plus and minus motion state $(-+)$ and a fast plus and minus motion state with intermittent pauses $(-0+)$. For this symmetric situation, we can define dimensionless ratios : (i) desorption constant $K = \varepsilon_0/\pi_0$ and (ii) force ratio $f = F_s/F_d$. Note that we have dropped the ± notation since both sets have the same single-motor dynein parameters.

5.2.1.1 Probability Method plots

In Fig. 5.1, we plot the motility diagram in the $f - K$ phase space in the absence of dynein catch bond (catch bond strength $\alpha = 0$). As shown in the plot, for various values of f and K, the cargo is in one of the three states : (i) (0) shown in red where the probability distribution shows a single peak at a state where $n_+ = n_- = n$ (ii) $(-+)$ shown in green where the probability distribution shows two maxima at $(n, 0)$ and $(0, n)$ (iii) $(-0+)$ shown in blue where the probability distribution shows three maxima at $n_+ = n_- = n$, $n_+ = 0$ and at $n_- = 0$. For small f which means $F_s \ll F_d$, the motor is in a no motion (0) state. At large f which means $F_s \gg F_d$, the forces are larger than detachment forces and can lead to rapid unbinding of one set of motors leading to the $(-+)$ motility state. Similarly at large desorption constants K the number of motors decreases and one gets an unbound state (shown in grey).

As the dynein catch bond is turned on (see Fig. 5.2), then at large forces, due to the engagement of the catch bond, it becomes very difficult to rip-off any of the set of motors. In this scenario we therefore see large regions of no motion (0) (red) state. At small enough f and higher desorption constants K, the motors can get unbound and we see the emergence of both $(-+)$ (green) and $(-0+)$ (blue) states.

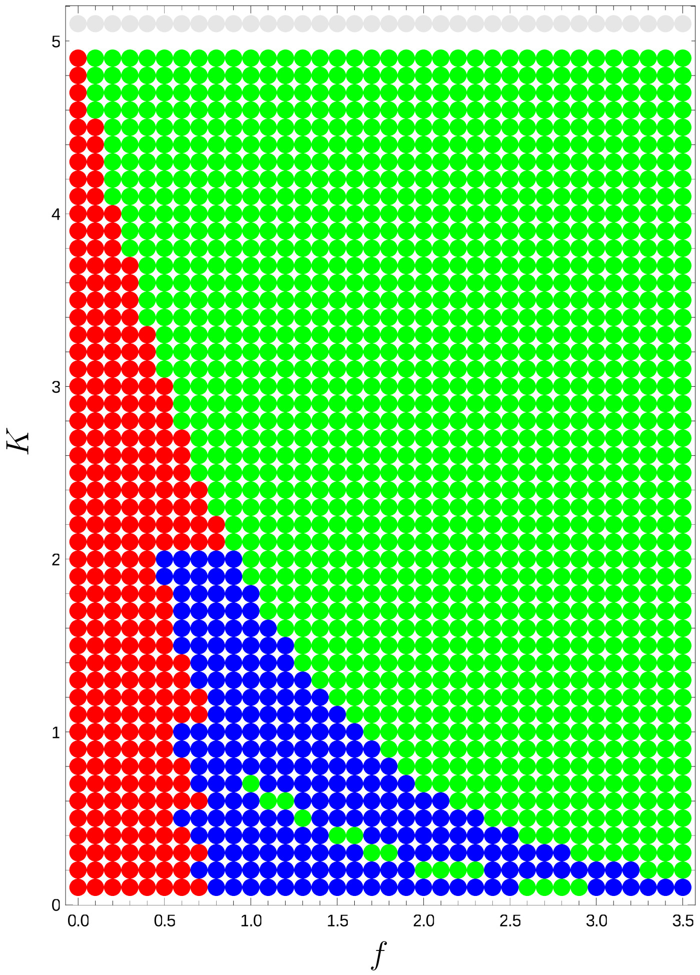

Figure 5.1: Motility diagram for symmetric tug-of-war using only dynein motor parameters with $\alpha = 0$. The number of motors are equal as are the various parameters. $N_+ = N_- = 5,\ F_d = 0.67\ pN,\ F_s = 1.5\ pN,\ F_0 = 7\ pN,\ \pi_0 = 1\ /s,\ v_f = 0.65\ \mu m/s,\ v_b = 1\ nm/s.$

5.3 Asymmetric tug-of-war

Now we consider the original bidirectional tug-of-war scenario with kinesin and dynein motor parameters. Depending on the number and nature of peaks of the probability distribution, the motion is then categorized into one of seven possible classes (Fig. 5.3) as shown below in a phase plot of (N_+, N_-).

Note that the motility diagram approach has some inherent limitations since interpreting the motion in terms of the peaks may give an incomplete picture. In Fig. 5.3, we plot the motility diagram and compare them with the contour plots of the processivity. The motility diagrams do not capture the full complexity of motion in the presence of catch bonds. For weak dynein, the motility diagrams predict that for $N_+ > 1$ and $N_- > 2$, the motion is either paused or in the fast plus with pause state.

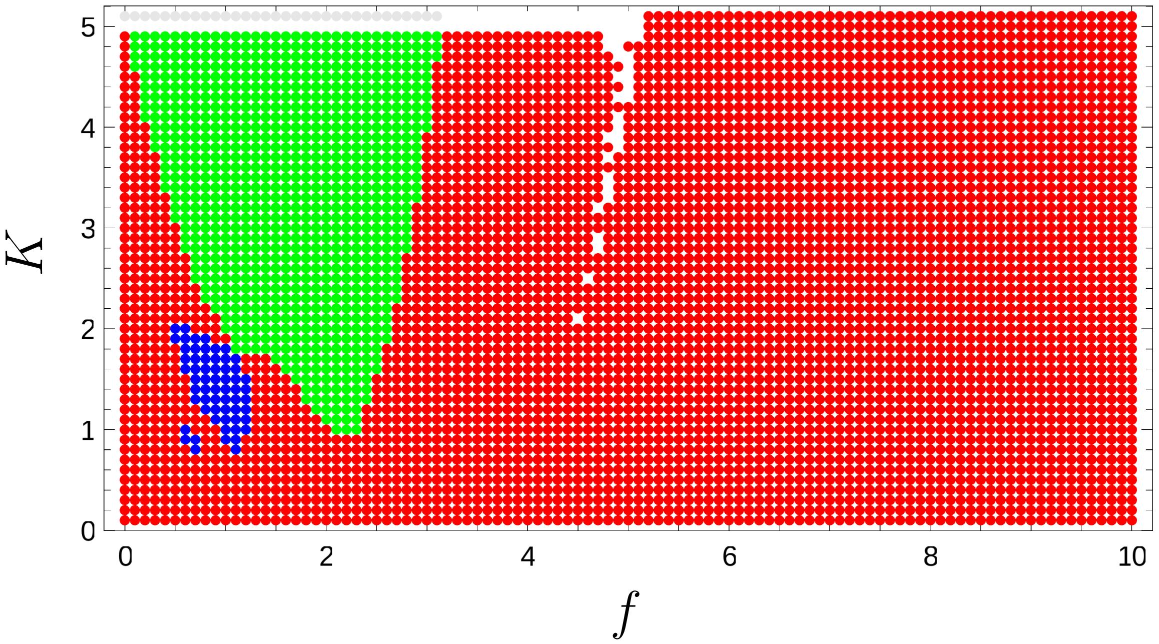

Figure 5.2: Motility diagram for symmetric tug-of-war using only dynein motor parameters with $\alpha = 35$. The number of motors are equal as are the various parameters. $N_+ = N_- = 5,\ F_d = 0.67\ pN,\ F_s = 1.5\ pN,\ F_0 = 7\ pN,\ \pi_0 = 1\ /s,\ v_f = 0.65\ \mu m/s,\ v_b = 1\ nm/s$. Note that some parts are left white since the motility state could not be accurately determined from the probability maxima.

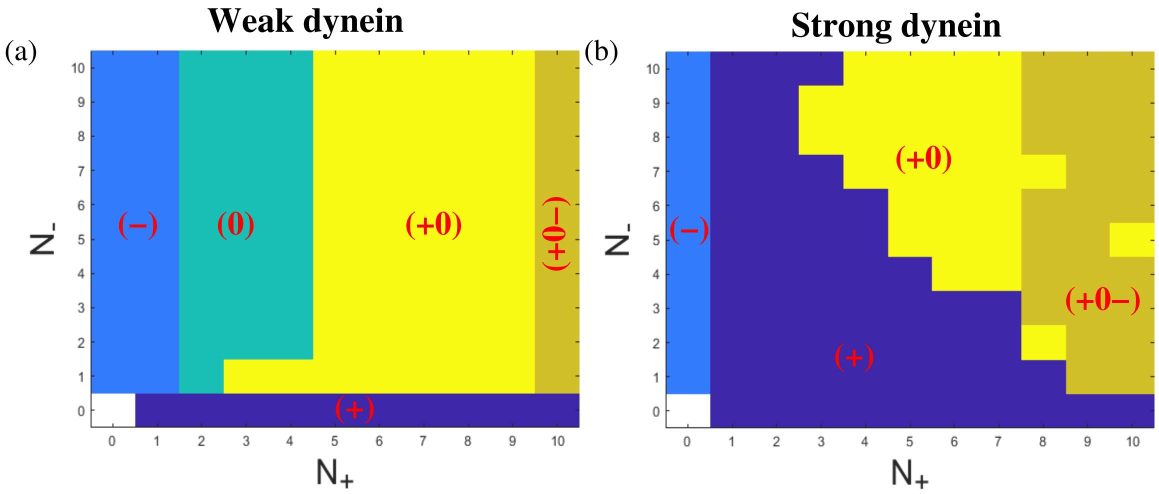

Figure 5.3: Motility diagrams in the $N_+ - N_-$ plane for (a) Weak dynein ($F_{s-} = 1pN$), and (b) Strong dynein ($F_{s-} = 7pN$). There are seven possible motility states, *fast plus* (+), *fast minus* (-), *no motion* (0), *fast plus with pauses* (0+), *fast minus with pauses* (0-), *fast bidirectional motion* (+-), and *fast bidirectional with pauses* (-0+). The parameter values used are the same as in Fig. 4.4.

However, as the processivity contour plots make clear, there is a range of (N_+, N_-) with negative directed runs in this region. This can also be seen by considering the runtime probability distributions shown in Chapter 4. For example for $N_+ = 2$ and $N_- = 6$, we have a minus directed transport interspersed with pauses, while the motility diagram simply predicts a no-motion state.

5.4 Discussion

In this chapter, we have discussed motility states obtained using the steady state probability distribution of bound motors. We have been able to identify several motility states depending on the tug-of-war scenario. In the symmetric case, we have seen a complex dependence of the desorption constant and force ratio on the nature of the detachment characteristics which we have varied from the non-catchbonded to the TFBD scenario. In the asymmetric case, which is the more experimentally relevant scenario, we have seen that the motility diagram obtained in the (N_+, N_-) plane does not show a one to one correspondence with the average processivity contour plots in the same plane obtained using the stochastic simulations, an aspect which is under current investigation.

Chapter 6

Summary

In this thesis, we have studied the explicit role of motor proteins on the dynamics of both a cytoskeletal filament and an intracellular cargo.

In the first problem, the results of which we have described in detail in Chapters 2 and 3, we explicitly model a semiflexible filament as it glides on a two dimensional substrate decorated with motor proteins. This model is very different from the effective active polymer models which either uses an active noise or models activity as a self-propulsive force acting tangentially on the filament. The filament is modeled as a semiflexible bead-spring polymer while the motor proteins are modeled as elastic springs which undergo attachment-detachment kinetics with the filament. The detachment increases with increasing local load. In the attached state, the motor proteins move along the filament in a given direction forcing the filament to move in the opposite direction. The velocity of motor proteins moving along the filament is dependent on the local extension. We look at the effect of local stress on the morphology of the polymer. In particular, the end-to-end distribution shows several interesting features like reduction of effective bending stiffness when detachment kinetics is local load independent, restoration of bending stiffness when detachment becomes load dependent and again lowering of effective bending stiffness as the local load dependent active velocity is increased. In the last case, the polymer coexists between open and spiral states which we characterize using an order parameter. Further, we see a very interesting behavior in the center of mass dynamics of the polymer as it shows multiple diffusive-ballistic crossovers. These unexpected results cannot be explained within an effective active polymer model as we identify three relaxation time scales : inertial, speed and orientational time scales of the center of mass velocity vector.

In the second problem, we turn our attention to the experimentally observed detachment kinetics of a specific molecular motor : dynein which shows a unique slip-catch-slip behavior, and look at its role in the intracellular transport of cargo.

As opposed to the previous study on gliding assay, the geometry is inverted to a bead assay and the detachment kinetics for dynein at a intermediate force range decreases with increasing force. The consequence on bidirectional cargo transport are far reaching. As opposed to the usual tug-of-war scenario where the motor set with the stronger pull wins, here we see a counter intuitive result. At certain load forces where the dyenin catch bond is activated, the motor binds stronger to the filament. As a result, increasing kinesin motors does not favor a plus directed movement of the cargo. The average processivity is negative and there is an extended parameter space where this phenomena works. This connects very well with recent experimental observations which have been together labeled as the 'paradox of codependence'. Our results hints at a plausible resolution of this paradox. We characterize motility states of the cargo and construct motility diagrams.

We hope that both these studies, which look closely at the role of the activity of motor proteins on local stress generation and transport properties, will provide a framework to interpret experimental data and have wider implications for the understanding of motor-driven processes in the cell.

Bibliography

[1] B. Alberts *et al.*, *Essential Cell Biology* (Garland Science, USA2014).

[2] D. A. Fletcher and R. D. Mullins, Nature **463**, 485 (2010).

[3] Unknown, Accessed: 2019-06-12, `https://study.com/academy/lesson/cytoskeletal-proteins-types-function.html`.

[4] C. P. Broedersz and F. C. Mackintosh, Rev. Mod. Phys. **86**, 995 (2014).

[5] T. Risler, Encyclopedia of Complexity and Systems Science 1 (2009).

[6] A. Mogilner and G. Oster, Biophysical journal **71**, 3030 (1996).

[7] D. A. Fletcher and J. A. Theriot, Physical Biology **1**, T1 (2004).

[8] S. Leibler and D. A. Huse, The Journal of cell biology **121**, 1357 (1993).

[9] M. Glotzer, Annual review of cell and developmental biology **17**, 351 (2001).

[10] J. R. Sellers, Biochimica et Biophysica Acta (BBA)-Molecular Cell Research **1496**, 3 (2000).

[11] J. Howard and J. Spudich, Proceedings of the National Academy of Sciences of the United States of America **93**, 4462 (1996).

[12] S. M. Block, Cell **93**, 5 (1998).

[13] E. Berliner *et al.*, Nature **373**, 718 (1995).

[14] R. D. Vale *et al.*, Nature **380**, 451 (1996).

[15] C. M. Farrell, A. T. Mackey, L. M. Klumpp, and S. P. Gilbert, Journal of Biological Chemistry **277**, 17079 (2002).

[16] M. J. Schnitzer and S. M. Block, Nature **388**, 386 (1997).

[17] R. Mallik *et al.*, Trends in cell biology **23**, 575 (2013).

[18] R. Lye, M. Porter, J. Scholey, and J. McIntosh, Cell **51**, 309 (1987).

[19] B. M. Paschal *et al.*, Nature **330**, 672 (1987).

[20] T. A. Schroer, E. R. Steuer, and M. P. Sheetz, Cell **56**, 937 (1989).

[21] B. J. Schnapp and T. S. Reese, Proceedings of the National Academy of Sciences **86**, 1548 (1989).

[22] N. Hirokawa, R. Sato-Yoshitake, T. Yoshida, and T. Kawashima, The Journal of cell biology **111**, 1027 (1990).

[23] S. Lin and C. A. Collins, Journal of Cell Science **101**, 125 (1992).

[24] I. Corthésy-Theulaz, A. Pauloin, and S. R. Pfeffer, The Journal of Cell Biology **118**, 1333 (1992).

[25] F. Aniento, N. Emans, G. Griffiths, and J. Gruenberg, The Journal of cell biology **123**, 1373 (1993).

[26] K. R. Fath, G. M. Trimbur, and D. R. Burgess, The Journal of Cell Biology **126**, 661 (1994).

[27] C. M. Waterman-Storer *et al.*, Proceedings of the National Academy of Sciences **94**, 12180 (1997).

[28] A. Blocker *et al.*, The Journal of cell biology **137**, 113 (1997).

[29] P. Bieling *et al.*, Nature **450**, 1100 (2007).

[30] S. J. Kron and J. A. Spudich, Proc. Natl. Acad. Sci. **83**, 6272 (1986).

[31] S. Kron, Y. Toyoshima, T. Uyeda, and J. Spudich, Methods in enzymology **196**, 399 (1991).

[32] A. Kishino and T. Yanagida, Nature **334**, 74 (1988).

[33] J. Howard, A. Hudspeth, and R. Vale, Nature **342**, 154 (1989).

[34] A. J. Hunt, F. Gittes, and J. Howard, Biophysical journal **67**, 766 (1994).

[35] L. Bourdieu *et al.*, Physical review letters **75**, 176 (1995).

[36] V. Schaller *et al.*, Nature **467**, 73 (2010).

[37] Y. Sumino *et al.*, Nature **483**, 448 (2012).

[38] A. T. Lam *et al.*, Soft Matter **12**, 988 (2016).

[39] M. P. Sheetz and J. A. Spudich, Nature **303**, 31 (1983).

[40] A. Dhar and D. Chaudhuri, Phys. Rev. Lett. **89**, 65502 (2002).

[41] A. Chaudhuri and D. Chaudhuri, Soft Matter **12**, 2157 (2016).

[42] M. J. Schnitzer, K. Visscher, and S. M. Block, Nat. Cell Biol. **2**, 718 (2000).

[43] R. D. Vale, Cell **112**, 467 (2003).

[44] D. Chowdhury, Phys. Rep. **529**, 1 (2013).

[45] W. O. Hancock and J. Howard, Proc. Natl. Acad. Sci. **96**, 13147 (1999).

[46] F. Huber *et al.*, Adv. Phys. **62**, 1 (2013).

[47] F. C. MacKintosh, J. Käs, and P. a. Janmey, Phys. Rev. Lett. **75**, 4425 (1995).

[48] H. Yamaoka, S. Matsushita, Y. Shimada, and T. Adachi, Biomech. Model. Mechanobiol. **11**, 291 (2012).

[49] F. Kreten, C. Hoffmann, D. Riveline, and K. Kruse, Physical Review E **98**, 012413 (2018).

[50] F. Nedelec, T. Surrey, A. C. Maggs, and S. Leibler, Nature **389**, 305 (1997).

[51] K. Sekimoto, N. Mori, K. Tawada, and Y. Y. Toyoshima, Phys. Rev. Lett. **75**, 172 (1995).

[52] T. Surrey, F. Nédélec, S. Leibler, and E. Karsenti, Science **292**, 1167 (2001).

[53] L. Bourdieu *et al.*, Phys. Rev. Lett. **75**, 176 (1995).

[54] J. Kierfeld, K. Frentzel, P. Kraikivski, and R. Lipowsky, Eur. Phys. J. Spec. Top. **157**, 123 (2008).

[55] K. Oiwa *et al.*, Proc. Natl. Acad. Sci. U. S. A. **87**, 7893 (1990).

[56] N. Gupta, A. Chaudhuri, and D. Chaudhuri, Physical Review E **99**, (2019).

[57] D. L. Coy, M. Wagenbach, and J. Howard, J. Biol. Chem. **274**, 3667 (1999).

[58] A. D. Mehta *et al.*, Nature **400**, 590 (1999).

[59] M. Rief *et al.*, Proc. Natl. Acad. Sci. **97**, 9482 (2000).

[60] R. S. Rock *et al.*, Proc. Natl. Acad. Sci. U. S. A. **98**, 13655 (2001).

[61] A. Yildiz *et al.*, Science **300**, 2061 (2003).

[62] S. P. Gross *et al.*, J. Cell Biol. **156**, 855 (2002).

[63] C. Kural *et al.*, Science **308**, 1469 (2005).

[64] F. Jülicher and J. Prost, Phys. Rev. Lett. **75**, 2618 (1995).

[65] A. Vilfan, E. Frey, and F. Schwabl, Eur. Phys. J. B **3**, 535 (1998).

[66] M. Badoual, F. Jülicher, and J. Prost, Proc. Natl. Acad. Sci. U. S. A. **99**, 6696 (2002).

[67] S. Grill, K. Kruse, and F. Jülicher, Phys. Rev. Lett. **94**, 108104 (2005).

[68] S. Klumpp and R. Lipowsky, Proc. Natl. Acad. Sci. **102**, 17284 (2005).

[69] C. Leduc, N. Pavin, F. Jülicher, and S. Diez, Phys. Rev. Lett. **105**, 128103 (2010).

[70] A. Nair *et al.*, Phys. Rev. E **94**, 032403 (2016).

[71] H. Y. Lee and M. Kardar, Phys. Rev. E. Stat. Nonlin. Soft Matter Phys. **64**, 056113 (2001).

[72] S. Sankararaman, G. I. Menon, and P. B. Sunil Kumar, Phys. Rev. E **70**, 031905 (2004).

[73] H. Jiang and Z. Hou, Soft Matter **10**, 9248 (2014).

[74] H. Jiang and Z. Hou, Soft Matter **10**, 1012 (2014).

[75] R. E. Isele-Holder, J. Elgeti, and G. Gompper, Soft Matter **11**, 7181 (2015).

[76] G. Jayaraman *et al.*, Phys. Rev. Lett. **109**, 158302 (2012).

[77] A. Laskar *et al.*, Sci. Rep. **3**, 1964 (2013).

[78] R. Chelakkot, A. Gopinath, L. Mahadevan, and M. F. Hagan, Journal of The Royal Society Interface **11**, (2014).

[79] D. Sarkar and S. Thakur, The Journal of Chemical Physics **146**, 154901 (2017).

[80] N. Kikuchi *et al.*, Proc. Natl. Acad. Sci. U. S. A. **106**, 19776 (2009).

[81] J. Gladrow *et al.*, Phys. Rev. Lett. **116**, 248301 (2016).

[82] K. R. Prathyusha, S. Henkes, and R. Sknepnek, Phys. Rev. E **97**, 022606 (2018).

[83] O. Duman, R. E. Isele-Holder, J. Elgeti, and G. Gompper, Soft Matter **14**, 4483 (2018).

[84] T. Eisenstecken, G. Gompper, and R. Winkler, Polymers (Basel). **8**, 304 (2016).

[85] Y. Yang, V. Marceau, and G. Gompper, Phys. Rev. E **82**, 031904 (2010).

[86] A. Ghosh and N. S. Gov, Biophys. J. **107**, 1065 (2014).

[87] A. Chaudhuri and D. Chaudhuri, Soft Matter **12**, 2157 (2016).

[88] D. Chaudhuri, Phys. Rev. E **75**, 21803 (2007).

[89] R. Chelakkot, A. Gopinath, L. Mahadevan, and M. F. Hagan, J. R. Soc. Interface **11**, 20130884 (2014).

[90] S. G. Krantz, *Handbook of Complex Variables* (Birkhäuser, Boston,MA1999).

[91] F. Peruani and L. G. Morelli, Phys. Rev. Lett. **99**, 010602 (2007).

[92] D. Selmeczi *et al.*, Biophys. J. **89**, 912 (2005).

[93] C. Gardiner, *Stochastic Methods: A Handbook for the Natural and Social Sciences*, *Springer Series in Synergetics* (Springer Berlin Heidelberg, 2009).

[94] M. A. Welte, Current Biology **14**, R525 (2004).

[95] M. J. I. Müller, S. Klumpp, and R. Lipowsky, Proc. Natl. Acad. Sci. U. S. A. **105**, 4609 (2008).

[96] V. Soppina *et al.*, Proceedings of the National Academy of Sciences **106**, 19381 (2009).

[97] D. Bhat and M. Gopalakrishnan, Physical Biology **9**, 046003 (2012).

[98] W. O. Hancock, Nature reviews Molecular cell biology **15**, 615 (2014).

[99] S. P. Gross *et al.*, The Journal of cell biology **156**, 855 (2002).

[100] M. A. Welte *et al.*, Cell **92**, 547 (1998).

[101] P. J. Hollenbeck, Front Biosci **1**, d91 (1996).

[102] M. Schuster *et al.*, Proceedings of the National Academy of Sciences **108**, 3618 (2011).

[103] M. J. Müller, S. Klumpp, and R. Lipowsky, Proceedings of the National Academy of Sciences **105**, 4609 (2008).

[104] M. J. Müller, S. Klumpp, and R. Lipowsky, Journal of Statistical Physics **133**, 1059 (2008).

[105] M. J. Müller, S. Klumpp, and R. Lipowsky, Biophysical journal **98**, 2610 (2010).

[106] A. G. Hendricks *et al.*, Current Biology **20**, 697 (2010).

[107] A. Gennerich and D. Schild, Physical biology **3**, 45 (2006).

[108] M. Martin *et al.*, Molecular biology of the cell **10**, 3717 (1999).

[109] S. Ally *et al.*, The Journal of cell biology **187**, 1071 (2009).

[110] S. P. Gross, M. A. Welte, S. M. Block, and E. F. Wieschaus, The Journal of cell biology **156**, 715 (2002).

[111] S. E. Encalada, L. Szpankowski, C.-h. Xia, and L. S. Goldstein, Cell **144**, 551 (2011).

[112] A. K. Rai *et al.*, Cell **152**, 172 (2013).

[113] A. Kunwar *et al.*, Proceedings of the National Academy of Sciences **108**, 18960 (2011).

[114] O. V. Prezhdo and Y. V. Pereverzev, Accounts of Chemical Research **42**, 693 (2009).

[115] R. P. McEver and C. Zhu, Annual Review of Cell and Developmental Biology **26**, 363 (2010).

[116] S. Rakshit and S. Sivasankar, Physical Chemistry Chemical Physics **16**, 2211 (2014).

[117] B. T. Marshall *et al.*, Nature **423**, 190 (2003).

[118] Rutherford Aris Vectors, Tensors and the Basic Equations of Fluid Mechanics Dover Books on Engineering 1990.pdf.

[119] B. Guo and W. H. Guilford, Proc. Natl. Acad. Sci. U. S. A. **103**, 9844 (2006).

[120] A. Yamada *et al.*, Nature Communications **5**, (2014).

[121] B. Akiyoshi *et al.*, Nature **468**, 576 (2010).

[122] P. Puri *et al.*, Dynein catch bond as a mediator of codependent bidirectional cellular transport, 2018.

[123] E. Evans, A. Leung, V. Heinrich, and C. Zhu, Proceedings of the National Academy of Sciences **101**, 11281 (2004).

[124] V. Barsegov and D. Thirumalai, Physical Review Letters **95**, (2005).

[125] D. Bartolo, I. Derényi, and A. Ajdari, Physical Review E **65**, (2002).

[126] Y. V. Pereverzev and O. V. Prezhdo, Biophysical Journal **91**, L19 (2006).

[127] E. A. Novikova and C. Storm, Biophysical Journal **105**, 1336 (2013).

[128] R. Mallik *et al.*, Nature **427**, 649 (2004).

[129] M. P. Singh, R. Mallik, S. P. Gross, and C. Y. Clare, Proceedings of the National Academy of Sciences of the United States of America **102**, 12059 (2005).

[130] A. Nair *et al.*, Physical Review E **94**, 032403 (2016).

[131] C. Leidel, R. A. Longoria, F. M. Gutierrez, and G. T. Shubeita, Biophysical journal **103**, 492 (2012).

[132] S. Chakrabarti, M. Hinczewski, and D. Thirumalai, Journal of Structural Biology **197**, 50 (2017).

[133] R. Mallik *et al.*, Current Biology **15**, 2075 (2005).

[134] S. Toba *et al.*, Proceedings of the National Academy of Sciences **103**, 5741 (2006).

[135] J. Beeg *et al.*, Biophysical journal **94**, 532 (2008).

[136] C. Leduc *et al.*, Proceedings of the National Academy of Sciences of the United States of America **101**, 17096 (2004).

[137] S. L. Reck-Peterson *et al.*, Cell **126**, 335 (2006).

[138] N. J. Carter and R. Cross, Nature **435**, 308 (2005).

[139] S. J. King and T. A. Schroer, Nature cell biology **2**, 20 (2000).

[140] H. Kojima, M. Kikumoto, H. Sakakibara, and K. Oiwa, Journal of biological physics **28**, 335 (2002).

[141] A. Gennerich, A. P. Carter, S. L. Reck-Peterson, and R. D. Vale, Cell **131**, 952 (2007).

[142] D. T. Gillespie, Journal of computational physics **22**, 403 (1976).

[143] D. T. Gillespie, The journal of physical chemistry **81**, 2340 (1977).

[144] W. M. Saxton, J. Hicks, L. S. Goldstein, and E. C. Raff, Cell **64**, 1093 (1991).

[145] D. D. Hurd and W. M. Saxton, Genetics **144**, 1075 (1996).

[146] J. G. Gindhart *et al.*, The Journal of cell biology **141**, 443 (1998).

[147] S. P. Gross, Current biology **13**, R320 (2003).

[148] S. P. Gross, Physical biology **1**, R1 (2004).

[149] S. P. Gross, Y. Guo, J. E. Martinez, and M. A. Welte, Current biology **13**, 1660 (2003).

[150] S. P. Gross, M. A. Welte, S. M. Block, and E. F. Wieschaus, The Journal of cell biology **148**, 945 (2000).

[151] G. T. Shubeita *et al.*, Cell **135**, 1098 (2008).

[152] M. A. Welte *et al.*, Current Biology **15**, 1266 (2005).

[153] R. J. McKenney *et al.*, Cell **141**, 304 (2010).

[154] M. Hu and E. Holzbaur, J. Cell Biol. **202**, 495 (2013).

[155] F. Berger, C. Keller, S. Klumpp, and R. Lipowsky, Physical Review Letters **108**, (2012).

[156] M. C. Uçar and R. Lipowsky, Soft Matter **13**, 328 (2017).

[157] S. Uemura *et al.*, Proc. Natl. Acad. Sci. U. S. A. **99**, 5977 (2002).

[158] J. R. Cooper and L. Wordeman, Current Opinion in Cell Biology **21**, 68 (2009).

[159] D. L. Coy, J. Biol. Chem. **274**, 3667 (1999).